Alma Mater Studiorum – Università di Bologna

DOTTORATO DI RICERCA IN

Biologia Cellulare e Molecolare

Ciclo XXVIII

Settore Concorsuale di afferenza: **05/E2 Biologia molecolare**

Settore Scientifico disciplinare: **BIO/11 Biologia Molecolare**

STRUCTURAL INVESTIGATION OF ANTIGENS USING ELECTRON MICROSCOPY

Presentata da: **Ilaria Peschiera**

Coordinatore Dottorato:
Chir.mo Prof. **Giovanni Capranico**

Relatore:
Dott.ssa **Ilaria Ferlenghi**

Co-Relatore:
Chir.mo Prof. **Vincenzo Scarlato**

Co-relatore:
Dr. **Lassi Juho Liljeroos**

Esame finale anno 2016

To my family and Anto,

Because they are the base of my strength

“The important thing is not to stop questioning. Curiosity has its own reason for existing. One cannot help but be in awe when he contemplates the mysteries of eternity, of life, of the marvelous structure of reality. It is enough if one tries merely to comprehend a little of this mystery each day. Never lose a holy curiosity”

“La cosa importante è non smettere di fare domande. La curiosità ha il suo motivo di esistere. Non si può far altro che restare stupiti quando si contemplano i misteri dell’eternità, della vita, della struttura meravigliosa della realtà. E’ abbastanza se si cercano di comprendere un poco di questo mistero ogni giorno. Non perdere mai una sacra curiosità.

Albert Einstein

Preface

Since my PhD is going to the end, I believe that part of my thesis should record the scientific gratitude for the people that I met during these three years and helped me in developing my scientific career.

Firstly I would like to thank Professor Vincenzo Scarlato (Università di Bologna) for the supervision of my PhD work.
Then I would like to thank the Electron Microscopy facility of Siena (Dipartimento Di Scienze della Vita) that introduced me in the "dark" world of Electron Microscopy. Professor Pietro Lupetti and Eugenio Paccagnini were always there for advices and suggestions. Particularly, my gratitude is for Dr. Fabiola Giusti. She patiently guided me to the secrets of Electron Microscopy imaging spending many hours and much energy with me in front of a microscope.
I would like to thank Dr. Kasim Sader (FEI Company) and the FEI Group for the great possibility they offered me in collecting Cryo-EM data. During the week I spent with them I realized the great potentiality of the Electron Microscopy applied to Biology. Particularly my gratitude is for Dr.Sader that shared with me his knowledge in the technology improvement and data collection. Without his outstanding experience the data collection would never be possible.
Last but not list I would like to thank Prof. José Maria Carazo and his group (Biocomputing Unit, CNB, Madrid). It has been an honor and a huge opportunity to spend one month of my PhD with them. Thanks to their invaluable scientific experience, their availability and kindness, I had a great time both personally and scientifically. It was really fruitfully for my understanding of such a difficult topic like EM data processing workflow. Most importantly I am grateful for the sport and coffee sessions we shared that gave me the opportunity to enjoy their company (sometimes understanding only the concept of the Spanish conversations!). Particularly, I would like to thank Prof. Carazo for the scientific (and dancing) suggestions; a thank goes to Dr. José Miguel de la Rosa-Trevin for the introduction to the Scipion software and for the patience to answer to my "bothering" questions. A special thank is for Dr. Roberto Melero that guided me in the image processing workflow with kindness and patience, always available for explanations, discussions and advices.

All these experiences made me more conscious and passionate of my work contributing to my personal and scientific growth.

Table of Contents

Abstract

The research activity of my PhD focused on two different projects: the main project was directed to understand the biological phenomena of monoclonal antibodies (mAbs) cooperative bactericidal activity whereas the second one aimed to understand the structure of the *N.meningitidis* antigen NadA var.3.

Cooperative bactericidal activity of anti fHbp mAbs: The mAbs cooperativity is a mechanism that occurs when mAbs that individually show low or no bactericidal activity become bactericidal when coupled together.

Revealing the structural bases of cooperative bactericidal activity by mAbs is fundamental for a thorough understanding of antibody-based mechanisms of protection against bacterial diseases. As far as it is known from literature, this phenomenon has been investigated only on meningococcal factor H binding protein (fHbp), a 27.5 kDa meningococcal surface-exposed lipoprotein and one of the four antigens present in the recently released Bexsero® vaccine for prevention of serogroup B *Neisseria meningitidis* infections.

Recently, several published works predict a mechanism of protection induced by mAbs where an optimal relative orientation of the mAbs bound to the antigen is hypothesized as a necessary step for the recruitment of C1q and the consequent activation of the classical complement pathway. To investigate the structural bases of the cooperative bactericidal activity, a biochemical, biophysical and Transmission Electron Microscopy (TEM) characterization of the cooperative and non-cooperative couples of both murine mAbs and human IgG mAbs has been performed in this work. The comparison of the structure of the murine cooperative complex with the human cooperative one strongly underlines the higher level of flexibility and instability of the first complex. Although previously published data showed that human mAbs do not map in the factor H (fH) binding site we have been able to prove that a simultaneous binding of fH to the immune cooperative complex occurs in the complement activation. Moreover in the investigation of the geometrical relationship between the antigen and the human monoclonal antibodies in the complex, performed through the 3D reconstruction of the complexes, we showed that the angle formed between the fHbp and the antibodies is identical indicating that the reciprocal orientation of the human monoclonal antibodies is only dependent on its epitope location on the antigen.

Finally, the high variability of assembly for non-cooperative human monoclonal complexes prove the structural dissimilarities with the cooperative human complexes thus identifying the main cause of the absence of the complex formation in the partial epitopes overlapping, as proved by Hydrogen/Deuterium Exchange Mass Spectrometry (HDX_MS).

Structural characterization of NadA: Determine the structure of the Neisserial adhesin A (NadA) antigen is a key step for a complete knowledge of its role in the bacterial pathogenesis of *Neisseria meningitidis*. NadA is a member of the Oligomeric Coiled-coil Adhesin (OCA) family of bacterial Trimeric Autotransporter Adhesins (TAA) mediating adhesion to and entry into epithelial cells. In the present work, the NadA var. 3 structure, the variant included in Bexsero® vaccine, was determined by the Cryo-Electron Microscopy (Cryo-EM) technique combined with Single Particle (SP) reconstruction method.

Preliminary morphological analysis of the sample by negative stain TEM revealed that NadA var.3 is a thin and elongated rod like structure decorated by a globular head. NadA var.3 homotrimer presents two recurrent points of bent along the stalk: the first one at the 1/3 of the stalk length and the second one closer to the C-terminus

The 3D reconstruction of NadA var.3, generated from Cryo-TEM data, shows an elongated and thin stalk decorated by a globular compact head characterized by a three-fold symmetry. Interestingly the 3D EM map shows three evident points of interruption of the density in the stalk region presumably correlated with the three interruptions present in the coiled-coil periodicity of NadA var.3 the sequence. This result indicates a possible role of the interruptions in the flexibility/extension mechanism of the antigen as a possible alternative mechanism to the already known multiple-module mechanism.

Neisseria meningitidis & Electron microscopy: structural vaccinology

Chapter 1

1.1 *Neisseria meningitidis*

1.1.1 The pathogen and the vaccine

Neisseria meningitidis is a gram negative diplococcus and an obligate human pathogen, well known as an important cause of morbidity and mortality worldwide. Meningitis and sepsis are life-threatening conditions that affect people depending on the epidemiological areas with an incidence ranging between 0.5 and 1000/100000 cases (Lewis & Ram, 2014; Pizza & Rappuoli, 2015). Outbreaks of the Invasive Meningococcal Disease (IMD) occur mainly in the African meningitis belt, in Europe, New Zeland, Canada and in the US Pacific Northwest (Stephens et al., 2007). Meningococcus colonizes the nasopharyngeal mucosa and is most typically carried asymptomatically by approximately 10% of the population. The rates of asymptomatic carriage increase in certain conditions (such as household crowding, active and passive smoking) and at different ages, with a peak in the adolescent. Although colonization of the nasopharynx is a common event, the disease is rare, but can cause death in 10-15% of the cases or permanent disability up to 19% of the cases (Caugant & Maiden, 2009; Leca et al., 2015; Stephens et al., 2007). A crucial step in the establishment of the carrier state is the adhesion to mucosal surface. It may lead a local inflammation and through the invasion of mucosal surfaces can access to the blood-stream leading to septicemia and/or meningitis (Pizza & Rappuoli, 2015) (Figure 1.1).

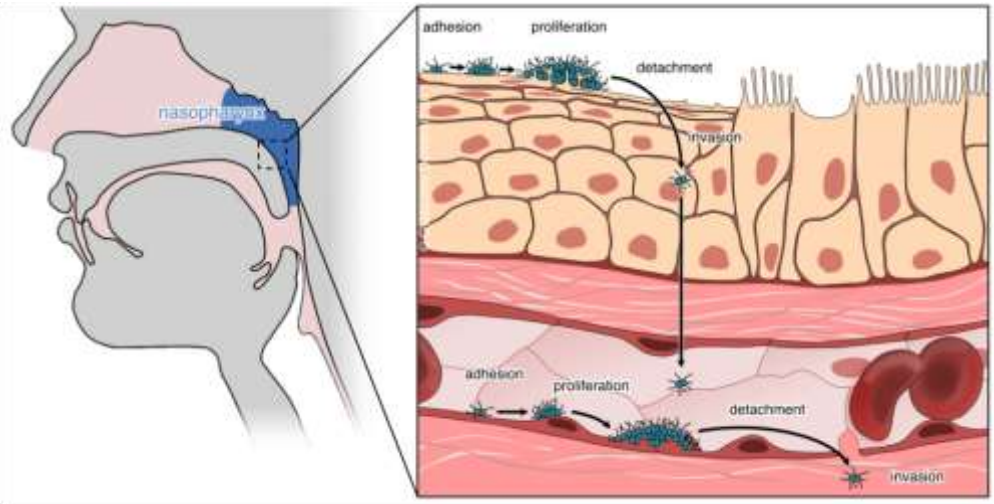

Figure 1.1: Scheme of the meningococcal invasion from the nasopharynx to the blood-stream. Taken from the website https://research.pasteur.fr/en/team/pathogenesis-of-vascular-infections/ .

Most of the *N.meningitidis* strains causing invasive disease are encapsulated. The capsule, mainly composed by polysaccharides is essential for the survival of the bacteria in the blood allowing to resist to antibody/complement mediated killing and to inhibit

phagocytosis. Twelve different meningococcal serogroups have been defined based on capsular polysaccharides composition of which five, A, B, C, W135 and Y, are responsible of more than 95% of the disease (Rouphael & Stephens, 2012).

Despite the wealth of knowledge already available on the pathogenesis and the genetics of meningococcal strains, the emergence of strains with epidemic potential and the change in serogroup circulation are unpredictable (Khatami & Pollard, 2010). In light of these observations, it's a global significance the development of a vaccines conferring broad protection against *N.meningitidis*. Up to date, vaccines against the serogroup A, C, Y and W135 have been produced as conjugated polysaccharide vaccine containing the purified Capsular Polysaccharide (CPS) and a carrier protein such as CRM197, a non-toxic mutant of the diphtheria toxin (Costantino et al., 2011). The tetravalent (groups A, C, W, Y) conjugate (Menactra, Menveo and Nimenrix) and the monovalent against group C (e.g., MenC, Menjugate) are examples of the available vaccines (Lewis & Ram, 2014).

For decades, no broadly protective vaccine against meningococcal group B (MenB) was available. The main reason of this difficulty relies in the composition of the MenB CPS that consisted of a homopolymer of α (2-8)-linked polysialic acid. These structures are antigenically comparable to the human fetal neural cell adhesion molecules and thus poorly immunogenic leading to the concern that MenB polysaccharide or glyconjugate based-vaccine may induce auto-antibodies (Finne et al., 1983). Consequently, all the efforts of the search for an ideal vaccine candidate have been focused on non-capsular antigens. Recently, two vaccines have been released in 2014: the vaccine Bexsero® and Trumenba®.

Bexsero® formulation contains three recombinant main antigens and Outer Membrane Vesicles (OMVs) and its composition has been developed based on a strategy called Reverse Vaccinology (RV) (Giuliani et al., 2006; Rappuoli, 2001; Tettelin et al., 2000).

1.1.2 The antigens present in Bexsero®

The proteins found through the RV were Neisserial Heparin Binding Antigen (NHBA), factor H binding protein (fHbp) and Neisserial adhesin A (NadA) (Figure 1.2). Two additional antigens GNA 2091 and GNA 1030, that in some of the assays induced protective immunity, were selected. Thus, the final multicomponent formulation of Bexsero® contains the NHBA, the fHbp, NadA with ¼ OMV to induce better and broader protection (Serruto et al., 2012).

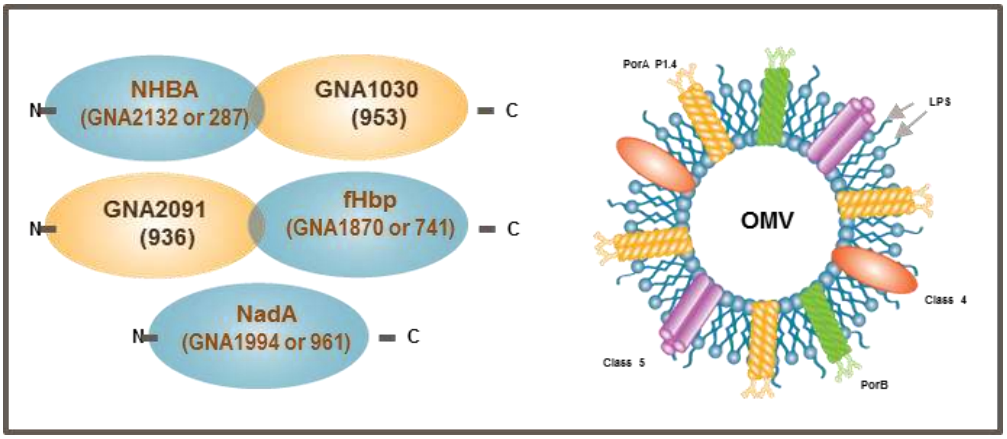

Figure 1.2: Schematic representation of the 4CMenB vaccine formulation. The image shows the main antigens identified through Reverse Vaccinology approach (NHBA, fHbp and NadA) on the left and the OMV on the right. Courtesy of Dr. Rappuoli R.

NHBA is a surface-exposed lipoprotein that binds heparin *in vitro* through an arginine-rich region resulting in increased survival in human serum and suggesting a role for NHBA in protection against complement (Serruto et al., 2010). Moreover, Serruto and collaborators suggested that *in vivo*, NHBA is able to bind glysoaminoglycans that are present in mucosal secretions (Serruto et al., 2010). The primary amino acid sequence of NHBA covers approximately 450 residues: the N-terminal region (spanning from residues 1 to ~ 230) annotated as intrinsically unfolded, the central arginine-rich motif (residues 235-245 in strain 2996) involved in the heparin binding, and a C-terminal region (spanning residues 246-428) (Serruto et al., 2010). The structure available up to date is only the C terminal region, recently determined by NMR that reveal 8 stranded anti parallel β-barrel (PDB entry: 2LFU) (Esposito et al., 2011) (Figure 1.3).

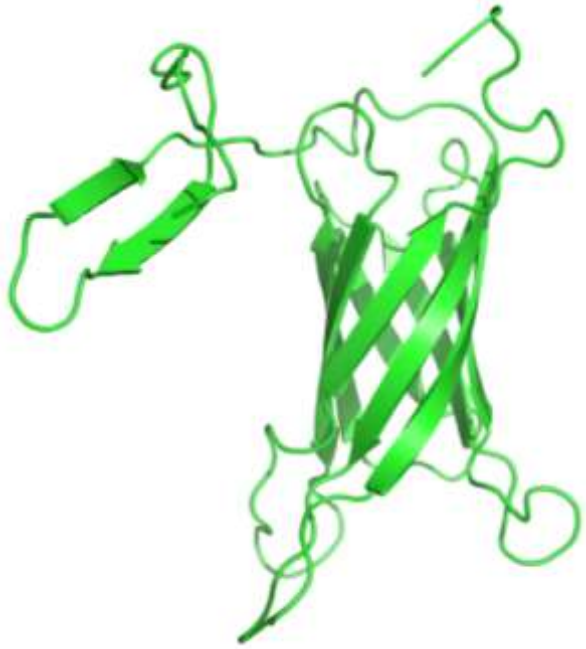

Figure 1.3: The structure of the conserved C-terminal region of NHBA resolved using NMR technique (PDB entry: 2LFU).The image is taken from Esposito et al., 2011.

Interestingly, the NHBA clearly shows a similar fold to the fHbp including the C-terminal portion, one turn N-terminal helix and a semi-conserved cluster of glycine (Esposito et al., 2011). These evidences combined with a very low sequence identity suggest that the proteins may be evolved from a common ancestor but are unlikely to share the same function. The gene of NHBA is present in all the *N.meningitidis* tested and a sequence analysis from genetically diverse group B strains reveals the presence of variable segments of NHBA, although the highly conserved N-terminal and C-terminal regions (Lewis et al., 2010; Pizza et al., 2000).

NadA was identified as a member of the Oligomeric Coiled-coil Adhesin family of bacterial auto-transporter adhesins, which shares a common secretory mechanism of the extracellular N-terminal domain, named passenger domain, and its subsequent trimerization on the bacterial surface. NadA is involved in bacterial adhesion to and entry into epithelial cells (Capecchi et al., 2005; Comanducci et al., 2002; Cotter et al., 2006; Surana et al., 2004). The *nadA* gene is found in ~30% of meningococcal pathogenic strains belonging to three out of the four known hypervirulent lineages of serogroup B and C, whereas it is mostly absent from carrier strains and not found in other commensal species like *N.lactamica* and *N.cinerea* (Comanducci et al., 2002). *In vivo*, the NadA is expressed at different levels during growth and it is up regulated by niche signal varying

the levels by more than 100-fold among isolates (Comanducci et al., 2002; Fagnocchi et al., 2013). Recently, the NadA family was genetically divided in six variants clustered in two main groups sharing an amino acid sequence identities of 45-50%. The Group I includes the vaccine antigen, the NadA var.3 (Bambini et al., 2014; Bambini et al., 2009). Structurally, NadA belongs to the Trimeric Auto-transporter Adhesins family, a class of OCA, (Capecchi et al., 2005; Magagnoli et al., 2009). The TAAs are commonly composed by a terminal domain (head) that is mainly responsible for binding to host cellular receptors, a passenger domain responsible for adhesion and made of a central α-helical domain (stalk) forming coiled-coil structure and a membrane domain with the anchor function (Malito et al., 2014). Recently Malito *et al.* were able to obtain a 2 Å crystal structure of the NadA var.5 (PDB entry: 4CJD), which belongs to a different group from the vaccine variant (Malito et al., 2014). The overall structure (residue 24-220) is made of an elongated homotrimeric coiled-coil stalk that extends from N terminus to the C terminus with a length of roughly 220 Å and with an average width of 15 Å in its central stalk region. The N-terminal region was detected with a broader width of ~ 40 Å that forms the head domain. Unfortunately, from the residue 137 to the residue 199 the electron densities were discontinuous suggesting that the three helices are less stable in this region. These conclusions are also supported by the observation that the last visible fragment spanning from residue 199 to residue 210 is arranged as short uncoiled helices, with a relatively large diameter of ~ 47 Å (Malito et al., 2014). Interestingly, preliminary Transmission Electron Microscopy (TEM) analysis demonstrated that the vaccine NadA var.3 shares a structural similarity with the NadA var.5 presumably reflecting the conserved function among NadA variants (Comanducci et al., 2004; Malito et al., 2014). Nevertheless, the lack of immunological cross-reactivity between the two groups of variants to which belongs the NadA var.5 and NadA var.3 suggest structural and/or surface-localized differences (Malito et al., 2014). Figure 1.4 shows the models of NadA var.3 and NadA var.5.

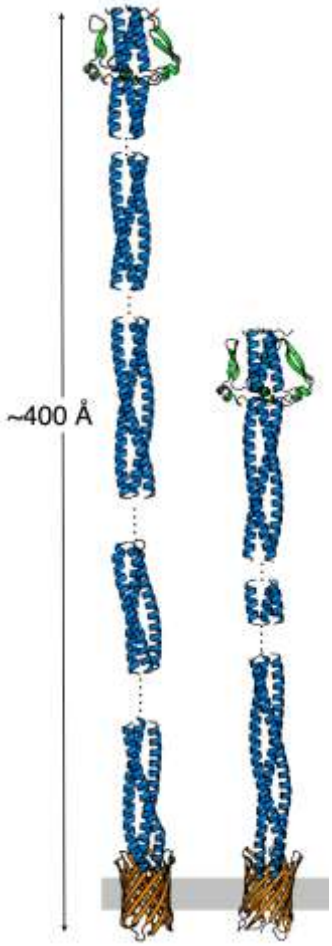

Figure 1.4: Full-length models of NadA var.3 and NadA var.5. The models are shown as cartoons: the stalk (blue colored), the wings-like insertions of the head domain (shown in green), and the transmembrane anchor (orange color). The outer membrane of the bacterium is gray colored. The dashed lines indicate either regions missing in the crystal structure of NadA var.5 or regions with low sequence homology or unknown secondary structure that were not included in the models. The image is a modification from Malito et al., 2014.

fHbp was firstly identified as a surface-exposed lipoprotein during the screening of the MC58 genome, but it was also discovered independently using the approach of membrane fractionation (Fletcher et al., 2004; Masignani et al., 2003; Pizza et al., 2000). The fHbp is expressed at different levels among strains and it is regulated by oxygen availability in a FNR-dependent manner (Masignani et al., 2003; Oriente et al., 2010). Although the expression of fHbp is present in nearly all *N.meningitidis* isolates examined thus far, a few strains that do not express fHbp have been identified (Bambini et al., 2009; Lucidarme et al., 2011; Masignani et al., 2003). fHbp can be classified into three genetic and immunogenic variants, fHbp var.1, fHbp var.2, fHbp var.3, that can be further divided into subvariants fHbp var.1.x, fHbp var.2.x and fHbp var.3.x The sequence conservation

within each variant ranges from 92%-100% whereas among variants can be as low as 63%. This diversity has a negative influence on the cross-protection: a member of each variant can induce a protective immune response against homologous strains, but is not able to induce complement mediated bactericidal antibodies against strains that express distantly related variants (Masignani et al., 2003). The three-dimensional (3D) structure of fHbp has been determined by Nuclear Magnetic Resonance (NMR) (PDB entry: 2KCO) spectroscopy and by X-ray crystallography (PDB entry: 3KVD) (Cantini et al., 2009; Cendron et al., 2011). The two structures are very similar and consist of two β-barrel with different topologies: an N-terminal domain (spanning the fragment 79-202 in the crystal structure) of 8 β-strands forming a highly curved anti-parallel β-sheet and a C-terminal domain (extended from residue 202 to 320 in the crystal structure) that is a well-defined β-barrel of 8 anti-parallel β-strands. The two domains are connected by a short linker, which together with several predominantly hydrophobic inter-domain contacts result in minimal freedom of movement between the two domains (Figure 1.5). Although the over 300 different sequence variants of fHbp known, multiple sequence alignments demonstrated that the residues contributing to the hydrophobic cores between the domains covering a surface of ~ 3500 Å are well conserved, suggesting that the 3D fold will be the same in all the variants (Cendron et al., 2011; Serruto et al., 2012).

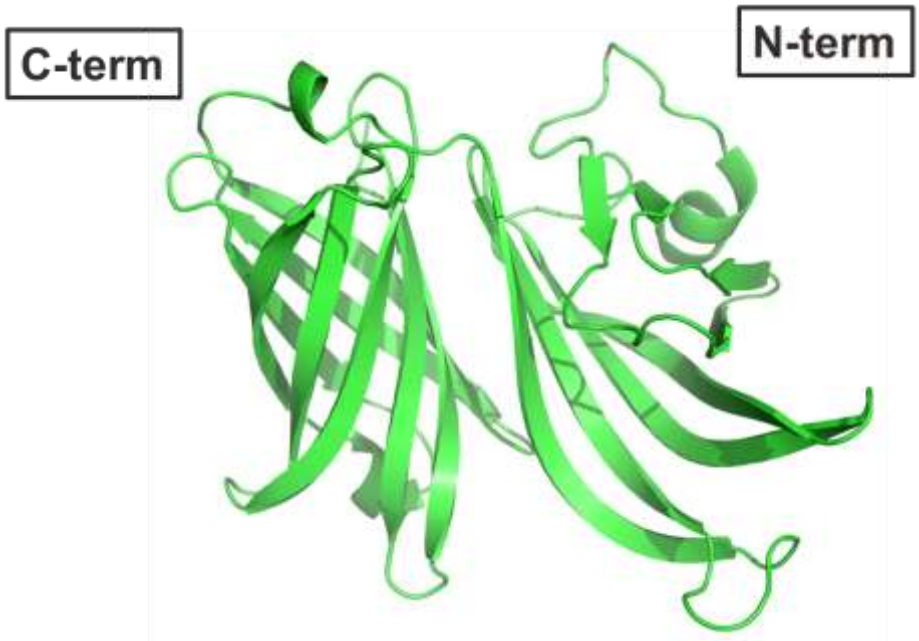

Figure 1.5: X-Ray cartoon structure of the fHbp var.1 solved at 2 Å (PDB entry: 3KVD) showing the two distinct domains connected by a loop. Image is taken from Cendron et al., 2011.

fHbp is produced as a precursor that undergoes N-terminal processing and lipidation at the cysteine present in the lipo-box motif (LxxC) allowing to anchor the antigen on the

outer membrane of the bacteria. The 10 residues between the lapidated Cys and the folded N-terminal domain of fHbp formed a highly flexible region that has been removed from the protein in most of the structural studies. However, it was proved that no significant differences were found between the recombinant structures and the structures of the lapidated fHbp form micelle-associated (Cendron et al., 2011; Mascioni et al., 2010; Serruto et al., 2012). fHbp binds human factor H (fH), an inhibitor of the alternative complement pathway and the binding was demonstrated to be specific for human fH (Granoff et al., 2009). This interaction is a bacterial mechanism to escape from the human immune system hampering the recognition of surface-exposed fHbp epitopes that are targets for bactericidal antibodies. This hypothesis was tested by Beernink and colleagues that expressed human fH in BALB/c mouse and then immunized the transgenic human fH mice with wild-type fHbp var.1 resulting in a lower IgG response and significantly lower Serum Bactericidal Activity (SBA) titers than wild-type mice (because murine fH does not bind fHbp) (Beernink et al., 2011). Moreover it has been shown that another surface protein A, called NspA, expressed by all meningococcal strains, is able to bind fH (Lewis et al., 2010). This is a redundant mechanism of the meningococcus in recruiting the factor H that underlines the key role of this strategy to limit complement activation on the bacterial surface (Serruto et al., 2012).

The mechanisms of the bacteria to escape from the complement activation are one of the main critical points necessarily to be addressed for extending the coverage of the vaccine.

1.1.3 The classical complement pathway and the cooperative bactericidal activity

The knowledge on the complement pathway and the role of antibodies in this mechanism is one of the fundamental steps to improve the potency and efficacy of vaccines against bacterial diseases.

The complement system has traditionally been considered as a first-line of innate immune defense against invading pathogens. Nevertheless, during the last decades, researchers discovered additional roles for the complement system in modulation of adaptive immune response, elimination of immune complexes and apoptotic cells, metabolism, angiogenesis, tissue regeneration, and organogenesis (Rosenstein et al., 2001). The complement system is characterized by serine-proteases that specifically cleave the next factor resulting in a proteolytic cascade to opsonize and lyse the bacteria (Nonaka, 2014). It comprises about 30 soluble molecules and several membrane inhibitors or receptors for complement components (Lewis & Ram, 2014). All of them are involved differently in the

three steps of the complement activation: the initiation, the cascade amplification and the effector production. The initiation starts from the recognition of a wide variety of molecular substrates and is considered to continue until the activation of the first serine proteases. Then during the step of amplification, the proteolytic cascade results in generation of peptides called anaphylatoxins that are the effectors of the final inflammation, phagocytosis and stimulation of B-cells and t-cells (Forneris et al., 2012; Nonaka, 2014). This pathway is finely controlled through the use of several regulators that prevent complement activation in order to balance the attack from foreign surfaces and the protection of host (Kirkitadze & Barlow, 2001; Zipfel, 2009). Complement activation on the bacterial surface can be initiated by one of the three pathways: the alternative, the classical and the lectin pathway. All of these pathways converge in the central cleavage of the complement component C3 (Figure 1.6).

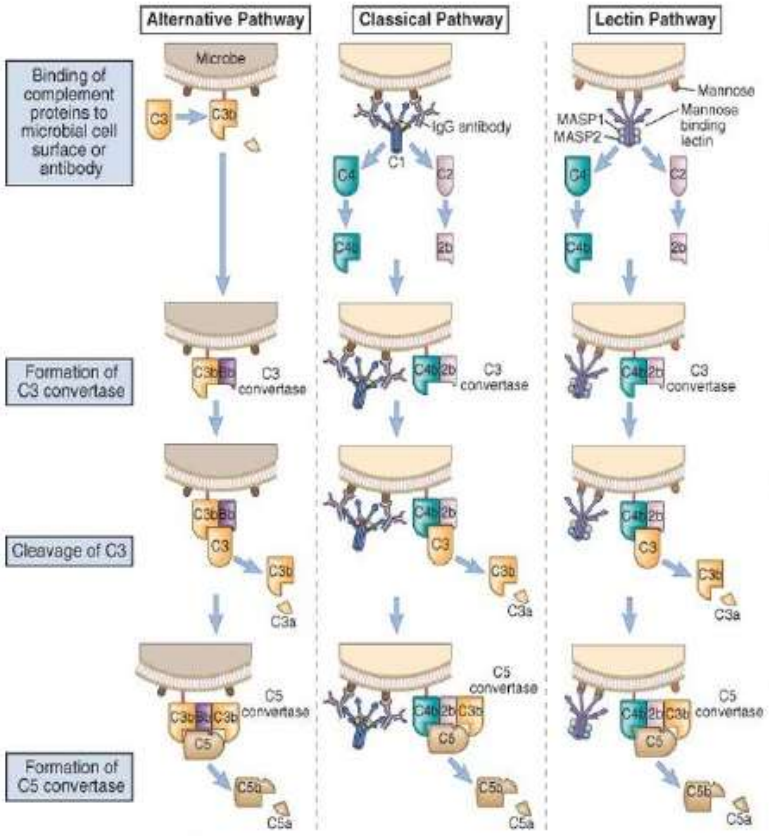

Figure 1.6: Representation of the three pathways that activate the complement system: alternative, classical and lectin pathway. The main steps of the three mechanisms are reported on the left. The image is from Abbas et al., Elsevier: Cellular and molecular immunology. http://www.slideshare.net/AllergyChula/complement-and-complement-deficiency.

The pathway activated by antibodies is the Classical Pathway (CP). It is initiated by binding of an antibody to its target resulting in a conformational change in the hinge region

of the Fc domain of the antibody that enables the engagement of the C1 complex. C1 is a multi-molecular complex formed by the subunit C1q associated with two copies of two serine-proteases, C1r, and C1s that is supposed to undergo to a conformational rearrangements in order to activate the C4 and thus the entire complement cascade (Cooper, 1985; Gaboriaud et al., 2004). A difference in the complement activation resides across IgG subclasses due to the variances in the amino acid sequence and glycosylation pattern in the C_H2 and C_H3 regions of the heavy chains of antibody (e.g. human classification: IgG3 > IgG1 > IgG2 and IgG4, that does not activate complement). Moreover, a critical density of IgG binding to a surface is required to allow two adjacent Fc regions to engage the first protein of the cascade, named C1q, and initiate the CP (Giuntini et al., 2012; Lewis & Ram, 2014). The C1q is a 460 kDa hexameric flexible protein that is assembled from six heterotrimeric collagen-like fibers, each one prolonged by a C-terminal globular domain, responsible for its recognition function (Gaboriaud et al., 2003; Kishore et al., 2004). The main characteristic of this domain lies in its ability to engage a broad variety of ligands. Although, the C1q is classically known for its ability to bind IgG- and IgM- of the immune system, it was discovered that it recognizes the lectin SIGN-R1, C reactive protein, and other pentraxins bound to pathogens and other surfaces, as well as various molecular motifs on several Gram-negative bacteria and viruses (Cooper, 1985; Kang et al., 2006; Kishore et al., 2004; Szalai et al., 1999; Thielens et al., 2002). However, it is well known that IgM or IgG immune complexes are the best physiological C1 activators, especially in the presence of C1-inhibitor. Although it has been thought for a long time that C1q binds to IgG Fc domain and that activation requires multivalent binding, until recently the molecular details of how this can happen have remained poorly understood. Diebolder and colleagues demonstrated that some IgG mutations strongly influenced C1q binding and C1 activation, like the E345R found as a general C1 activation enhancer for all the IgG isotype variants (Diebolder et al., 2014; Idusogie et al., 2000; Kellner et al., 2014; Moore et al., 2010). Moreover, Diebolder also showed a very efficient C1 activation through an Fc-hexamer dependent clustering of the IgG on the bacterial surface. The model proposed, solved by Cryo Electron Tomography (Cryo-ET), has one Fab arm of each IgG on the target surface while the other Fab arm lying on the same central plane as the clustered Fc platform (EMDB entry: 2507) (Figure 1.7A and Figure 1.7B). This positioning could be envisaged to provide more degrees of freedom for the Fc segments, allowing their optimal positioning for C1q recruitment (Diebolder et al., 2014; Gaboriaud et al., 2014).

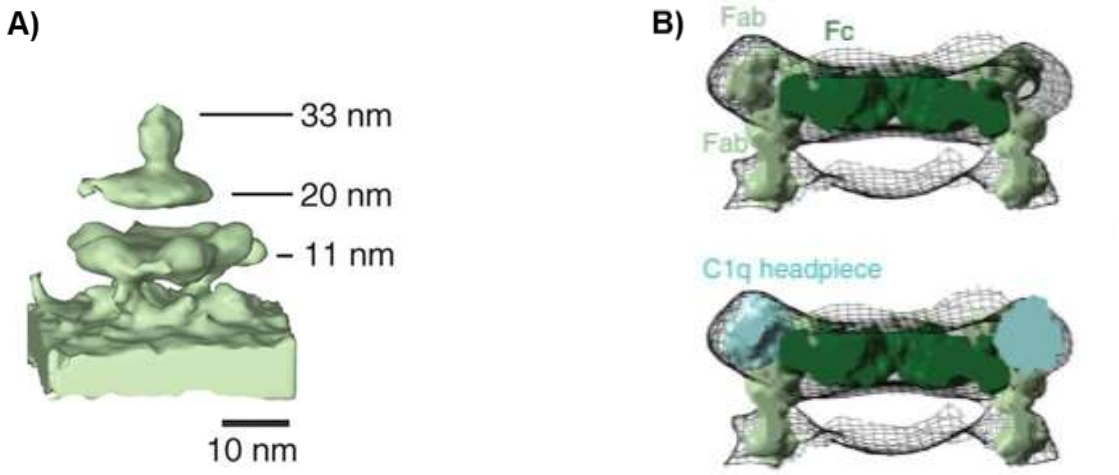

Figure 1.7: Model proposed in the work of Diebolder et al. that show the very efficient C1 activation through IgG Fc-hexamer dependent clustering on the bacterial surface. A) Isosurface of the subtomogram average of antibody-C1 at >6 nm resolution. The distances to the membrane center are indicated as heights (EMDB entry: 2507). B) Side view of the model of the lower Cryo-ET platform with the hexamer of the IgG-b12 structure (PDB: 1HZH) located into the six-fold symmetrized density (top) and with docked C1q headpieces (bottom). Images were taken from Diebolder et al., 2014.

Moreover, the structure of the deglycosylated IgG4 Fc further supports the hypothesis of a possible generic Fc assembly, which is stabilized by this E345R mutation (Davies et al., 2014). These models are in agreement with an evolutionary relationship between IgM and IgG in triggering complement. IgM, in fact, exists in a polymeric state with the C1q binding sites normally hidden and then exposed when the antigen is bound. On the contrary, IgG normally exists in a monomeric state with C1q binding sites exposed but with an affinity for the C1q too low to allow an adequate binding (Burton, 1986; Czajkowsky & Shao, 2009; Feinstein et al., 1986). The model from Diebolder is nonetheless compatible with observations that smaller IgG complexes may suffice to initiate some complement activation (Borsos & Rapp, 1965; Rosse et al., 1967). In the context of activation of the complement pathway, the interesting and poorly understood phenomenon named cooperative bactericidal activity between monoclonal antibodies (mAbs) allows two different mAbs that lack bactericidal activity alone, to induce bactericidal titers in the SBA assay only if present together. The work of Beernink *et al.*, demonstrated that some antibodies against the antigen fHbp were able to cooperate on strains with low fHbp expression to induce the bacteriolysis describing a mechanism that needs sufficient recruitment of the C1q molecules to activate complement-mediated bactericidal activity (Beernink et al., 2008). The investigation of the molecular basis of the cooperative

bactericidal activity is fundamental to understand how the complement has evolved to become activated by low number of copies of antigen on the bacterial surface.

Thus, using a case study of some couples of fHbp mAbs, as previously described in literature (e.g. the work of Beernink *et al.*, Giuntini and collaborators, Faleri and co. workers), it is possible to investigate mAbs' synergic rules focusing on the following variables: i) the ability of the antibody to block fH binding to the bacterial surface (since it was demonstrated that antibodies blocking fH binding show greater bactericidal activity) (Giuntini et al., 2011) ii) The differences between the subclasses of the mAbs (murine IgG3> IgG2a/b; human IgG3>IgG1>IgG2 (Giuntini et al., 2012) iii) presence of antibodies directed against distinct fHbp epitopes iv) the amount of fHbp expressed on the bacterial surface (epitope density) (Giuntini et al., 2011; Serruto et al., 2012).

1.2 The structural vaccinology era

Vaccination has been defined as a conviction of the immune system to treat a noninfectious substance that has been artificially introduced as an invading pathogen raising an immune response. Ideally this mechanism would protect the vaccinated from future infection inducing an immune response equal or better than that caused by natural infection. The main feature of vaccination is a long-term immunity against the pathogen preventing the individual from the disease and thus the transmission of the pathogen between humans. This contributes to the entire society protection and it is believed to save at least 2-3 million lives per year worldwide (Delany et al., 2014; Liljeroos et al., 2015). The starting point of vaccines began with the germ theory of Pasteur, Koch, Ramon and Mèrieux that leaded the development of vaccines based on lived attenuated or inactivated (killed) pathogens and on inactivated toxins (toxoids). These vaccines protected against rabies, diphtheria, tetanus, pertussis and tuberculosis in infant. Subsequently in the second half of the 20^{th} century, the innovation in cell culture technologies allowed the production of effective inactivated vaccines to prevent polio (IPV) and hepatitis A, and live attenuated vaccine against polio (OPV), mumps, rubella, measles (MMR), rotavirus, and varicella. In the meanwhile the progress in microbiology resulted in the development of polysaccharide vaccines against some strains of pneumococcus and meningococcus (Delany et al., 2014). In the 1970s, glycoconjugate and recombinant subunit vaccines revolutionized the field with the production of safer and more effective vaccines. *Haemophilus influenza*, pneumococcus and the meningococcus types A, C, W and Y are examples of very effective glycoconjugate vaccines (Delany et al., 2014;

Liljeroos et al., 2015). Moreover, the recombinant DNA technology was quickly adopted in the vaccine field enabling the large scale production of single protein from pathogens and their modification in order to optimize proteins for vaccine use. The recently licensed 4-component vaccine against *Neisseria meningitidis* serogroup B (Bexsero®) is an example of these improvement (Liljeroos et al., 2015). The innovative approach of the RV allows to identify potentially surface-exposed proteins starting from the genome rather from the cultures (Rappuoli, 2001). The RV that integrates bioinformatics tools for the identification of the vaccine candidate with the implementation of the speed of DNA sequencing has already been used to fight several pathogens, mainly bacteria and recently also for herpes simplex virus (Chiang et al., 2015; Maione et al., 2005; Montigiani et al., 2002; Naz et al., 2015; Talukdar et al., 2014; Wizemann et al., 2001; Xiang & He, 2013). The rational direct evolution of RV is named Structural Vaccinology (SV) and is based on the idea that protective determinants can be used to selectively engineer the antigen that can be re-designed, simplify and included in vaccine combination. This method is the results of a multidisciplinary and interdependent approach that includes experimental methods like X-ray crystallography, electron microscopy and mass-spectrometry, and computational methods like structural modeling, computational scaffold design and epitope prediction (Liljeroos et al., 2015). The final objectives of this rational structure-based antigen optimization are the facilitation of a faster industrial-scale production, the achievement of a greater immunogenicity, an increased safety profile and a broadly protection (Cozzi et al., 2013) . Since many years, structural biology has been used in the pharmaceutical field to determine the 3D structures of druggable proteins and to identify and inspect the sites where small molecules might bind (inhibiting or activating) a target protein. Based on the structure of target protein, important drugs directed at the active sites of enzyme have been successfully development, such as the inhibitors for HIV-1 protease or the influenza virus neuraminidase (Harrison, 2004; Kaldor et al., 1997; Kim et al., 1997). Nevertheless, the structural biology plays a key role in the fragment-based drug discovery allowing the rational design of new small molecule inhibitors (Scott et al., 2012). Moreover the developments in the proteomics and genomics field for protein structure determination, as well as the growing number of different technologies able to determine the 3D structure of proteins leaded to an increased number of available structure that aimed to expand the knowledge of the molecular architecture of possible vaccines candidates (Cozzi et al., 2013). Ultimately, SV could be considered a powerful tool to modify and rationally design existing vaccine antigen in order to improve their immunogenicity. Practically, after the structure generation of the whole protective antigen, the target domains can be identified

and the protein topology defined. The identification of the most immunogenic regions on the antigen is the main step. This is performed through the epitope characterization and epitope mapping using neutralizing antibodies (Cozzi et al., 2013). The term epitope mapping indicates the experimental methods used to obtain information on the epitope location onto the antigen like X-Ray crystallography, NMR and Cryo-EM (Liljeroos et al., 2015). The first technique is probably the most powerful and important between all the methodologies, but it has the drawbacks of the crystals generation, the large amount of specimen, and the unpredictable timelines for the crystallization. For small antigens (<30 kDa), the alternative is NMR method. Nowadays, cryo-EM is an emerging approach allowing the generation of structures near atomic resolution requiring only micrograms of proteins and avoiding the crystallization step. Moreover, since images of individual molecules are obtained, computational methods can be used to reveal multiple states. Figure 1.8 shows the workflow of the Structural Vaccinology.

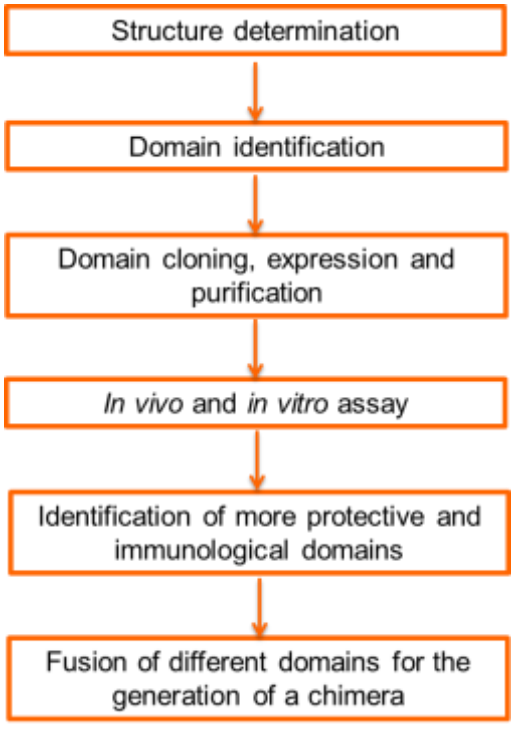

Figure 1.8: General workflow of the Structural Vaccinology approach. The image is adapted from Cozzi et al., 2013.

One of the most important examples where SV has been applied regards the fHbp protein of *N.meningitidis* group B. The very high amino acid conservation within each variant combined with the 3D structure of the full-length protein solved by both NMR and X-ray

crystallography and the mapping studies for the identification and localization of the protective epitope residues, consented a rational design of the three fHbp variants for a broader protective antigen (Cantini et al., 2009; Cendron et al., 2011; Mascioni et al., 2009; Scarselli et al., 2009). C-terminal domain that contains the majority of the protective epitopes was sub-divided into 10 different partially overlapping areas from 900 Å to 2000 $Å^2$ in order to determine in a fine-tune way the protective residues (Cozzi et al., 2013; Giuliani et al., 2005). The structure-based epitope mapping using variant specific mAbs revealed that the amino acids recognized located in non-overlapping regions between the variants (Scarselli et al., 2011). The final aim was to include in one of the variant, the crucial epitopes of the other two variants (Figure 1.9). fHbp variant 1 was used as a scaffold, introducing in various region of it specific residues from epitopes of var.2 and var.3.

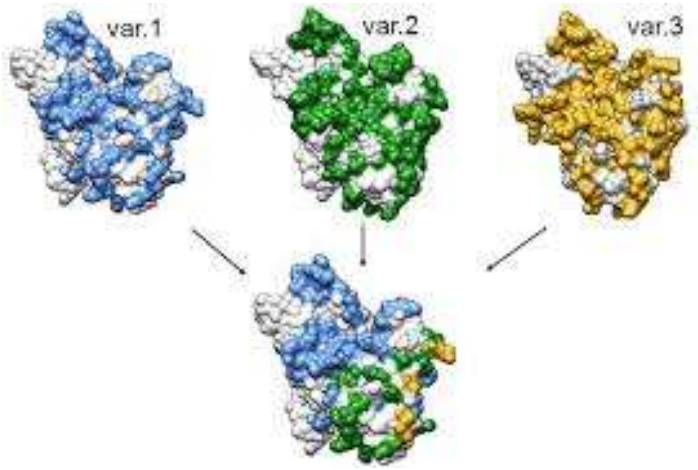

Figure 1.9: The structures of factor H-binding protein variants 1, 2 and 3 from N.meningitidis showed in the top were used to generate the chimera represented on the bottom. The different colors in the chimera referred to the single fHbp variants. The image was taken by Cozzi et al., 2013.

In light of the successful application of the SV approach, we can predict that this emerging field will lead a great improvement of the structural biology techniques as crucial tool for the development of future vaccines.

1.3 The electron microscopy

The structural visualization of macromolecules and macromolecular complexes is essential to understand the cellular mechanism and the function they are involved into. Nowadays Cryo-EM is emerging as a very powerful technique in the structural biology

field, as mentioned in the previous paragraph (Bai et al., 2015; Nogales, 2016; Nogales & Scheres, 2015; Valpuesta & Carrascosa, 2015). Defined as the Method of the Year 2015 by Nature, Cryo-EM is becoming a high resolution approach joining the two broadly used methods, X-ray crystallography and NMR. The first one is a very successful technique that provides atomic resolution whereas NMR can describe dynamics and interactions of the molecule studied. Unfortunately, the bottleneck of the crystallization step for the X-ray crystallography and the size limitations of the NMR have imposed restrictions in their applications to large complexes, integral membrane proteins and macromolecular assemblies with multiple states. Moreover, both the methods require a large amount of pure sample (Bai et al., 2015; Nogales, 2016). Thus Cryo-EM has come out as a structural technique suitable for challenging biological systems. The advantages reside in the need of smaller amount of sample, the feasibility to analyze large and flexible complexes with heterogeneous conformations and the possibility to have a not perfectly pure sample (Belnap, 2015; Nogales, 2016). The recent advancement in the instrumentation and software leads to the so called “resolution revolution” of the TEM field (Nogales, 2016). Particularly, during the last few years an explosion was detected in the Single Particle (SP) Cryo EM: many structures were deposited in the EM database and an increased number of them reported a map better than 4 Å of resolution (Figure 1.10) achieving recently the 2.2 Å released structure of the *E.coli* of β-galactosidase in complex with PETG (Bartesaghi et al., 2015; Nogales, 2016).

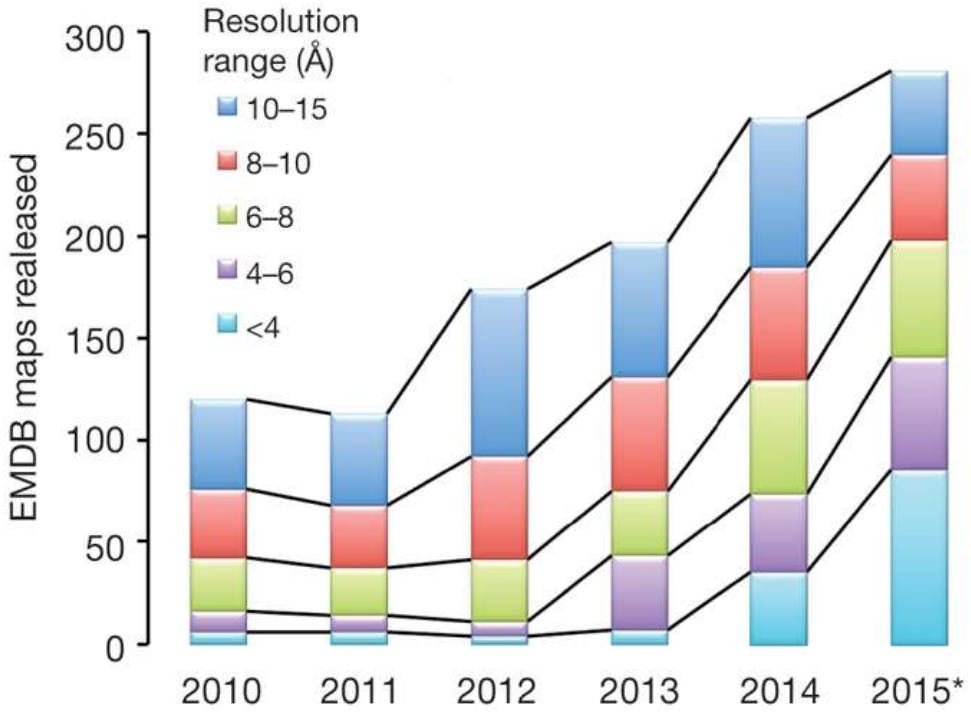

Figure 1.10: EM maps deposited in the Electron Microscope Data Bank EMDB (http://www.emdatabank.org/) in the last six years. The asterisk indicates that the data of the 2015 are incomplete because stopped in Oct, 14th. The image is taken by Nogales, 2016 (Courtesy of C.Lawson).

Khoshouei and colleagues calculated that 237 near-atomic resolution structures deposited in the DataBank in the 2015. These numbers reveal a great potentiality to grow for EM field (Khoshouei et al., 2016). The TEM is simply defined as a microscope that allows imaging a sample working with a beam of electrons that interacts with the specimen. As consequence the resulted TEM images, named micrographs, record the area-density and mass-thickness of the analyzed sample. This forms the 2D projections of the sample in which each point represents the sum of the density of the 3D object perpendicular to that point on the plane (Belnap, 2015). A brief overview of the TEM workflow and the SP reconstruction methodology is described below with references to the technical upgrade that characterizes this revolution (Figure 1.11).

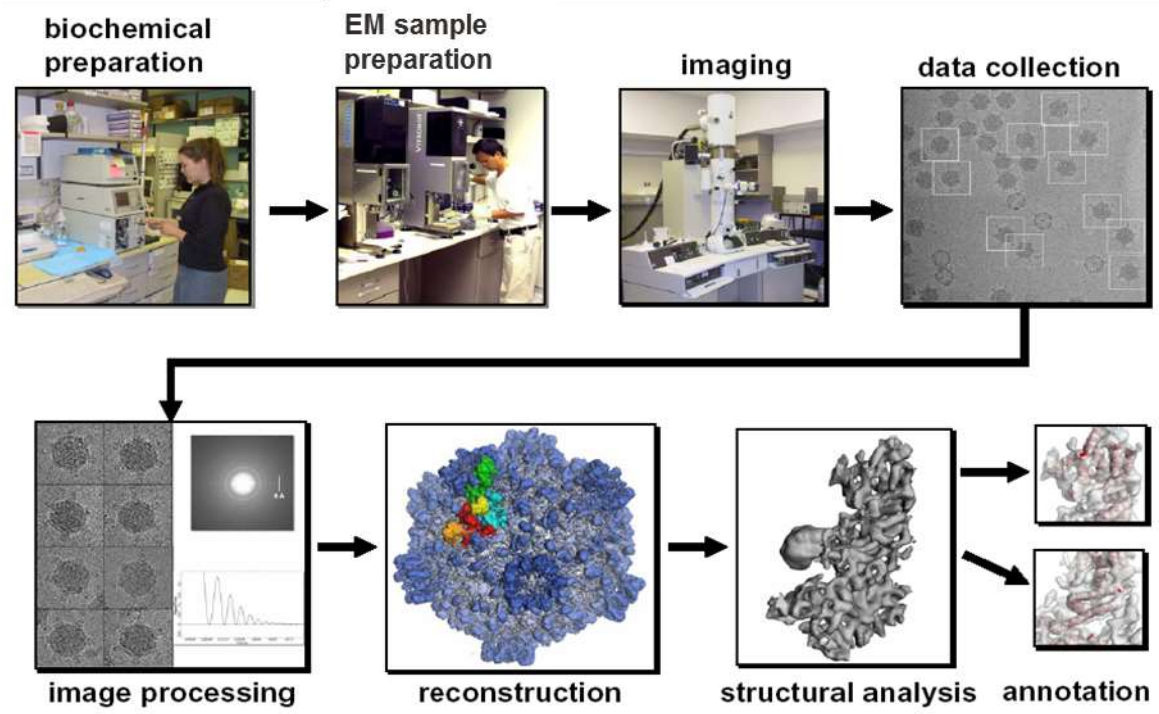

Figure 1.11: TEM workflow from the biochemical preparation to the final 3D reconstruction. Courtesy of Dr.Ferlenghi I.

Biochemical preparation: Biochemical tools are applied to purify the biological samples. A high level of purity is necessary to generate a homogeneous sample containing only the particle to be analyzed. The structural heterogeneity, due to molecule aggregation or molecule breakage should be minimized to generate an ideal sample for the following SP analysis and structure determination.

TEM sample preparation: The specimen used is a purified sample that is deposited on a carbon film with a support structure, commonly a copper or a nickel grid. There are several techniques for the TEM sample preparation depending on the type of specimen analyzed and on the scope of the analysis. As the contrast of the biological sample is too poor for the human eye to easily differentiate its features, in order to improve contrast several techniques are used. In electron microscopy, staining is usually done with heavy metal salts commonly derived from molybdenum, uranium, or tungsten. Heavy ions are used because they will readily interact with the electron beam and produce phase contrast thus enhancing significantly the low intrinsic contrast of macromolecules for the higher density of the heavy metals (Belnap, 2015) (Figure 1.12A). It is quite rapid and very useful for both qualitative analysis of the state of the sample and for a preliminary structural analysis of the specimen as prelude to more detailed investigation by Cryo-EM (Booth et al., 2011). The limitation of the negative staining is related to the fact that the stain shows

only the surface features, proving few information of the internal structure (Belnap, 2015). The resolution is believed to be limited by the dimension of the stain particles resulting in a 3D final map of low resolution (i.e. up to ~20 Å) (Wang & Sigworth, 2006). For the 3D reconstruction a common disadvantage can come from the flattening induced by the staining dehydration resulting in a geometrical distortion. Nevertheless different 3D EM models generated using negative staining demonstrated a perfect correspondence with known structures (Harris et al., 2001; Steven & Navia, 1980; Stoops et al., 1992). Another common drawback regards the adsorption of the sample onto a support in a limited number of preferred orientations that leads to loss of information. In this case, Random Conical Tilt (RCT) is an approach that provides different views of the molecules through tilted images and is a robust method for determining a reliable initial model (J. Frank, 2009; Ohi et al., 2004). Cryo-EM is a method for the sample preparation that preserved the specimen through a fast freezing in a thin layer of amorphous or vitreous ice, a non-crystalline form of solid water (Figure 1.12B).

Figure 1.12: EM technique for sample preparation. A) Negative staining: a particle deposited on a support is surrounded by staining. B) Cryo-EM: a particle is embedded in a vitreous thin layer. This image is taken from http://life.nthu.edu.tw/~labcjw/BioPhyChem/EM/bbsem.htm.

This technique avoids dehydration or support adsorption resulting in a close to native state of the target molecule, as demonstrated by the study performed on the catalase frozen hydrated crystal (Bai et al., 2015; Belnap, 2015; Ohi et al., 2004; Taylor & Glaeser, 1974). Care has to be taken to minimize the exposure of liquid nitrogen layer to the air to avoid ice contamination (Cheng et al., 2015). Another important parameter in the Cryo-EM sample preparation is the thickness of the ice: a very thick ice results in a low Signal-to-Noise Ratio (SNR) that prevents the sub-nanometer resolution (Henderson, 1995). Particles that are not reasonably visible should not be used for a 3D EM map generation (Cheng et al., 2015). Although the outstanding resolution results obtained with Cry-EM, there are some drawbacks: the low SNR of the biological sample and the degradation and radiation damage of the structural integrity of the specimen. The high vacuum, in fact, needed for avoiding the air-electron scattering degrades the sample as well as the

radiations break the chemical bonds of the molecules with the energy deposited by the electron beam. It's for this reason that at the beginning the specimens were dehydrated or chemically fixed (Bai et al., 2015).

Imaging & data collection: The sample prepared onto the grid is inserted in the TEM and the micrographs collection starts. A key role to target a good structure resolution is played by the high quality images (i.e. high contrast and sufficient resolution) and subsequently by the technical improvements in the new microscopes, detectors and software for image acquisitions. In fact, microscopes as Titan Krios working at 300 kV increase the acceleration voltage used and optical performance (Glaeser et al., 2011; Veesler et al., 2013; Zhang & Zhou, 2011). A crucial improvement regards the new detectors, Direct Detectors (DD). This innovative generation of detectors through the use of a new technology, the Complementary Metal-Oxide Semiconductor (CMOS), records the electrons without the conversion into photon that is a characteristic of the well-known Charge-Coupled Device (CCD) (Kuhlbrandt, 2014). The incident electrons pass through a very thin semiconductor membrane where they deposit energy directly detected by electronics fabricated on the membrane (Bai et al., 2015; McMullan et al., 2009). This greatly increased the capability of the DD of detecting the SNR of the incoming signal, defined as Detective Quantum Efficiency (DQE), in comparison with CCD and photographic films (Ruskin et al., 2013). DD also possesses a fast readout that allows to record movies composed by multiple frames permitting the correction for beam-induced sample motion and stage drift and thus the image blurring (Brilot et al., 2012; Shigematsu & Sigworth, 2013). This permitted to produce a great number of high resolution reconstructions of molecules in the MDa mass range (Allegretti et al., 2014; Amunts et al., 2014; Fernandez et al., 2014; Voorhees et al., 2014; Wong et al., 2014) and even complexes considered as too small for single particle (Cao et al., 2013; Liao et al., 2013; Lu et al., 2014). Types of these detectors are: DE (Direct Electron), Falcon (FEI) and K2 (Gatan). Another great improvement is given by the Volta Phase Plate (VPP) that is a continuous, amorphous thin carbon film located in the back-focal plane of the objective lens. Its activation increases the phase contrast facilitating the observation of weak phase object with markedly improved contrast (Khoshouei et al., 2016). It was demonstrated by Khoshouei and co-workers using a relatively small protein (257 kDa) that the VPP allows to recognize the particles and push the resolution to 4.4.

Image processing & reconstruction: A significant part of EM procedure is the image processing, in which a key tool is the development of good software (Cheng et al., 2015). Between the different methods available, the SP reconstruction is the most popular.

Developed by Joachim Frank and co-workers, it deals with “single particle” (the biological sample) that assume random or multiple orientations on the grid (Joachim Frank, 2006; Nogales, 2016). Following the scheme reported in the Figure 1.13 (left panel), the SP reconstruction workflow can be divided four main steps to generate a final 3D volume: preprocessing of the micrographs, particle picking, 2D classification and 3D reconstruction.

- **Micrographs processing:** The processing starts with the import and evaluation of the quality of the micrographs. This determines the goodness of the reconstruction. All the modifications that are introduced by the microscope in the ideal projection resulting in the EM image are characterized by the Contrast Transfer Function (CTF). The correction of the CTF must be done on each image in order to reject micrographs with strongly asymmetric ring (astigmatism) or ring that fade in a particular direction (Carazo et al., 2015).
- **Particle picking:** Once the dataset is collected and good micrographs selected, particles can be selected and extracted. Some processing can be performed during the extraction such as filtering. The quality of the particles is a critical point for the final reconstruction because the inclusion of a huge number of bad particles may preclude the structure determination (Cheng et al., 2015). This can now be performed by algorithm that produces a score regarding the goodness (e.g. z score) (Vargas et al., 2013). Particles can be selected in a manual, semi-automated or fully automated manner. When the particles are localized, they should be windowed (boxed) and assembled into a stack.

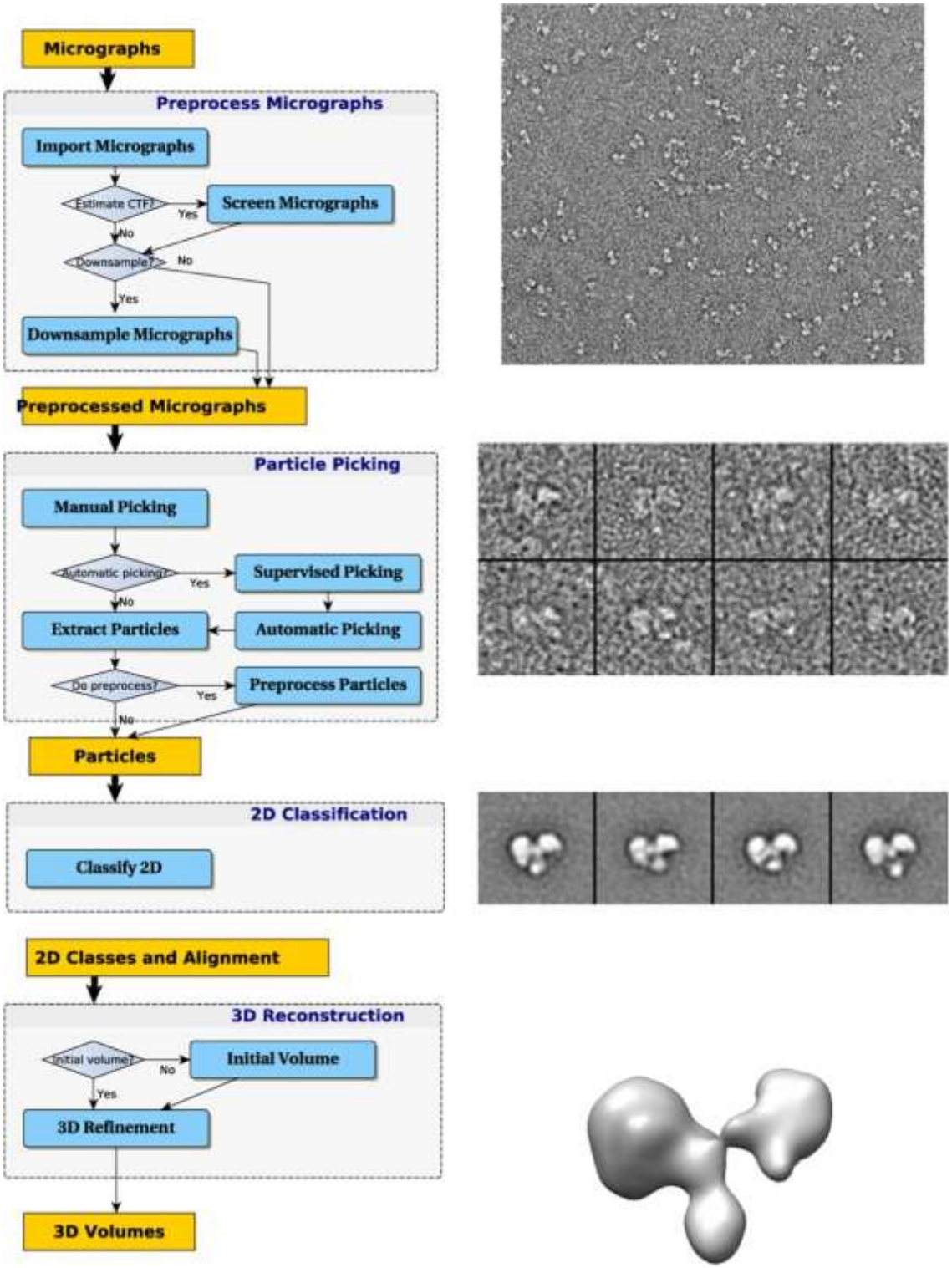

Figure 1.13: Single particle EM workflow. Panel represents the different steps (on the left) and a practical example of the procedure (on the right). This image is a courtesy of Nunez-Ramirez et al., 2011 published on Carazo et al., 2015.

- **2D classification:** A crucial step is the 2D analysis. In particular the alignment and the grouping in homogeneous subset, named classification. This reveals the

presence of invalid particles, image artifacts or empty fields that need to be removed, it highlights the presence of few views that will conduce to an unsuccessful 3D analysis and it verifies the presence of high quality classes with high SNR necessary for the computational determination of 3D structure (Cheng et al., 2015).

- **3D reconstruction:** The calculation of an initial model from the different classes is performed *ab initio* if no reasonable template or guesses for the structure exist. This first model should contain the main features of the 3D object at low resolution. The subsequent step is the refinement of the initial map obtained. All the refinement methods available in the packages are based on the 3D projection matching procedures that modifies the orientation parameters of single particle images (projections) to achieve a better match with the re-projections computed from the approximation of the structure (Cheng et al., 2015). This leads to the final 3D map.

  To monitor the progress of the refinement, an indicator is the Fourier Shell Correlation (FSC). It indicates the level of SNR as a function of the spatial frequency and the resolution of the map. "Resolution" is however arbitrarily chosen by a cut-off level of the SNR or FSC curve. Three are the main definitions: the spatial frequency at which the FSC curve is 0.5, the spatial frequency at which the SNR is 1.0 (corresponding to an FSC of 0.33, point at which the power of the signal is equal to the power of the noise). Another choice is FSC=0.143, selected based on relating EM results to those in X-ray crystallography. It is important to keep in mind that the quality of an EM map is described by the whole FSC curve, not just the resolution, and there are EM maps with the same nominal resolution that differs significantly in the overall quality. In turn, the reported nominal resolution reflects the overall resolution of the entire density map without describing the local variation (Cheng et al., 2015; Ludtke & Serysheva, 2013)

.

There are different image analysis methodologies that were implemented during the years in well-known software packages, such as SPIDER (Joachim Frank et al., 1981), EMAN2 (Tang et al., 2007), XMIPP (Marabini et al., 1996), IMAGIC (Marin van Heel & Keegstra, 1981), FRIALIGN (Grigorieff, 2007). Among the others, Scipion is a new software emerging for facilitating the interoperability between different packages and for the exchanging of data ((Marabini et al., 2013) all the details will be explained in the manuscript by de la Rosa-Trevin *et al*., in press). The fundamental importance of this

interoperability in the 3D reconstruction is the possibility to easily use tools from different packages overcoming the weakness of each software.
Moreover the software allows the traceability of every step performed during the analysis. This characteristic joined with a user friendly graphic interface will allow to spread EM and to grow always more.

fHbp – a case study of cooperative bactericidal activity

Chapter 2

2.1 Introduction

The complement system plays a crucial role in innate immune defense against pathogenic infection. Initiation of the complement cascade occurs through one of three pathways, classical (CP), lectin or alternative (AP) and leads to cleavage of the protein C3 into C3b by C3 convertases. The formation of an activate C3 that exposes reactive thioester is a key feature in this system; it triggers the deposition of C3b on the surface of an invading pathogen and results in its elimination through phagocytosis or lysis following the assembly of the Membrane Attack Complex (MAC) (Walport, 2001a, 2001b). The activation of complement within the host must be precisely regulated as inappropriate and/or excessive activity can damage host cells (Liszewski et al., 1996). Several factors are responsible for down-regulating complement activation *in vivo*. Soluble down-regulators are present in the systemic circulation and at mucosal surfaces, while other molecules that reduce complement activation are expressed on cells to prevent local deposition of complement factors. The fH particularly is the main regulator of the AP, which is the only pathway triggered spontaneously and everywhere in the organism (Ferreira et al., 2010) (Figure 2.1).

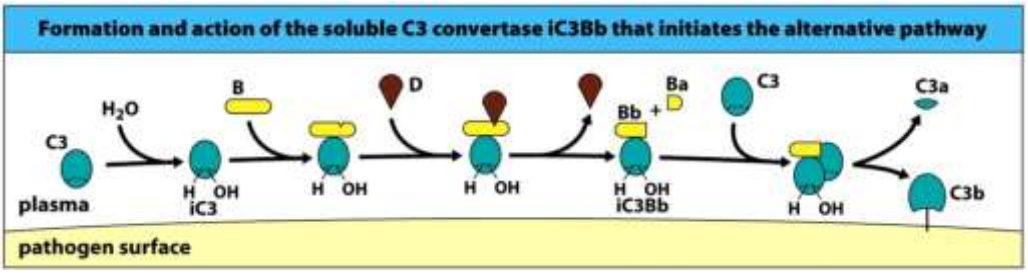

Figure 2.1: Alternative pathway scheme. Image is taken from Atkinson et al., 2006.

The fH is one of the three recognition molecules, which together with the properdine and C3b acts to identify the host or target (Ferreira et al., 2010). It inhibits the AP in three ways i) by accelerating the dissociation of C3bBb, ii) acting as cofactor for factor I (fI)-mediated inactivation of C3b, and iii) competing with factor B (Muller-Eberhard, 1988; Walport, 2001a). The factor H is a 155 kDa soluble glycoprotein present in the secretions of the nasopharynx. It is composed of 20 homologous Complement Control Protein (CCP) domains that in the electron microscope give factor H the appearance of flexible “beads on a string” with the ability to fold back on itself (Aslam & Perkins, 2001; DiScipio, 1992; Kristensen et al., 1986; Perkins et al., 1991; Ripoche et al., 1988; Sim & Perkins, 1990). Since its crucial role in the complement regulation, numerous pathogens, like

N.meningitidis, have the capacity to interact with fH to confer resistance to the alternative pathway (Ferreira et al., 2010). The fHbp was demonstrated by Madico and collaborators to be the principal fH-binding meningococcal protein (Madico et al., 2006). The structure of fHbp-fH (domains 6 and 7, called fH67) complex has been solved and refined to 2.35 Å (PDB entry: 2W80), reviling that the contact area is extensive and involves mainly the β-barrels of fHbp and the fH CCP6 with several minor contacts to CCP7 (Schneider et al., 2009) (Figure 2.2). The interaction buries a surface area of ~2860 Å and creates a high affinity binding (~5 nM) (Scarselli et al., 2011; Schneider et al., 2009) .

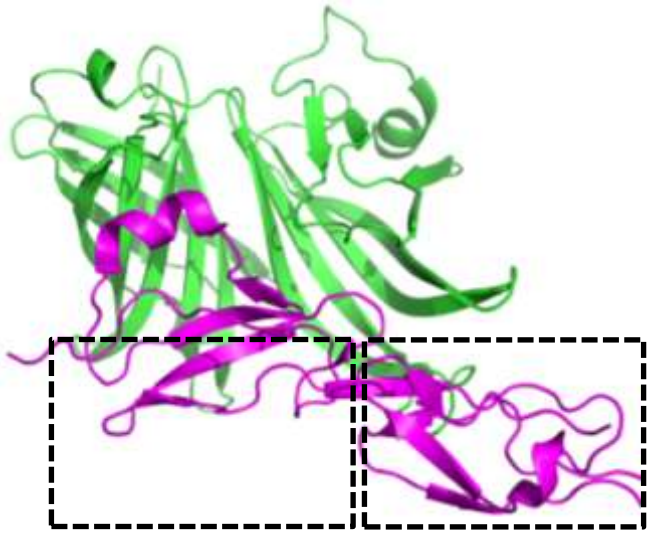

Figure 2.2: Model of recombinant fHbp (green colored) complexed with the fH CCP 6 and CCP7 (violet colored). The contact zones are highlighted with dotted boxes. The image is an adaptation from the 2W80 PBD structure (Schneider et al., 2009).

The high affinity binding between the fHbp and fH has implication for fHbp role as a virulence factor *in vivo* because it allows sequestering the fH present in the plasma. The fHbp protein is considered as unique candidate antigen since anti-fHbp antibodies can elicit protection using two different mechanisms: direct complement-mediated killing of the bacterium, or blocking fH binding to increase susceptibility of the bacteria to the alternative complement pathway killing (Madico et al., 2006; Seib et al., 2015). In this case, an increased susceptibility of the bacteria to the complement mediated bactericidal activity results from the inhibition of the fHbp binding to fH (Giuntini et al., 2012; Konar et al., 2013). Moreover the site of the recombinant fHbp var.1 holding the binding location for human fH is the target of most of the murine mAbs characterized to date (Beernink et al., 2009; Beernink et al., 2008; Malito et al., 2013; Scarselli et al., 2009). However the binding of fH to fHbp is specific for human and for some nonhuman primate fH (Beernink et al., 2014; Granoff et al., 2009); it is believed that the vaccine antigen can form a

complex with fH (Beernink et al., 2015). As a confirmation, recent studies demonstrated that in immunized human, in fH transgenic mice and in infant rhesus macaques, the binding of fH to the fHbp skews the anti-fHbp serum antibody repertoire to epitopes outside the fH binding site. These results suggest that these antibodies have lower complement-mediated bactericidal activity than the mAbs able to block the formation of fH-fHbp complex. Since the fundamental mechanism of serum-induced protection in human is still poorly understood, to investigate the anti-fHbp repertoire of immunized humans, Beernink and collaborators cloned the heavy- and light- chain immunoglobulin variable-region genes from individual peripheral blood plasmablast cells from three humans immunized with a licensed MenB-4C vaccine (Beernink et al., 2015). They observed a lack of inhibition of the fH-fHbp binding, but interestingly most of the characterized anti-fHbp fragment antigen binding (fab) enhanced the human fH binding. On the basis of this enhancement, they reinforced the idea that the anti-fHbp bactericidal activity depends largely on the classical complement pathway since the fH is a down regulator of the alternative pathway. This prediction was proved incorrect in that the block of the formation of the C3 convertase (C3bBb), specific for the activation of alternative pathway, decreased the bactericidal activity (Beernink et al., 2015). Thus, all these recent evidences suggest a more complicated and different protection mechanism for human mAbs than the one predicted with mice mAbs.

The involvement of the classical complement pathway in the bacterial killing is certain. This pathway is initiated by the binding of antibodies to their target antigen that induce a conformational change in the Fc portion of the mAbs thus enabling the engagement of the C1q that leads to the activation of the complement pathway (Lewis & Ram, 2014). Although the molecular basis of the recruitment of the C1q is still mostly unknown, lots of efforts have been done to elucidate this event. Recently has been demonstrated that chimeric IgG anti-fHbp mAbs, irrespective of IgG subclass and thus their ability to activate CP, showed a greater bactericidal activity against mutant strain of *N. meningitidis* with increased fHbp expression than against the wild-type strain (Giuntini et al., 2012). A potent complement activation by mAbs was demonstrated to be restricted to certain antigens and epitopes (Bindon et al., 1988; Cragg & Glennie, 2004), presumably because antigen size, density and membrane fluidity may affect activation (Cragg & Glennie, 2004; Diebolder et al., 2014; Hughes-Jones et al., 1985; Parce et al., 1983; Teeling et al., 2006; Xia et al., 1993) and because IgG orientation resulting from epitope geometry imposes additional structural constrain (Bindon et al., 1988; Cragg et al., 2003; Pawluczkowycz et al., 2009; Teeling et al., 2006). Diebolder and colleagues reported that an ordered IgG

hexamer formation, via specific non-covalent interaction between Fc segments, after antigen binding on the cell surface, triggers the complement activation (Diebolder et al., 2014). In this intricate and not well understood biological context, the study of the interesting bactericidal phenomenon, named cooperative bactericidal activity, could reveal a thorough understanding in the molecular basis of the antibody-based mechanisms of complement activation. This mechanism, still mostly unknown, showed that pairs of murine mAbs that individually lack bactericidal activity are able to elicit bactericidal activity if mixed together (Beernink et al., 2008). Using murine mAbs, Beernink and co-workers tested the cooperative effect proposing a model for effective bacteriolysis of strains with low level of fHbp expression that are normally resistant to antibodies killing. The author postulated the inhibition of the binding of fH as necessary but not sufficient for cooperative bactericidal activity. In contrast, the recent findings regarding the human repertoire of mAbs outside the fH binding site strongly suggested a different mechanism for human mAbs cooperativity from the one hypothesize for murine cooperative activity. Moreover two murine mAbs that recognize a wild panel of variants and subvariants of fHbp have been reported to have bactericidal activity only if they are used in combination (Faleri et al., 2014; Vu et al., 2012). All these finding suggest that the ability of mAbs anti-fHbp to efficiently promote complement-mediated killing relies on the affinity and configuration of binding to the antigen, leading to efficient engagement of C1q (Seib et al., 2015). The study of the geometrical relationship between the antigen and the antibody could therefore play a key role in the elucidation of the cooperative bactericidal mechanism. The connection between physical parameters of non-covalent binding, as the interaction between mAbs and other molecules, and parameters of biological function such as immunogenicity was already explored (Greenspan & Bona, 1993). One of the factor that affects the interaction is the three dimensional geometry of the whole immune complex that is influenced by both the topological locations of reactive sites and the segmental flexibility of the reactants. A description of structural differences of some immune-complexes was performed in the 1993 by Roux using immunoelectron microscopy (Roux & Greenspan, 1994; Roux & Tankersley, 1990; Shoenfeld et al., 1997). By characterizing the structure and the kinetics of different monoclonal antibodies reacting with a target idiotype, they found that the geometric bivalent interaction is the one energetically favored unless inhibited by restrictions (Roux, 1999; Roux & Tankersley, 1990). MAb affinity for the antigen is another important feature that plays a role in measuring the stability of the complex. A “locked” conformation formed between the antigen and the antibody is the result of the high affinity binding whereas a less constrained complex (such as ring

tetramers) is obtained with low affinity binding (Roux, 1999). Finally i) the investigation of the geometrical relationship of the antigen-antibodies complex, ii) the possible constraints found for the efficient activation of the complement pathway and iii) the difference in the cooperative couple of murine and human mAbs, could reveal the structural basis of cooperative bactericidal activity thus shedding light on the antibody-based mechanisms of protection against bacterial disease.

2.2 Aim of the work

Revealing the structural bases of cooperative bactericidal activity by monoclonal antibodies is fundamental for a thorough understanding of antibody-based mechanisms of protection against bacterial diseases. Cooperative bactericidal activity occurs when mAbs, that are not individually bactericidal, become bactericidal when used in combination. This phenomenon was investigated on the meningococcal fHbp, a 27.5 kDa surface-exposed lipoprotein and one of the most important antigens present in the recently released vaccine Bexsero® for prevention of serogroup B *Neisseria meningitidis* infections (Seib et al., 2015; Serruto et al., 2012). To understand the structural basis of the cooperative bactericidal mechanism, we investigated firstly a cooperative couple of murine mAbs; then we proceed with biophysical and biochemical characterization of human cooperative mAbs to compare their characteristics with those of the murine ones analyzing the stability of the complex. Finally, a detailed biochemical and structural analysis was performed on both human cooperative and non-cooperative couples of mAbs to point out the different mechanisms of these opposite biological effect. In detail, we investigated on the influence of the flexibility and steric hindrance of the mAb molecules in the formation of the cooperative complex by using both mAb and fabs. We also explored the effect of the binding of the human fH on cooperative couples to give a greater picture of the mechanism of the mAbs cooperativity.

2.3 Experimental procedure

2.3.1 fHbp: cloning, expression and purification

The recombinant protein fHbp var. 1 (from strain MC58, UniProt Q6QCC2) full length was produced as fully previously described (Cantini et al., 2006; Masignani et al.2003).

The fHbp was expressed in the pET-21b plasmid (Novagen) in the *E.coli* strain BL21 (DE3) Star (Invitrogen) as a C-terminal histidine fusion lacking the N-terminal leader peptide and lipobox motif (Figure 2.3).

```
        10         20         30         40         50         60
MVAADIGAGL ADALTAPLDH KDKGLQSLTL DQSVRKNEKL KLAAQGAEKT YGNGDSLNTG

        70         80         90        100        110        120
KLKNDKVSRF DFIRQIEVDG QLITLESGEF QVYKQSHSAL TAFQTEQIQD SEHSGKMVAK

       130        140        150        160        170        180
RQFRIGDIAG EHTSFDKLPE GGRATYRGTA FGSDDAGGKL TYTIDFAAKQ GNGKIEHLKS

       190        200        210        220        230        240
PELNVDLAAA DIKPDGKRHA VISGSVLYNQ AEKGSYSLGI FGGKAQEVAG SAEVKTVNGI

       250
RHIGLAAKQL EHHHHHH
```

Number of amino acids: 257

Molecular weight: 27654.8

Theoretical pI: 6.9

Figure 2.3: Protparam analysis of fHbp var.1 sequence with a C-terminal histidine fusion and lacking the N-terminal leader peptide.

The growth was performed in DIFCO 3X medium and the cells were inducted with 0.25 mM IPTG for 5 hours at 25 °C.

The recombinant fHbp was purified from the biomass using a sonication protocol for the lysis followed by Ni^{2+}-affinity resine (His-Trap HP, GE Healthcare) *via* C-terminal 6x-His-tag and a cationic exchange chromatography step (HiTrap SP HP, GE Healthcare) in 50 mM Tris, pH 8.0 buffer.

The purity of the sample was assessed using densitometry analysis (over 98%) of sodium dodecyl sulfate polyacrylamide gel electrophoresis (SDS-PAGE) and Size Exclusion Chromatography-Ultra Performance Liquid Chromatography (SEC-UPLC) (99%) in 10 mM NaP, 400 mM $(NH_4)SO_4$, pH 6.0 buffer.

Protein concentration was determined using Bradford method (Protein Assay,Bio-Rad) and the BCA method (Pierce).

2.3.2 Antibodies: cloning, expression and purification of humAbs

The VH and VL gene fragments produced for the generation of human fabs in *E.coli* were optimized for mammalian expression by Geneart (Life Technologies) with the addiction of an Eco31I site at the gene extremities and an appropriate linker for single step cloning. The synthetic DNA strings digested with Eco31I restriction enzyme, were purified and DNA products ligated into human pRS5a Igγ1, Igκ and Igλ expression vectors (NIBR) containing a human Ig gene signal peptide sequence, the Eco31I cloning site upstream of the human IgG1, Igκ or Igλ constant regions, the CMV promotor for the transcription and the ampicillin resistance. The cloning was performed in *E. coli* strain DH5α, using standard ligation protocol.

Transient production of recombinant antibodies in suspension Expi293 (Life-Technologies) cells was performed according to manufacturer's protocol. Equal amounts (15 µg each/30 ml of transfection volume) of IgH and corresponding IgL chain expression vector DNA were used to transfect Expi293 cells. Cells were harvested centrifuging at 900 x g for 10 minutes to remove the cell debris and the supernatants collected 3 and 6 days after transfection and then filtered at 0.22 µm sterile filter PES Membrane (Millex-GP).

Recombinant antibodies were purified with Protein G beads (GE Healthcare) according to the manufacturer's instructions. Antibodies were eluted with of 100 mM glycine pH 3.0, collecting the eluates in tubes containing 1 M Tris pH 9.0. To assess the protein collected, 20 µl of the Flow Through (FT), the wash and the elution (ELU) fractions, in Non-Reducing (NR) and Reducing (R) conditions, were loaded onto a SDS-PAGE 4-12% Bis-Tris gel (Novex, Life Technologies) using MES 1X as buffer (Figure 2.4). The buffer of the elution fraction containing the desired mAb was exchanged to PBS. Recombinant antibodies were quantified by absorbance at 280 nm and their purity was assessed by SDS-page after coomassie staining.

A)

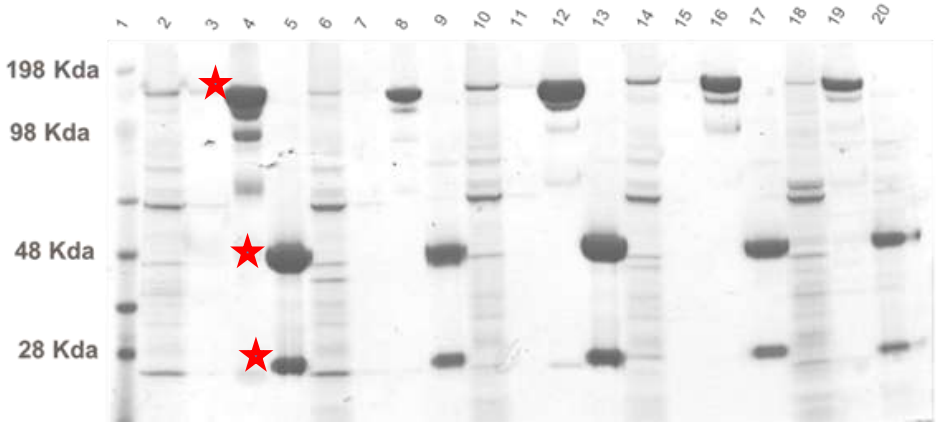

B)

lane	sample	lane	sample
1	Marker	11	7B10 ELU NR
2	1A3 FT	12	7B10 ELU R
3	1A3 WASH	13	2C1 FT
4	1A3 ELU NR	14	2C1 WASH
5	1A3 ELU R	15	2C1 ELU NR
6	1A12 WASH	16	2C1 ELU R
7	1A12 ELU NR	17	1G3 FT
8	1A12 ELU R	18	1G3 WASH
9	7B10 FT	19	1G3 ELU NR
10	7B10 WASH	20	1G3 ELU R

Figure 2.4: A) SDS-PAGE gel of the purification fractions of human mAbs anti fHbp var.1. The elution fraction is tested both in Non-Reducing (NR) and Reducing (R) conditions. Red stars indicate as example in the four and five lanes the band of the mAb in NR and R conditions, respectively. B) The table reported the loading order of samples in the SDS-PAGE gel.

2.3.3 Antibodies: cloning, expression and purification of hufabs

It is well known from literature that the antibodies are flexible and large proteins (Zhang et al., 2015). The latter characteristic implies that mAbs have a steric hindrance that could influence the reciprocal binding onto the antigen (Pellequer & Van Regenmortel, 1993). In order to understand the possible effects of both flexibility and steric hindrance of the mAb molecule in the formation of the complex, a couple of cooperative mAbs were generated as fabs. From a single isolated plasmablast from peripheral blood, the Heavy Chains (CH) and Light Chains (CL) of the Variable region genes of different fabs anti-fHbp var.1, encoded by unique germ line, were amplified separately and then joined by overlap extension PCR. Products were cloned into pET22 with Chloramphenicol resistance as bicistronic expression cassettes encoding for fab and sequenced (L. Liu and A. H. Lucas,

manuscript in preparation). The expressions were performed in *E.coli* strain Rosetta2 (DE3) (Novagen) in Enpresso B medium (Biosilta), according to manufacturer's instructions, and the induction was carried out with 1mM IPTG for 24 hours at 25°C. The biomasses produced were pelleted at 10000 x g for 20 minutes at 4°C and the surnatant discarded. After the lysis in CelLytic Express (Sigma-Aldrich) buffer 10 ml/g of wet biomass with the addiction of 10 mM imidazole for 30 minutes of incubation at Room Temperature (RT), the soluble fraction was obtained pelleting the lysate at 18000 g for 20 minutes at 4°C and filtrated using a 0.22 µm sterile filter PES Membrane (Millex-GP). The recombinant fabs were purified using a first step of Ni^{2+}-affinity chromatography with 1 ml His GravityTrap column (GE Healthcare). The elution was performed using 20 mM Tris-HCl, 300 mM NaCl, 250 mM imidazole, pH 8. A buffer exchange to 20 mM Tris-HCl, pH 8 was necessary to perform an anionic exchange chromatography step (HiTrap SP HP, GE Healthcare) using an automated AKTA Purifier System. The fabs were collected, concentrated using an Amicon- 15 Ultra (Amicon) 10 K and quantified by Bradford protein assay (Sigma-Aldrich). Their purity was assessed by SDS-PAGE after coomassie staining in NR and R conditions (Figure 2.5).

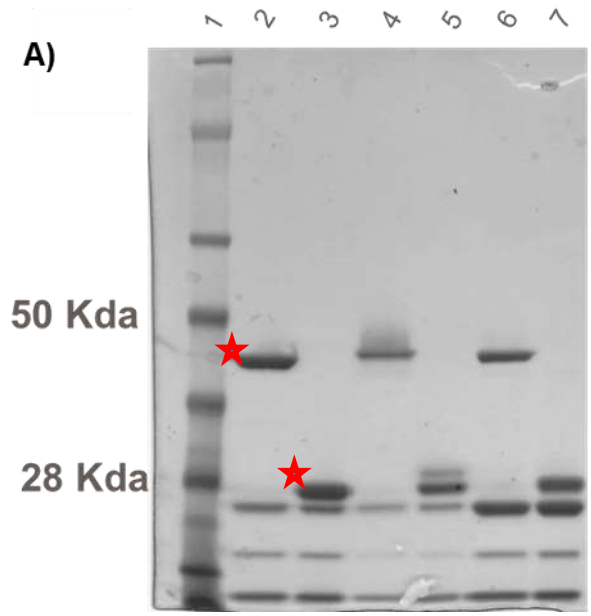

B)

lane	sample
1	Marker
2	7B10 NR
3	7B10 R
4	2C1 NR
5	2C1 R
6	1G3 NR
7	1G3 R

Figure 2.5: A) SDS-PAGE gel of the purified human fabs anti fHbp var.1 after the anionic exchange chromatography tested in Non-Reducing (NR) and Reducing (R) conditions. Red stars indicate as example in the second and third lanes the band of the mAb in NR and R conditions, respectively. B) The table reported the loading order of samples in the SDS-PAGE gel.

2.3.4 Antibodies: production and selection of the murine mAbs

The murine IgG1 isotype mAb30G4 was produced and purified by Areta International Srl as described by Malito *et al*, 2013; the murine mAb502 was prepared as detailed illustrated in Giuliani *et al*., 2005 (Giuliani et al., 2005; Malito et al., 2013).

Since mAbs able to induce complement mediated killing of bacteria are correlates with resistance to meningococcal meningitidis (Borrow et al., 2006; Goldschneider et al., 1969), the crucial characteristic of the selected monoclonal antibodies to study a cooperative phenomenon, was low or no bactericidal titer elicited when tested alone, but high titer when mixed together. The SBA titers of each mAb and pairs of mAbs were screened to find cooperative and non-cooperative couples. Secondly, high affinity of each mAb for the antigen was needed for the formation of a stable complex in order to characterize the structure in solution without the use of chemical cross-linking. Surface Plasmon Resonance (SPR) technique was used for detecting the parameters of the binding affinity. Third important discriminant feature was the epitope location of each mAb onto the protein. The data of this cooperative couple of murine mAbs were available in literature (Faleri et al., 2014).

2.3.5 Selection of the human mAbs and human fabs

The same selective criteria described above, were applied on the human mAbs. A combined approach of peptide array technology, peptide scanning analysis and sequence alignment allowed an approximate definition of each epitope. A more stringent selection was applied by using the capability of monoclonal antibody to recognize different variants. The cross reactivity locate the epitope of the mAb in a highly conserved region of the protein. The non-cooperative couples chose in this study are composed by one monoclonal antibody that recognizes only the var.1 and one that recognizes all the three variants of the protein. Figure 2.6 reports the summary of the characteristics.

mAb	SBA titer	Affinity var.1 (KD)	Epitope location
mAb1A3	<4	1.67 ± 0.39 E-10	Full length protein
mAb1A12	<4	1.78 ± 0.8 E-11	aa 319-434
mAb7B10	<4	0.93 ± 0.02 E-10	Full length protein
mAb2C1	<4	0.9 ± 0.05 E-11	aa 319-434
mAb1G3	<4	1.72 ± 0.03 E-10	Full length protein
Couple of mAbs	**SBA titers**	**Immunological Definition**	
mAb7B10+mAb2C1	2048	Cooperative	
mAb1A12+mAb1A3	512	Cooperative	
mAb1G3+mAb7B10	8	Non cooperative	
mAb2C1+mAb1A12	<4	Non cooperative	

Figure 2.6: The table reported the characteristics of the mAbs and the couples selected.

2.3.6 fHbp-antibodies: formation and purification of complexes

The complexes of the recombinant fHbp var.1 and the antibodies were formed incubating the desired mAbs or fabs in a molar ratio of 1:1 for 1 hour at RT with the recombinant fHbp var.1 in order to be in an antibody excess. The murine complex was then purified using a Superose 6 3.2/30 (GE Healthcare) in TBS (25 mM Tris, 150 mM NaCl, pH 8). Additional attempt was performed using a High Performance Liquid Chromatography (HPLC) equipped with Yarra3000 andYarra2000 (Phenomenex) in a mobile phase of 50 mM HEPES, 150 mM NaCl, pH 7. A Superdex 200 Increase 3.2/300 column (GE Healthcare) in 20 mM Tris, 300 mM NaCl, pH 8 and AKTA Micro system (GE Healthcare) were used to purified the human immune complex. Fractions of 0.05 µl were collected by Fraction Collector Frac-950 (GE Healthcare).

2.3.7 fHbp-antibodies: Surface Plasmon Resonance (SPR) for assessing cooperativity

A Biacore T200 instrument was used to show that simultaneous binding of the known cooperative couple of murine mAbs30G4 and mAb502 can be seen in a surface plasmon-based competition assay. Based on this result, couples of human mAbs were tested under similar conditions to discriminate biochemically cooperative and non-cooperative couples of mAbs (Abdiche et al., 2014). HBS-P (10 mM HEPES pH 7.4, 150 mM NaCl, 0.05% v/v Surfactant P20) was used as running buffer. As classical sandwich assay (Figure 2.7),

1000 RU of the desired mAb were immobilized on a CM-5 sensor chip using amine coupling chemistry, followed by injection of the recombinant fHbp var.1 (100 nM at 30 µl/min for a contact time of 1 minute). Equally, the second mAb was injected subsequently at the same concentration and flow rate. Sensorgrams were analyzed using Biacore T200 Evaluation 1.0 Software.

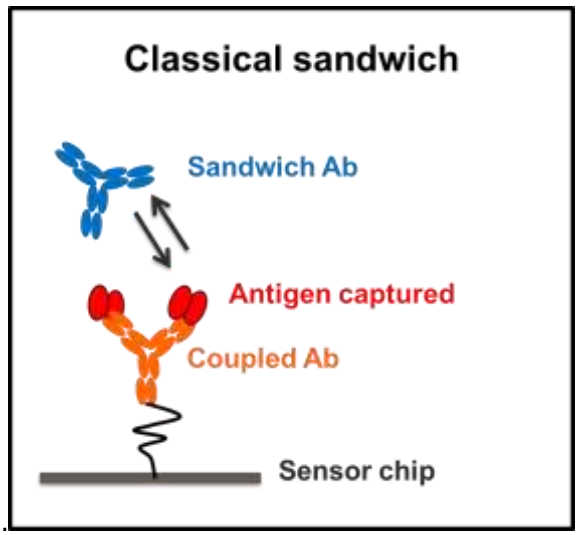

Figure 2.7: Scheme of the protocol used for the SPR binning experiment.

2.3.8 fHbp-antibodies: Surface Plasmon Resonance (SPR) competition assay with factor H (fH)

The human factor H was described as specific ligand for the antigen fHbp. To investigate the formation of a quaternary complex with the cooperative couples of human mAbs, the Biacore T200 instrument (Biacore) was used to perform competition assay with the human fH. The cooperative couples tested were the mAb7B10-mAb2C1 and the mAb1A3-mAb1A12. The same approach and conditions used for the discrimination between cooperative and non-cooperative couples (as described in the previous subparagraph) was applied for the competition assay with the fH. The capturing of the fHbp var.1 was performed on the CM-5 sensorchip covalently coupled with the mAb1A3, mAb1A12 and mAb7B10, followed by injection of second mAbs in order to form the cooperative complex. A concentration of 100 nM of fH was then injected at 30 µl/min. The sensorgrams were analyzed as previously described.

2.3.9 fHbp-antibodies: Hydrogen/Deuterium eXchange Mass Spectrometry (HDX-MS) analysis

An HDX-MS epitope mapping analysis has been set up to better characterize the human mAbs epitopes. The first step was to generate and separate peptides covering the full length protein in order to monitor the deuterium uptake in the entire sequence when the antigen is coupled with mAb. The fHbp var.1 (54 pmol) was treated with 2 M guanidinium chloride for 1 hour at 60°C and subsequently injected in the nanoACQUITY ultra-performance liquid chromatography system for the digestion, that was performed for 2.5 minutes at 20°C online with a pepsin column (Poroszyme® Immobilized Pepsin Cartridge). The peptides generated were trapped, concentrated and desalted using a pre-column (VanGuard BEH 1.7 µm, 2.1x5 mm) and separated using a AQUITY UPLC BEH C18 reverse phase column, 1.7 µm, 1.0x100mm (Waters) with a linear gradient from 15 to 45% of acetonitrile/water, 0.1% formic acid over 6.8 min at 40 µl/min. The mass spectra were acquired in a resolution mode (m/z 100-2000) on a Waters SynaptG2 mass spectrometer equipped with a standard ESI source. Mass accuracy was ensured by continuously infusing a GFP solution (600 fmol/µL in 50% acetonitrile, 0.1% formic acid) through the reference probe of the ESI source. The identity of each peptide was confirmed by MS^E analyses. MS^E was directly performed by a succession of low (6 V) and high collision (25 V) energies in the transfer region of the mass spectrometer. All fragmentations were performed using argon as collision gas. Data were processed using Protein Lynx Global Server 3.0 (Waters) and each fragmentation spectrum was manually inspected to confirm the assignment. The DynamX 3.0 software (Waters) was used to select the peptides considered. Only the peptic peptides present in at least five repeated digestions of the fHbp were considered for the analysis.

The antibody/antigen complexes were formed by mixing 54 pmol of the selected antibody to an equimolar amount of recombinant fHbp var.1. The complexes were incubated for 30 minutes at RT and the labelling was initiated by dilution with deuterated PBS buffer (pD 7.4) .The time course experiment (ranging from 30 seconds to 30 minutes) was performed on ice to limit the back-exchange. At each time point 30 µl of the mixed antibody/antigen were quenched with 30 µl of ice-cold quenching buffer (200 mM sodium phosphate buffer, 4 M guanidinium chloride) to dissociate the complex and to lower the pH to 2.5. The quenched aliquots were immediately frozen in liquid nitrogen and stored in dry ice at -80°C (Figure 2.8). The minimum excess of deuterium among all the experiments was 77%.

A control experiment for each antibody/antigen complex was performed with the antigen alone at the same condition previously described (using PBS instead of the antibody).

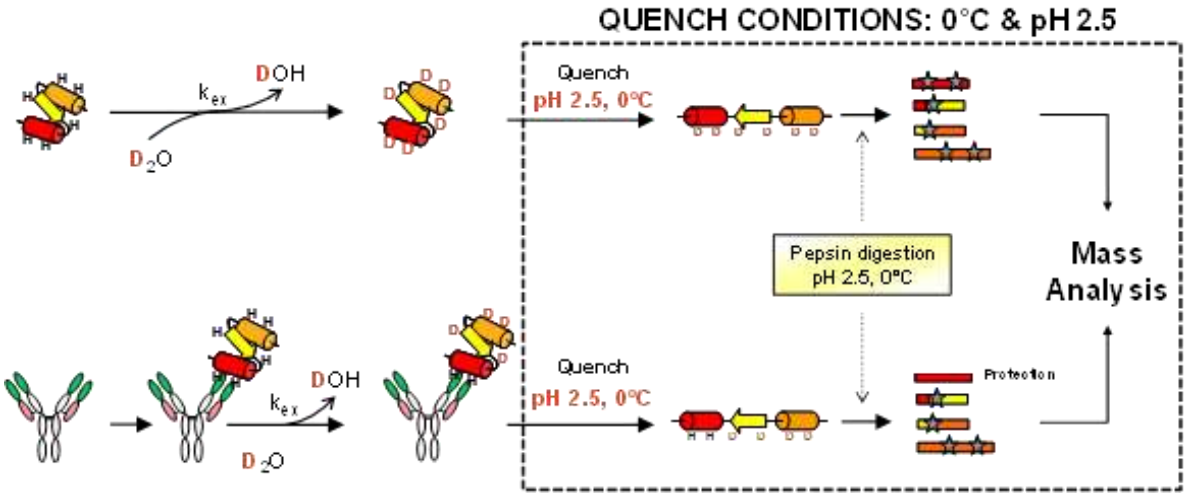

Figure 2.8: Protocol for epitope mapping with the optimized HDX-MS system.

Labeled samples were thawed rapidly to 0°C and injected into a Waters nanoACQUITY UPLC with HDX Technology. The injector, switching valve, columns, solvents and all associated tubings were at 0°C to limit back-exchange. The DynamX 3.0 software (Waters) was used to select peptides considered for the analysis and to extract the centroid mass of each of them, and for each charge state, as a function of the labelling time.

2.3.10 fHbp-antibodies: Electron Microscopy (EM)

The complexes were analyzed by transmission electron microscopy using negative staining technique to verify the integrity of the sample and the formation of the complex. The images of the complexes were than processed to generate 3D structures with the aim to assess both the overall complex folding and the internal angular flexibility. Each sample was purified through a SEC (see complex formation and purification). The fraction of the chromatographic peak corresponding to an apparent molecular weight of the immune complex was diluted to 0.03 mg/ml in 20 mM Tris, 300 mM NaCl, pH 8 buffer. 2.5 µl was loaded for 30 seconds onto a copper commercial 300-square mesh grid of carbon/ formvar (Agar Scientific) previously rendered hydrophilic with 15 mA current for 20 second by glow discharge Quorum Q150AS.

Blotted off the excess of the solution by Whatman® filter Paper No.1 (SIGMA-Aldrich), the grid was negatively stained using 1% of Uranyl Acetate in water solution for 45 seconds. The excess of the stain was soaked off by Whatman® filter paper No.1. The images of the

immune murine complex were collected on a Tecnai G2 Spirit TEM working at 120 kV with a side mount Olympus Morada 2Kx4K CCD camera and a pixel size of 3.8 Å/ pixel. The micrographs of the human cooperative couples were acquired using a Philips CM200-FEG TEM operating at 200 KV and equipped with a TVIPS TemScan-F224HD, corresponding to a pixel size of 3.3 Å/pixel on the specimen. To perform the image processing of the human complexes, a dataset of around 2000 untilted images and a Random Conical Tilt pairs of images were collected for each sample. The RCT micrographs acquired at -55° and 0° were used to obtain an initial model free of distortions produced by the preferred orientation of the complex onto the grid. This model was then refined with the particles extracted by the untilted images.

2.3.11 fHbp-human antibodies: image analysis and structure generation

All the images collected of the human mAbs complexes were processed using Scipion Sofware (Biocomputing Unit, Madrid), httpp://scipion.cnb.csic.es/m/home/. An initial analysis of the 2D class averages was performed to compare the structural differences of the immune complexes. The pairs collected were used to generate an initial volume with RCT protocol whereas the untilted datasets were used for the 2D comparison of the structural features among the complexes and for the final 3D refinement and reconstruction.

2.3.11.1 Random Conical Tilt (RCT)

A starting 3D model was generated using micrographs collected at -55° and 0°. Imported the pairs of micrographs within Scipion-RCT package, the particles were picked out independently from the tilted and untilted dataset. The protocol of assignment (Vilas et al., manuscript in preparation) tilt-pairs assigned the correct angular correlation between pairs. For each complex analyzed, a subset of around 1000 pairs was obtained. A 2D classification was performed using CL2D (Sorzano et al., 2010) and the RCT volumes calculated for each class averages. Figure 2.9 reports the protocol followed.

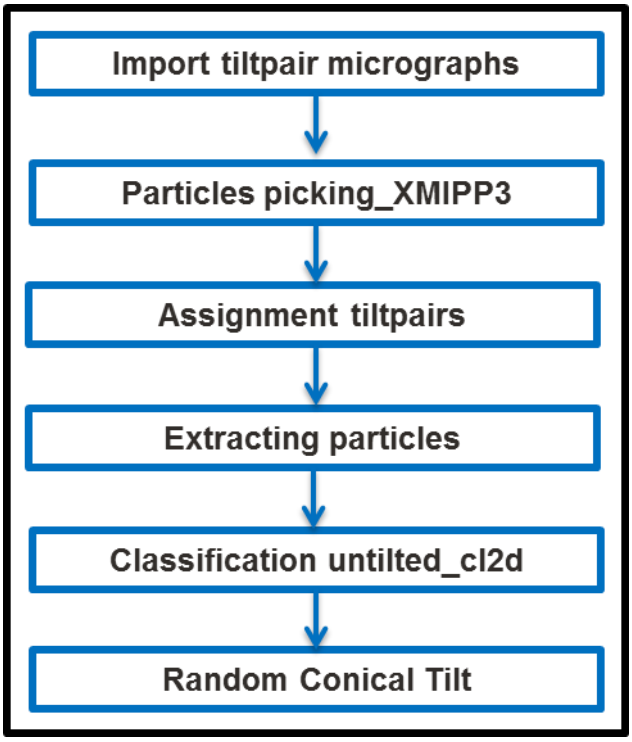

Figure 2.9: Scheme of the Scipion-RCT protocol for the generation of the initial model.

2.3.11.2 3D refinement and reconstruction

The Single Particle Reconstruction was applied to the untilted images. Created a subset containing the best images of each sample, a big number of particles were picked out and extracted using Scipion-EMAN. The goodness of the particles was screened using z-score, an error value that taking in account several features (such as the radially weighted average intensity) is able to distinguish particle images from non-particles ones (Vargas et al., 2013). Thus, a subgroup with the 10000 best particles was formed to go through iterative 2D reference-free image analysis. This classification step leaded to group particles with the same orientation and view in order to generate a final image named class with higher SNR As consequence this allowed to compare all the difference classes and evaluate the heterogeneity of the sample in terms of structure flexibility and geometrical relationship between antigen and antibodies. A high number of 300 classes were generated with CL2D to assess the diversity of the views. Imported the initial model generated using RCT, the particles were used for 3D refinement within Scipion-XMIPP3 projection matching.

2.3.12 OMV-antibodies-C1q: immunogold for C1q binding

The cooperative couple of mAb formed by the mAb7B10-mAb2C1 was tested for the capability to recruit the C1q and thus, activate presumably the complement cascade with TEM immunogold technique. The antibodies/antigen complex was analyzed directly on the surface of the OMVs expressing fHbp var.1. The entire protocol was performed at RT. The OMVs concentrated 0.03 mg/ml were incubated for 1 hour with 0.02 mg/ml of both the mAb7B10 and mAb2C1 to form the immune complex. 4 µl of this mix were loaded onto a nickel commercial 300-square mesh grid of carbon/formvar (Agar Scientific) for 3 min. Soaked off the excess of the solution by Whatman® filter Paper No.1 (SIGMA-Aldrich), the grid was incubated with PBS-SBA 0.1% for 30 minutes to block the unspecific sites. The grid was blotted again and incubated for 1 hour with 1 µl of human C1q (SIGMA-Aldrich), previously diluted 200 times in DPBS from the starting concentration of 1 mg/ml. Removed the excess of buffer, a final incubation with a mix of polyclonal anti-C1qB and anti-C1qC (SIGMA-Aldrich) was performed for 30 min. An anti-human secondary mAb conjugated with 5 nm gold particle was diluted according to manufacturer's instructions (Agar Scientific) in PBS-BSA 0.1% and used to detect the complex formed by OMV-mAb7B10-mAb2C1-C1q-antiC1q (Figure 2.10). The sample was then washed 5 times for 5 minutes each in PBS 1X and negatively stained using 2% of Uranyl Acetate in water solution for 45 sec. The excess of the stain was soaked off and the grid left to dry air for 5 minutes. Control experiments using only the secondary labelled mAb and in the absence of each component separately were performed using the same protocol. The images were acquired using a TECNAI-G2 Spirit TEM operating at 120 KV and equipped with a TVIPS Olympus Morada 2Kx4K CCD Camera, corresponding to a pixel size of 3.8 Å/pixel on the specimen.

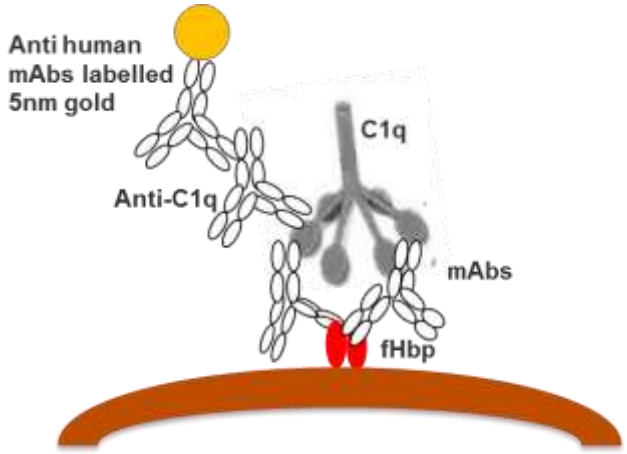

Figure 2.10: schematic representation of the OMV-mAbs-C1Q complex. On the OMV surface (colored in brown, bottom part) is expressed the fHbp var. 1 (red colored). The protein is recognized by the 2 cooperative mAbs that will bind the heads of the C1q molecule (grey dray). The C1q is detected by an anti-C1q then recognize by the anti-human gold labelled secondary mAb (mAb, bound to a yellow ball, on the top of the image).

2.4 Results

2.4.1 Generation and purification of the murine immune complex

Size exclusion chromatography was used to verify and separate the trimeric complex formed between the murine mAb502, the murine mAb30G4 and the antigen fHbp.

The chromatographic profile shows a unique peak preceded by a small shoulder, corresponding to a 400 kDa apparent molecular weight, indicating that no stable complex was formed (Figure 2.11). Based on the calibrating Standard Molecular Weight (Gel Filtration Standard, Biorad), the higher peak eluted at 1.73 ml corresponds to an apparent molecular weight of 160 kDa that is the MW of a single unbound mAbs (Figure 2.11).

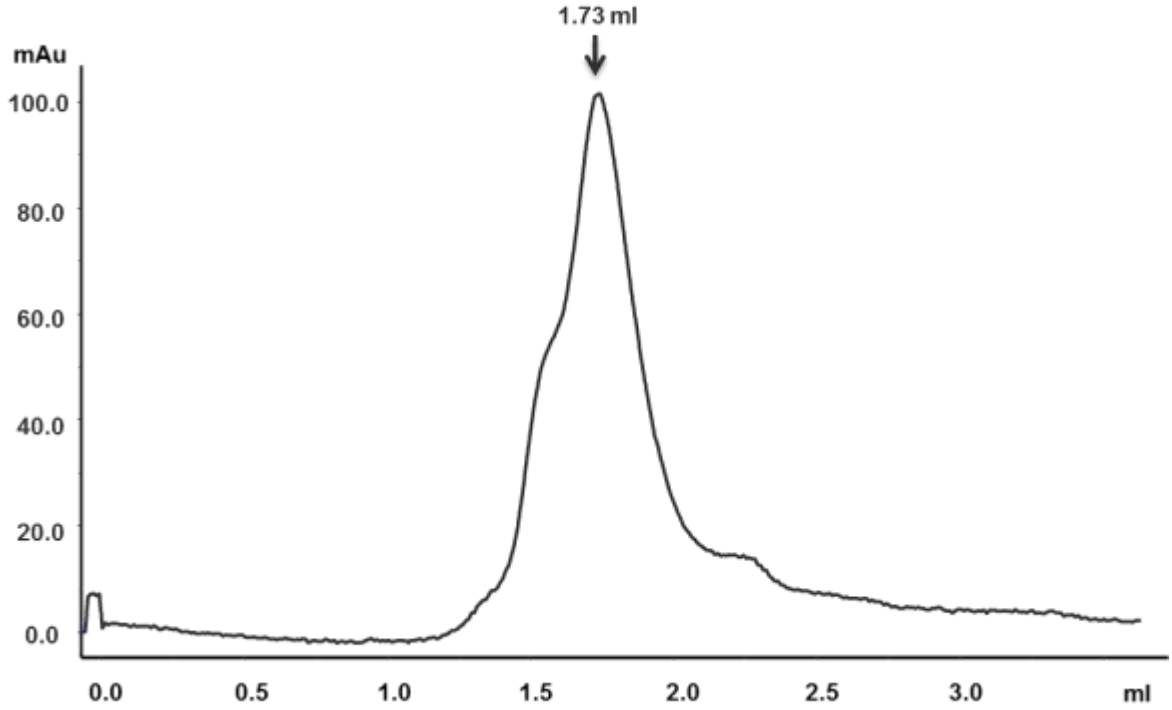

Figure 2.11: Size exclusion profile of the cooperative couples of murine mAbs and the fHbp. The unique, not symmetrical peak corresponds to an apparent molecular weight of free mAbs. The shoulder before the peak eluted around 1.55 ml could correspond to a mAbs-antigen complex.

To investigate the formation of the complex with analytical methods, an HPLC analysis was performed. To generate the internal standard, each sample was analyzed individually and recorded as brown (fHbp), green (mAb30G4) and red (mAb502) chromatographic profiles (Figure 2.12A).

A)

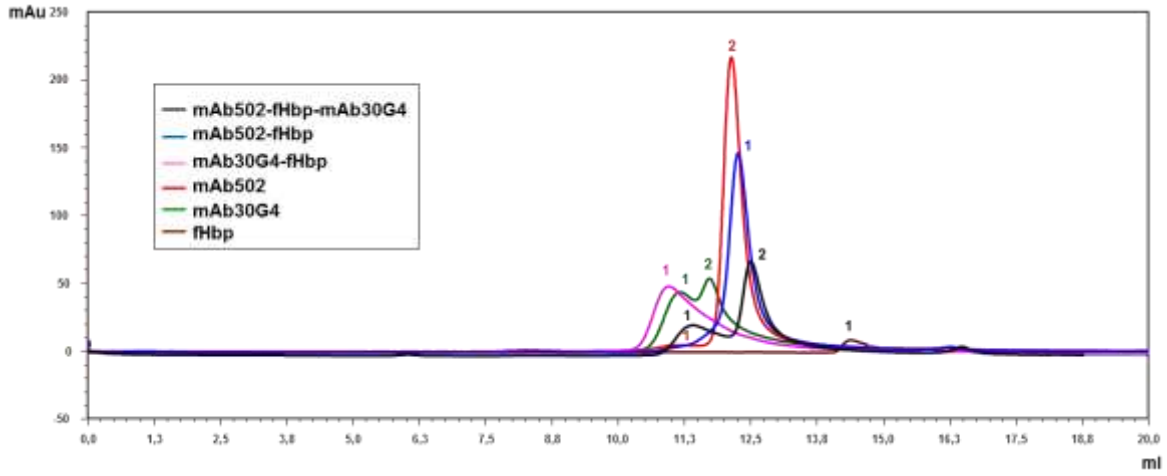

B)

Sample	Peak 1 tr	Peak 2 tr
fHbp	14,385	
mAb502-fHbp	12,235	
mAb30G4-fHbp	10,964	
mAb502-fHbp-mAb30G4	11,414	12,496
mAb30G4	11,150	11,717
mAb502	11,163	12,125

Figure 2.12: HPLC profile of the purification cooperative couples of murine mAbs formed by the mAb502 and the mAb30G4 A) Comparison between the chromatographic profiles of all the runs. The color code of the curves is described in the legend panel. B) The table reports the retention times of the chromatographic peaks.

The three components were incubated for 1 hour at RT. The purification confirms the previously obtained SEC data: no stable complex is formed. The sample corresponding to the mAb502-fHbp-mAb30G4 complex (black curve), doesn't show a sharp peak with an increased molecular weight. This result is also supported by the retention times of the elution (Figure 2.12B).

2.4.2 Generation and purification of the different human complexes

The monoclonal antibodies suitable for the formation of cooperative and non-cooperative couples were screened as described in Material and Methods. To assess the simultaneous binding between the two monoclonal antibodies and the antigen, the cooperative trimeric complexes composed by the mAb7B10-fHbp-mAb2C1 and mAb1A3-fHbp-mAb1A12 were purified by the analytical SEC. The analysis shows the presence of two different peaks for both the complexes (Figure 2.13A and Figure 2.13B): the first

corresponding to an apparent molecular weight of 402 KDa, is in agreement with a complex formed by two molecules of mAbs and two molecules of fHbp; and the second one corresponds to the non-bound mAbs, accordingly to an evaluated molecular mass of 160 kDa.

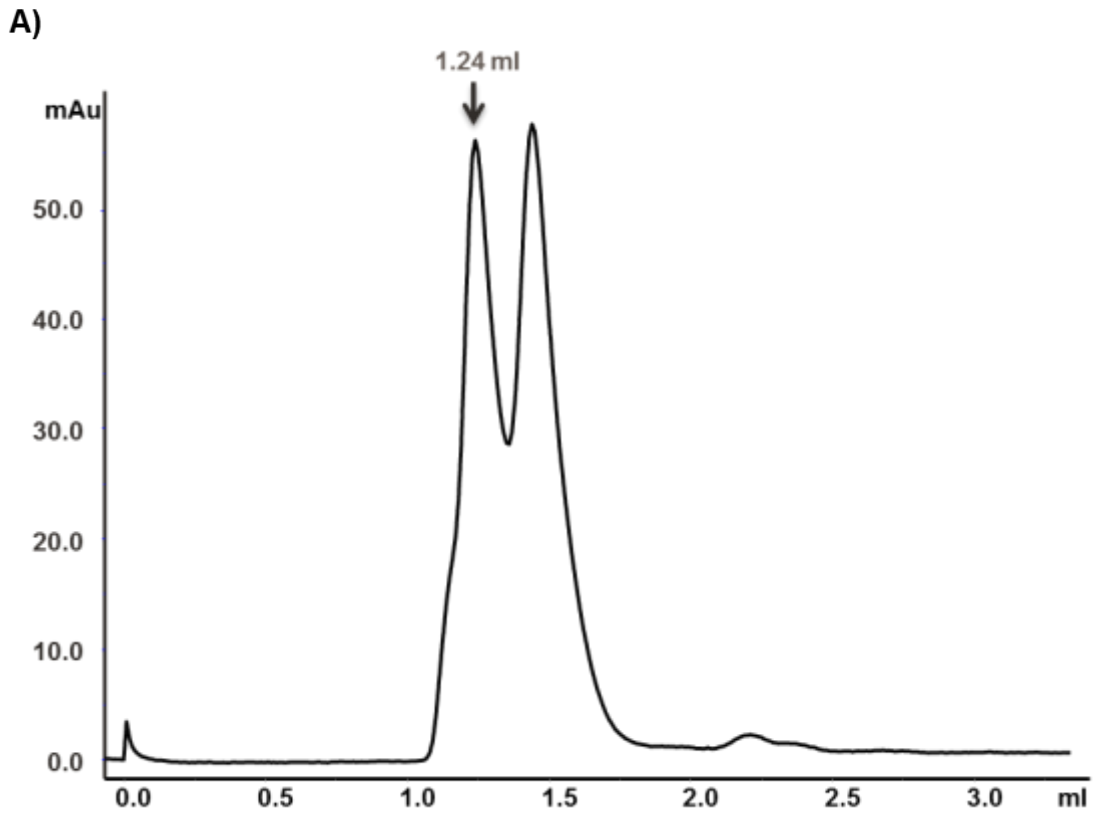

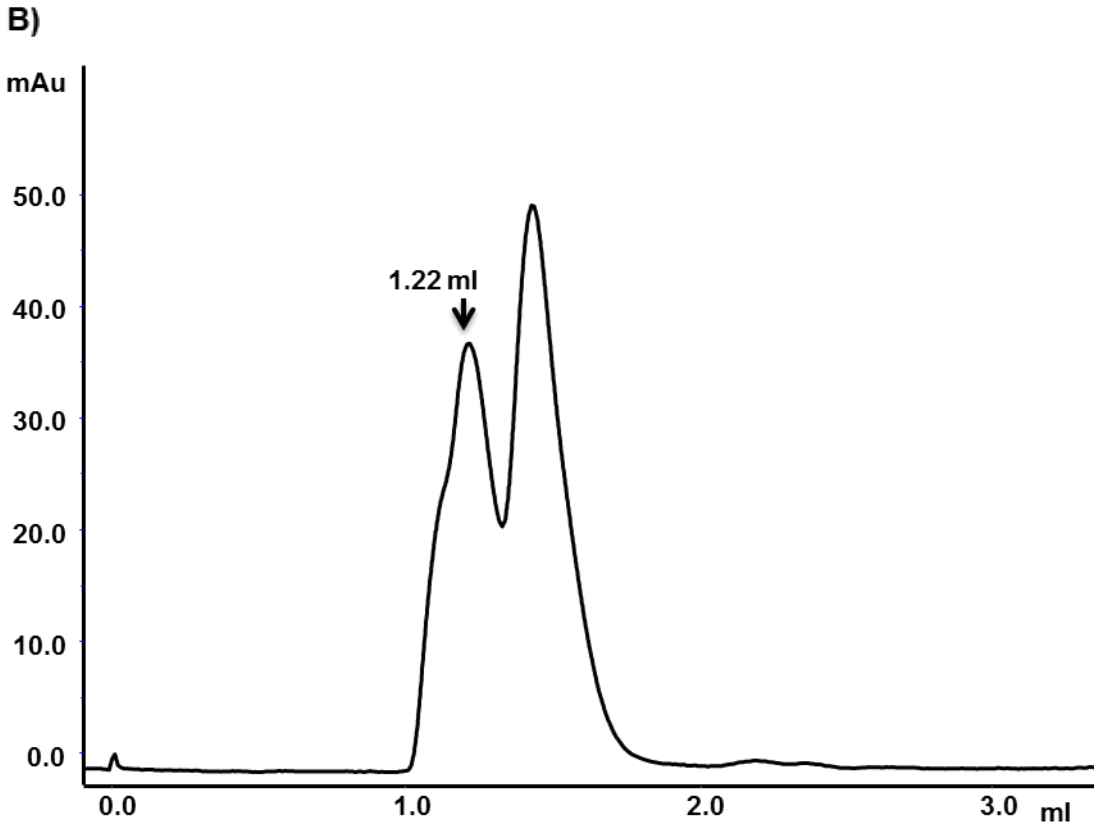

Figure 2.13: Size exclusion profile of the cooperative couples of humAbs. The first peak corresponds to an apparent molecular weight of a complex formed by two mAbs and two fHbp molecules. The second peak has the same apparent molecular weight of the non-bound mAb. A) The chromatographic profile of the couple composed of the mAb7B10-mAb2C1. B) The chromatographic profile of the cooperative couple formed by mAb1A12-mAb1A3.

The same analysis is performed on the samples of non-cooperative couples composed by mAb1A12-fHbp-mAb2C1 and mAb7B10-fHbp-mAb1G3 (Figure 2.14A and Figure 2.14B). The chromatographic profiles show one unresolved peak with a retention time corresponding to the mAb alone for both the couples. Thus, no simultaneous binding of the two antibodies to fHbp is observed for the non-cooperative couples.

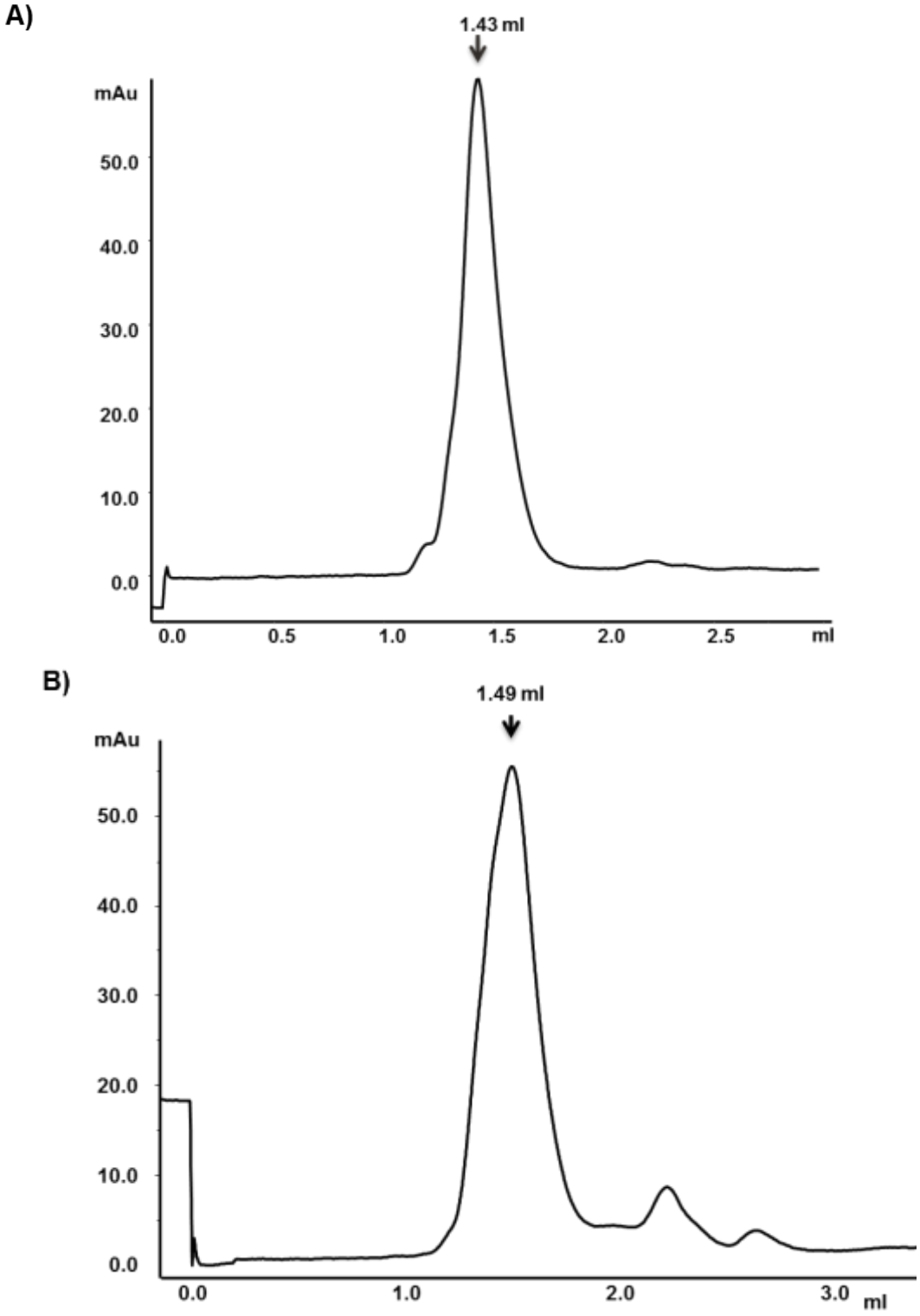

Figure 2.14: Size exclusion profile of the non-cooperative couples of mAbs. A) The chromatographic profile of the couple composed of the mAb1A12-mAb2C1. B) The chromatographic profile of the cooperative couple formed by mAb7B10-mAb1G3.

2.4.3 SPR assay for cooperative murine mAbs

The SPR technique was applied to investigate the stability of the binding of the two antibodies with the antigen. Briefly, the mAb502 was coupled by amine chemistry to a sensor-chip, followed by injection of a 100 nM solution of the antigen to capture fHbp on the chip surface. Then mAb30G4 was injected to assess its binding to the captured fHbp.
The sensorgram of the experiment with two mAbs and the antigen shows a curve that demonstrates the formation of the initial complex between the immobilized mAb502 and fHbp (Figure 2.15, red curve), followed by binding of the second mAb30G4 to the captured fHbp. This result indicates that a simultaneous binding between the two mAbs and the fHbp is possible (Figure 2.15, green curve). The slope of the last part of the sensorgram profile indicates the existence of a non-stable complex, confirming the previous results.

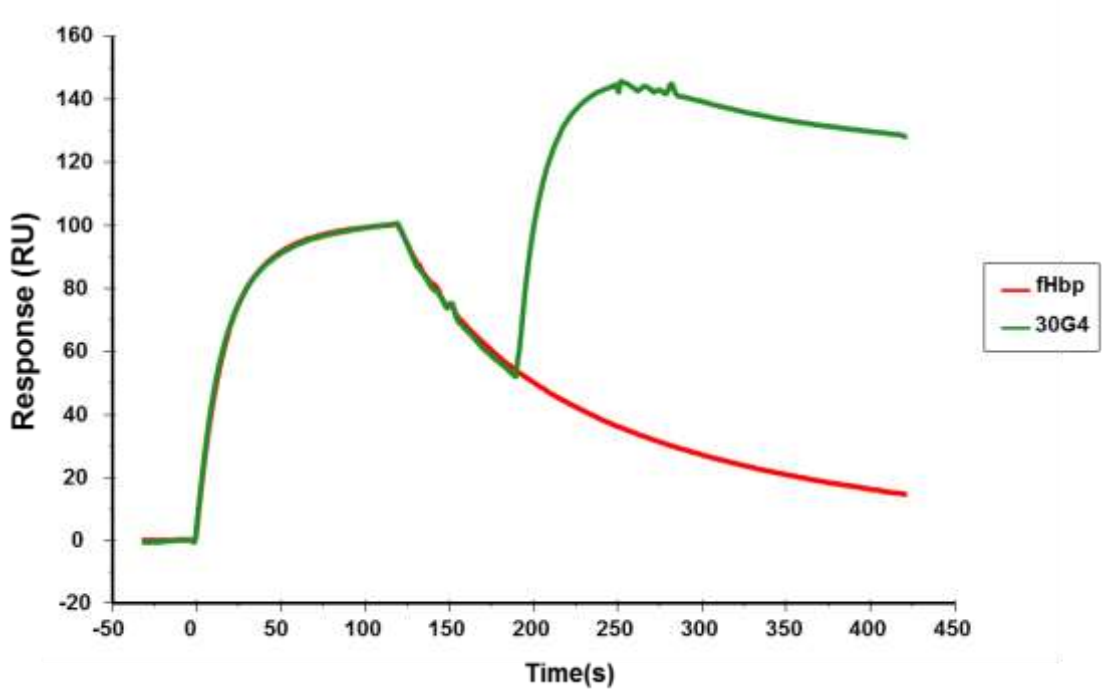

Figure 2.15: Sensorgrams profile of the SPR analysis performed using a murine couple of mAbs. The red curve reports the sensorgram profile of the control between the mAb502 and the fHbp. The green curve represents the experiment performed using both the mAb502, mAb30G4 and the fHbp antigen.

The slope in both the control and the sensorgram of the experiment demonstrates the low stability of the complex between the mAb502 and the fHbp.

2.4.4 Competitive SPR assay for cooperative and non-cooperative couples of human mAbs

The SPR approach was also applied to discriminate cooperative from non-cooperative mAb couples. The amine coupling method was used to immobilize firstly one mAb on the chip surface, followed by the capturing of the antigen. The first curve presents in all the sensorgrams shows a very stable complex, indicating strong binding between each of the tested mAb and fHbp. The following injection of the second mAb generates an additional signal only if the two monoclonal antibodies could bind simultaneously the protein. The Figure 2.16A reports a summary table of the SPR results. The single sensorgrams (Figure 2.16B, C, D, E, F) indicate that the mAb1A3 chemically coupled on the surface of the chip can bind the fHbp simultaneously with mAb1A12 or mAb2C1; the mAb1A12 with the mAb1A3, mAb7B10, mAb1G3; the mAb7B10 with the mAb1A12 and the mAb2C1; the mAb2C1 with the mAb1A3, the mAb7B10 and the mAb1G3 while the mAb1G3 with the mAb1A12, mab2C1. The form of the signal generated by the second mAb demonstrates the formation of a very stable complex. If no binding is detected for the couple, this indicates that the epitope of the second mAb is not available for binding when the protein is captured by the surface-coupled mAb. Consequently the SPR results confirm the definition of cooperative couples indicating the formation of a very stable complex between the pairs of mAbs bound simultaneously to the fHbp. Whereas non-cooperative couples were found to be unable to bind the antigen simultaneously.

A)

mAb on the surface	mAb injected				
	1A3	1A12	7B10	2C1	1G3
1A3	NON COOPERATIVE	COOPERATIVE	NON COOPERATIVE	COOPERATIVE	NON COOPERATIVE
1A12	COOPERATIVE	NON COOPERATIVE	COOPERATIVE	NON COOPERATIVE	COOPERATIVE
7B10	NON COOPERATIVE	COOPERATIVE	NON COOPERATIVE	COOPERATIVE	NON COOPERATIVE
2C1	COOPERATIVE	NON COOPERATIVE	COOPERATIVE	NON COOPERATIVE	COOPERATIVE
1G3	NON COOPERATIVE	COOPERATIVE	NON COOPERATIVE	COOPERATIVE	NON COOPERATIVE

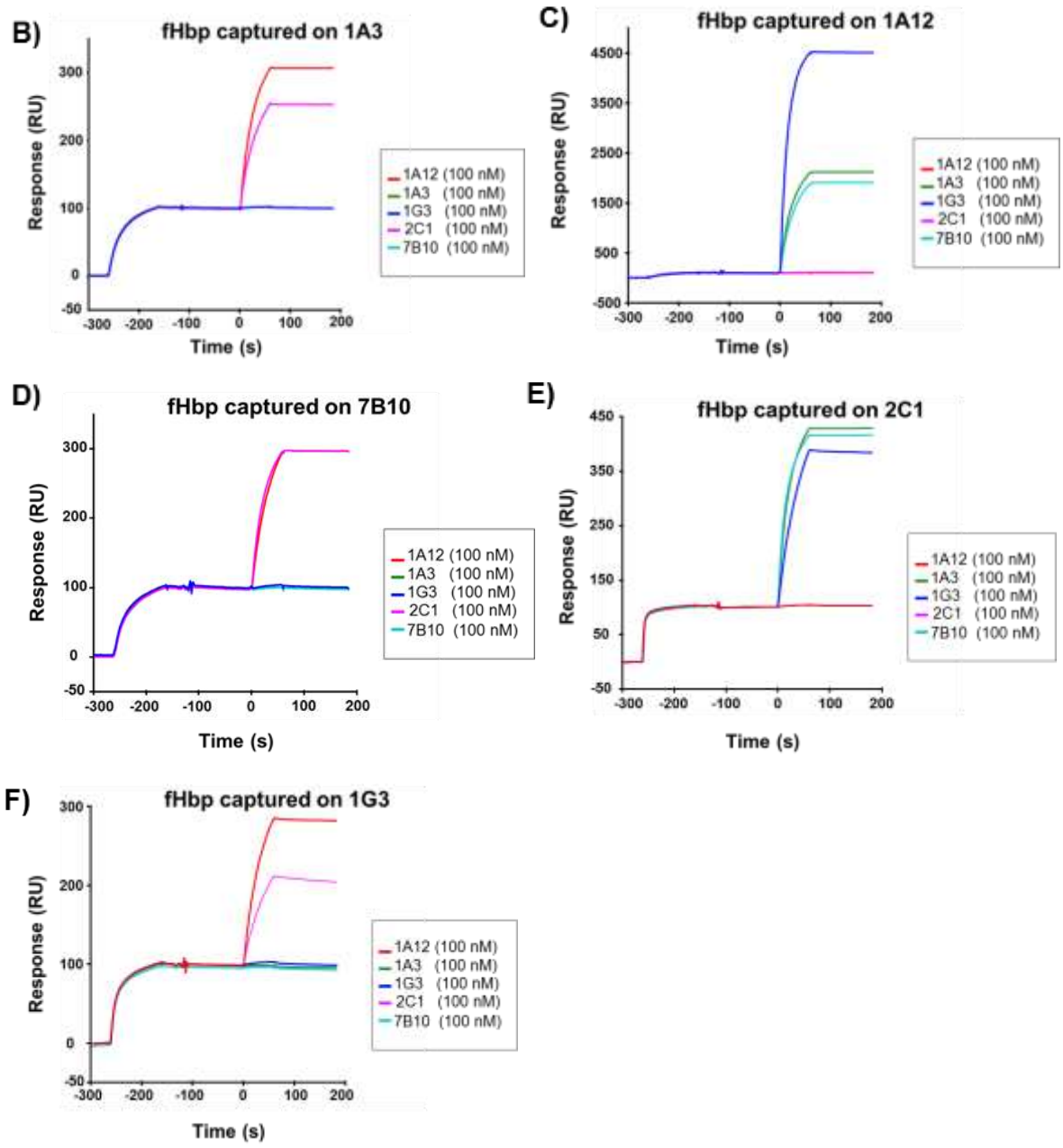

Figure 2.16: Sensorgrams profiles of the SPR competition analysis performed using each mAbs amine coupled to the sensor surface of the SPR. The color code is reported in each panel. A) Summary table indicates the cooperative (green boxes) and non-cooperative (orange boxes) couples, B) represents the coupling of the mAb1A3, C) shows the mAb1A12, D) represents the profile of the mAb7B10, E) reports the mAb1G3, F) illustrates the profile of the mAb1G3

2.4.5 Epitope mapping of anti fHbp humAbs

Pairs of non-cooperative human mAbs able to bind different variants of the recombinant fHbp (one of the pairs recognizes all the three variants of the fHbp whereas the second

mAb binds only the fHbp var.1) suggest different epitopes recognition. To investigate if the absence of simultaneous binding is caused by overlapping epitopes or by steric hindrance between mAbs, an HDX-MS epitope mapping analysis was performed. The first step consists in the generation and separation of the peptides covering the full-length fHbp in order to monitor the deuterium uptake of the peptides. The 68 peptides generated cover 100% of the protein (Figure 2.17).

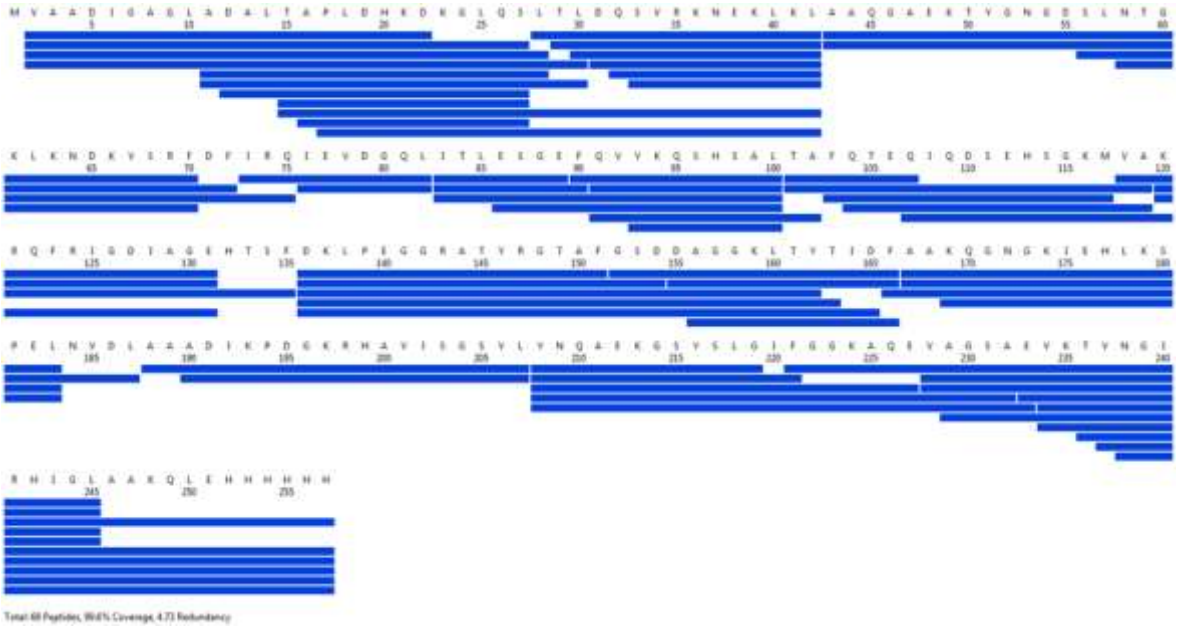

Figure 2.17: Peptidic map of recombinant fHbp var.1 obtained after pepsin digestion.

The HDX data reveal that the binding sites of the mAb7B10, mAb1A3 and mAb1G3 are exclusively located in the N terminus region of fHbp. In particular, the mAb1A3 and mAb7B10 present overlapping epitopes composed by the segment of amino acid (aa) 2-27, corresponding to the initial loop of the fHbp var.1, and the segment aa 101-119, corresponding to a β-sheet (Figure 2.18A). The epitope identifies for the mAb1G3 is composed by segment aa 2-27, that is common with the other two mAbs, and the segment aa 43-70, corresponding to a long loop (Figure 2.18B). This epitope is partially overlapping with the mAb1A3 and mAb7B10 epitopes, previously described. Collectively, the results indicate that all the epitopes are conformational and superimposable at the N terminus domain of the fHbp.

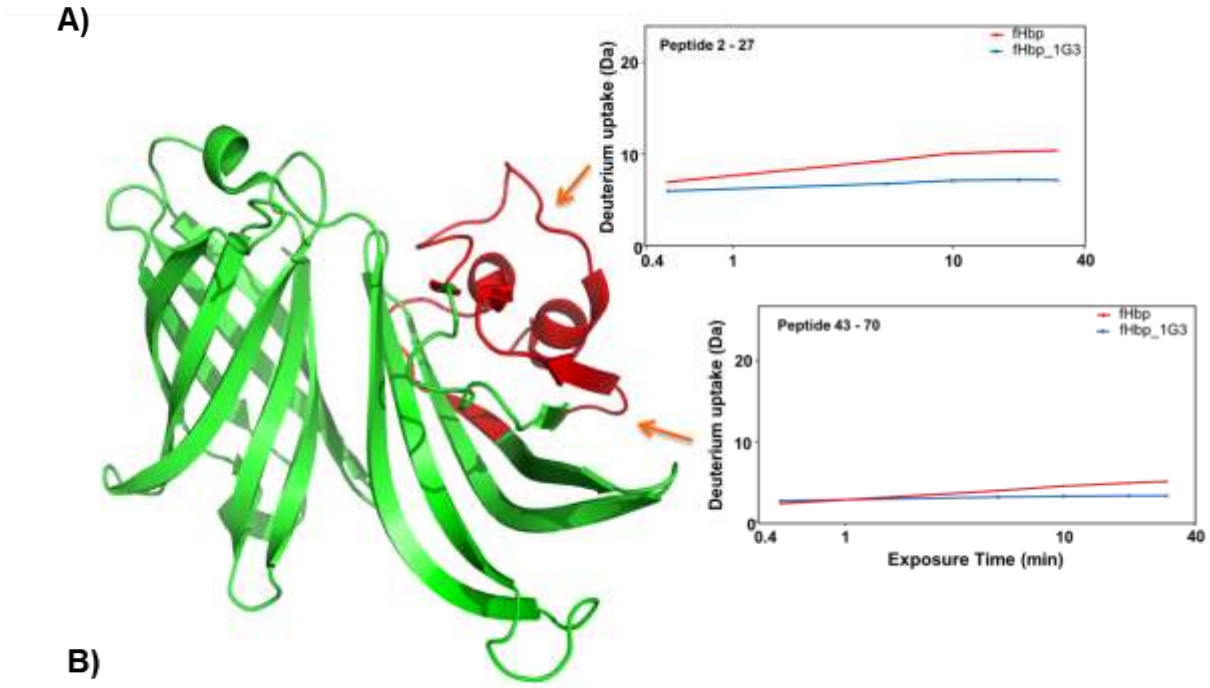
A)
Peptide 2 - 27
fHbp
fHbp_1G3
Deuterium uptake (Da)
0
10
20
0.4
1
10
40
Peptide 43 - 70
fHbp
fHbp_1G3
Deuterium uptake (Da)
0
10
20
0.4
1
10
40
Exposure Time (min)

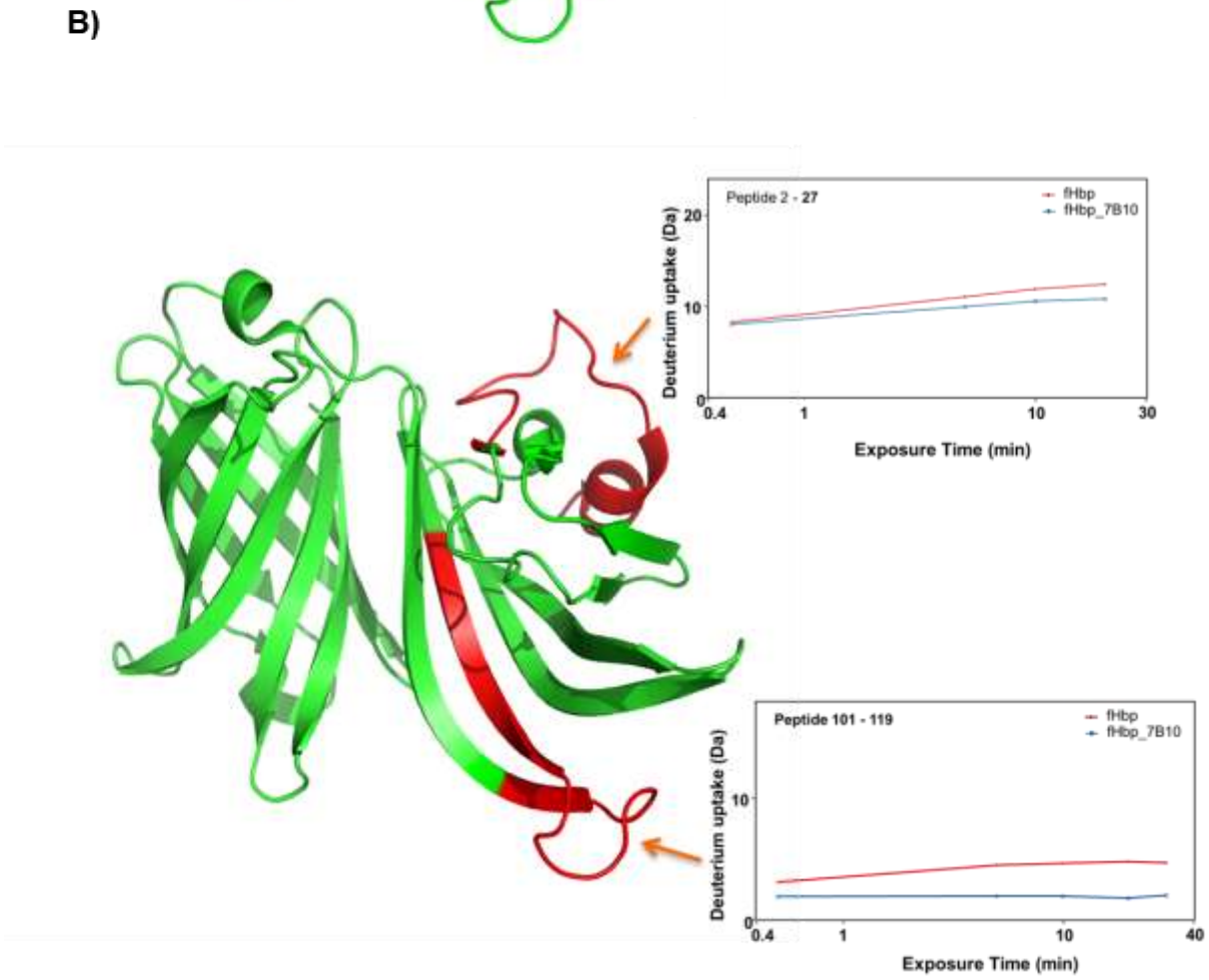
B)
Peptide 2 - 27
fHbp
fHbp_7B10
Deuterium uptake (Da)
0
10
20
0.4
1
10
30
Exposure Time (min)
Peptide 101 - 119
fHbp
fHbp_7B10
Deuterium uptake (Da)
0
10
0.4
1
10
40
Exposure Time (min)

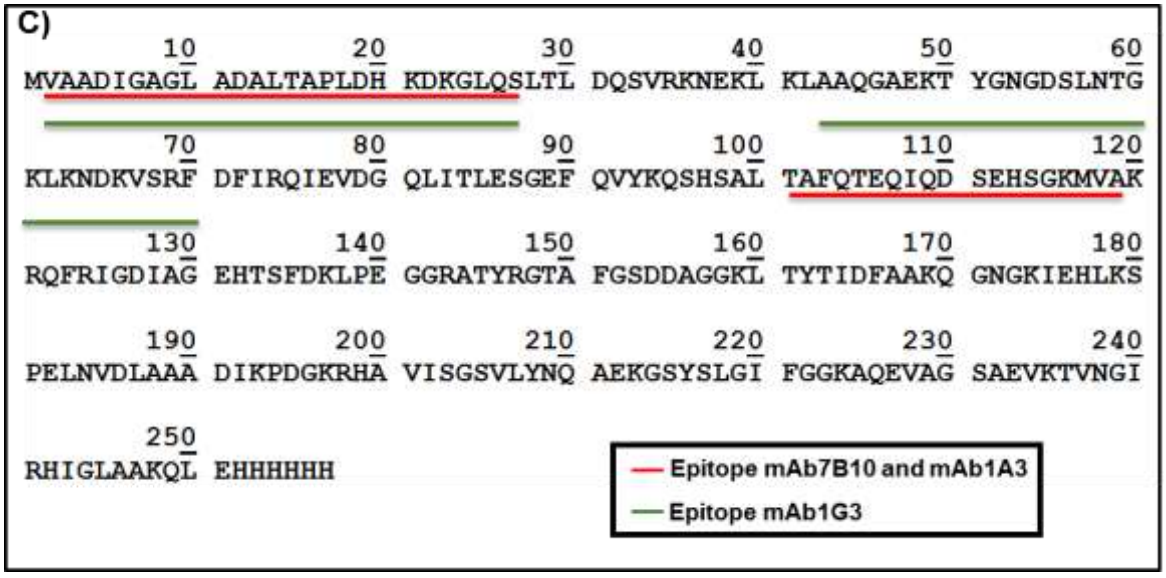

Figure 2.18: HDX_MS results showing the epitope recognized by A) the mAbs7B10 and mAb1A3 and B) the mAb1G3. The graphs report the relative uptake of deuterium in function of the time of fHbp alone (red curve) and complexed with the mAb (blue curve). The peptides present in the epitopes are highlighted in red on the fHbp var.1 structure C) Sequence of the recombinant fHbp v.1.1 showing the epitopes of the mAb1A3, mAb7B10 and mAb1G3. The color coded is explained by the legend in the box.

2.4.6 EM analysis for cooperative and non-cooperative couples

Negative Stain- TEM (NS-TEM) was used to visualize and compare the structure of the trimeric complexes using a murine cooperative couple *versus* human cooperative and non-cooperative couples. The micrographs collected for the murine complex show a heterogeneous sample with the complex present in different conformations and several copies of unbound mAbs (Figure 2.19, examples are red boxed).

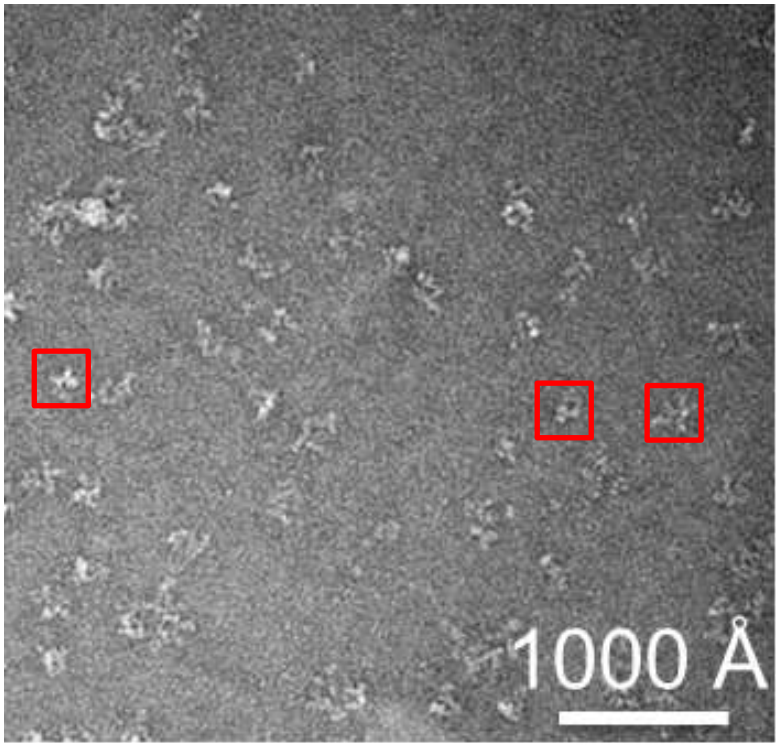

Figure 2.19: Negative staining electron micrographs of the complex formed by the cooperative couples of mAb502 and mAb30G4. Examples are red boxed.

The micrographs of both the cooperative trimeric complexes, the mAb7B10-fHbp-mAb2C1 and the mAb1A3-fHbp-mAb1A12, indicate homogeneous preparations in which the complexes assume the same constant geometrical shape, a rhomboid, suggesting the formation of a very stable trimeric complex (Figure 2.20A and Figure 2.20B, examples are showed boxed in red). The structure is composed by two monoclonal antibodies each bound to one molecule of fHbp, where the two fHbps are facing each other, and with the Fc portions of the Mabs pointing outwards the rhomboid. To further investigate on the structure of the trimeric complexes and to understand the impact of both flexibility and steric hindrance of the monoclonal antibodies on the folding of the whole complex, the cooperative mAb7B10 and mAb2C1 were generated as fabs. NS-TEM analysis is performed on the trimeric complex formed using the fab7B10 and fab2C1. The micrographs show a homogenous and preferential distribution of the complex that assumed a fixed V geometrical shape made by two fabs protruding both from the fHbp side (Figure 2.21, examples are highlighted by red boxes).

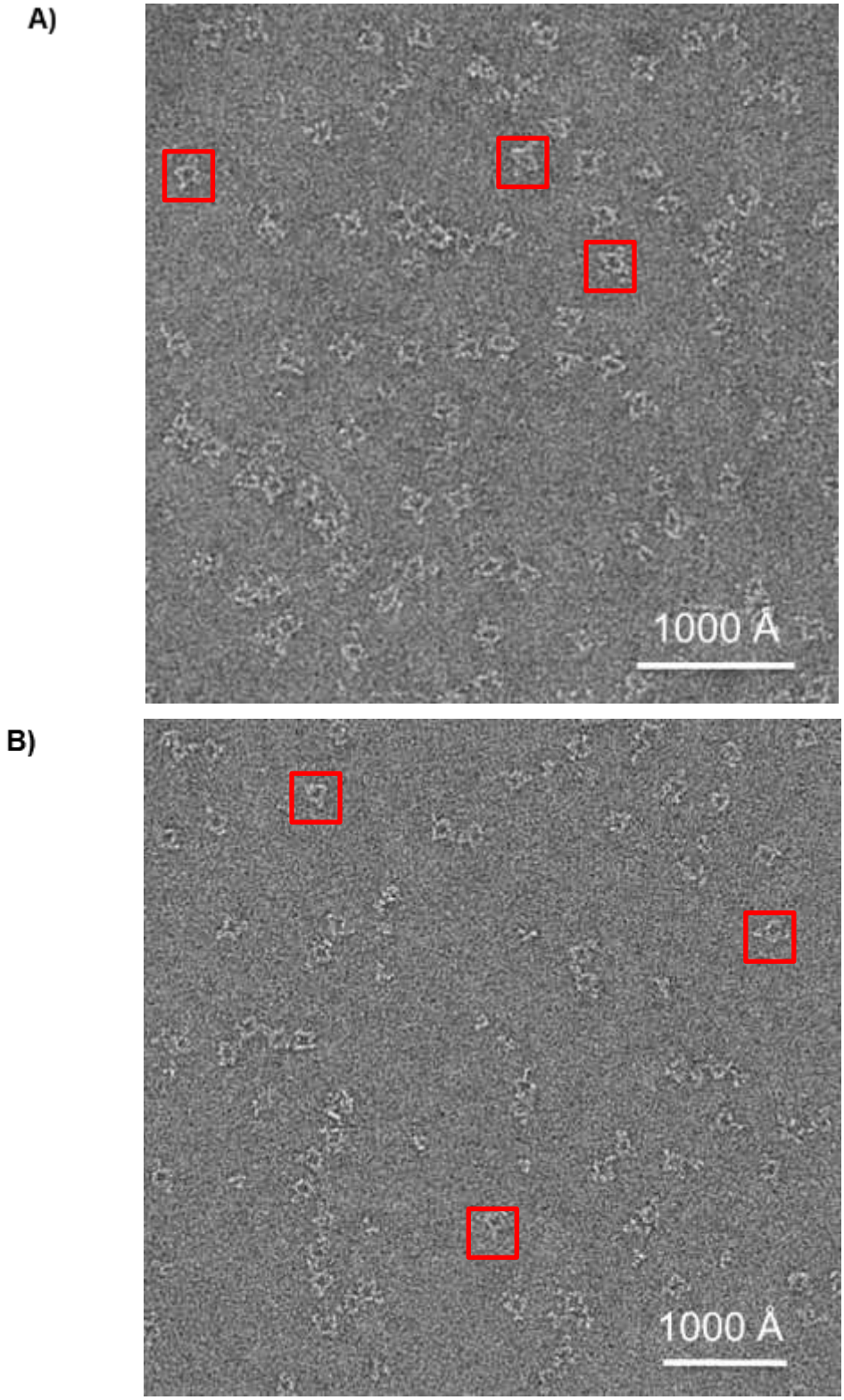

Figure 2.20: Negative staining electron micrographs of the complexes formed by the cooperative couples of mAbs A) mAb7B10-mAb2C1 B) mAb1A3-mAb1A12. Examples are red boxed.

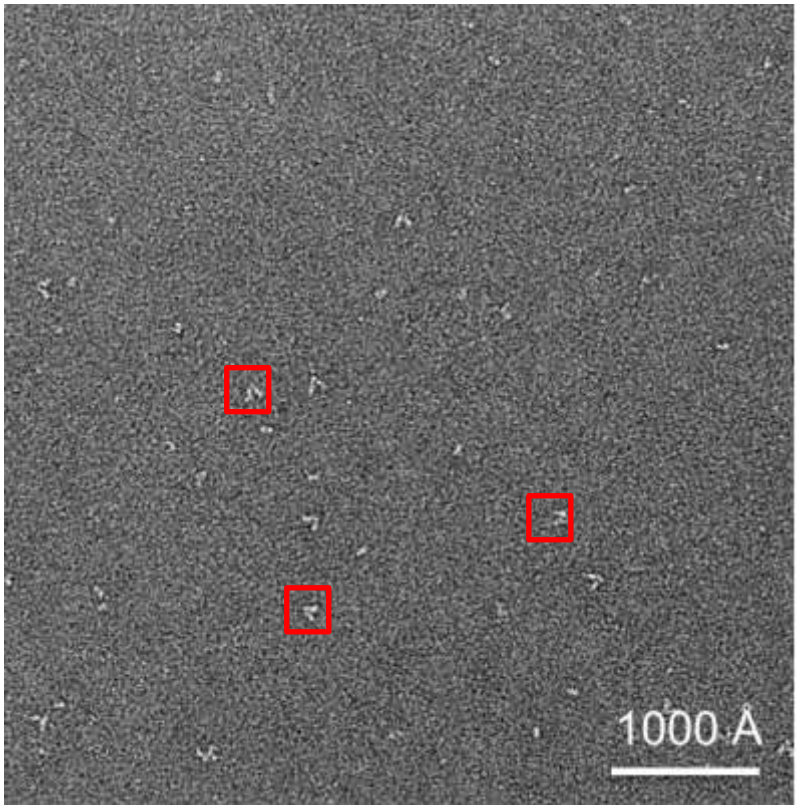

Figure 2.21: Negative staining electron micrographs of the complex formed by the cooperative couples of fabs fab7B10-fab2C1. Examples are red boxed.

NS-TEM analysis was used to image also the non-cooperative couples composed by mAb7B10-fHbp-mAb1G3 and mAb1A12-fHbp-mAb2C1. Both the samples present a heterogeneous conformation with the presence of single unbound mAbs and few formed complexes. The absence of complexes showing a constant geometrical shape indicates that no stable simultaneous binding between the mAbs and the antigen exists (Figure 2.22A and Figure 2.22B, examples are highlighted by red arrows).

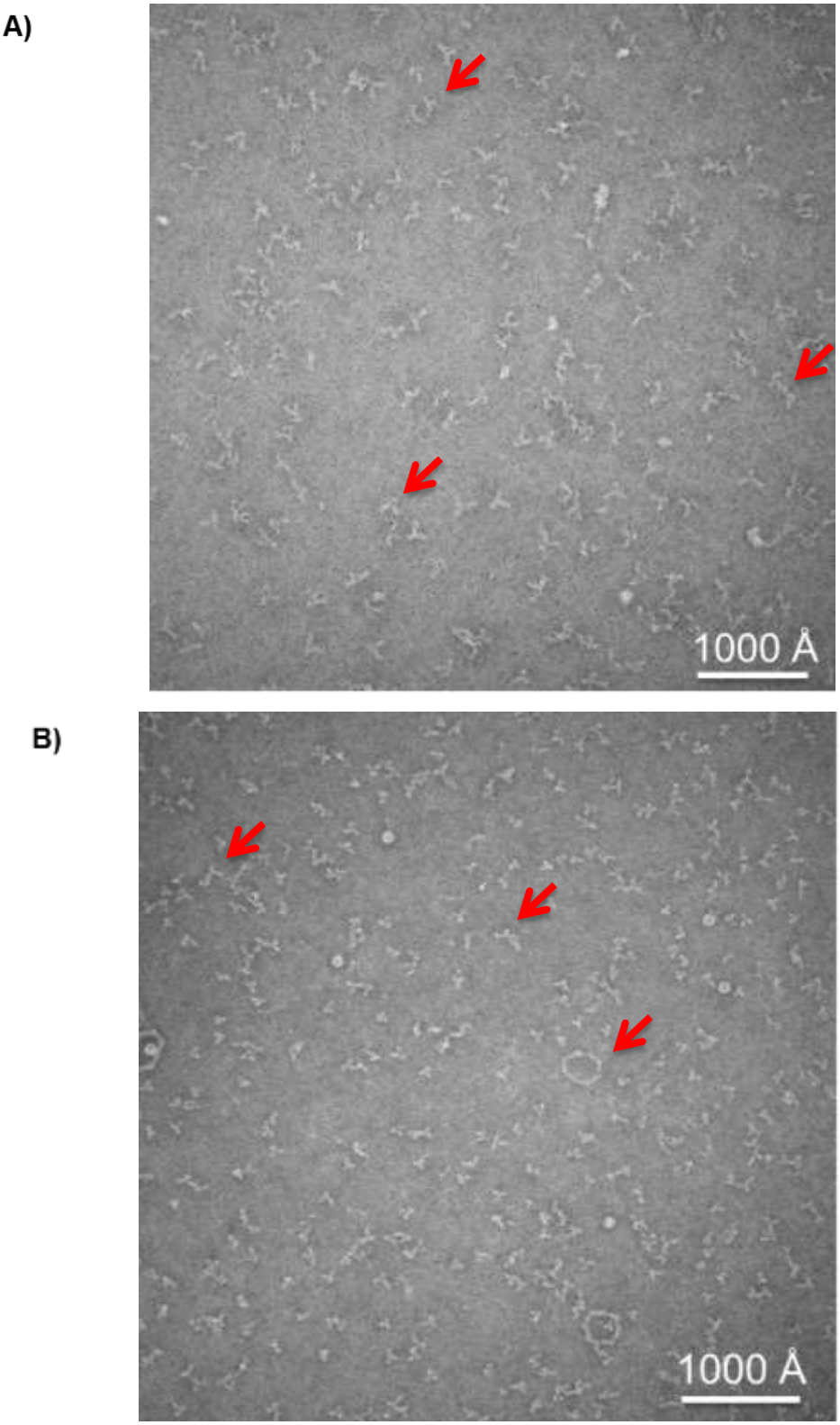

Figure 2.22: Negative staining electron micrographs of the complex formed by the non-cooperative couples of mAbs A) mAb1A12-mAb1A3 B) mAb7B10-mAb1G3. Examples are highlighted by red arrows.

2.4.7 Structure generation of cooperative couples of human mAbs and fabs

To investigate the impact of the relative orientation of mAbs with respect to the antigen and the possible influence of the flexibility and of the steric hindrance of the mAbs on the complex formation, we determined the structures of the trimeric cooperative human complexes formed by i) the mAbs and ii) by the fabs. Due to the preferred orientation of the complexes observed in the images, a Random Conical Tilt and an untilted set of micrographs were acquired in order to proceed with the single particle analysis as previously described.

2.4.7.1 2D class averages analysis

Each immune complex was processed as following: the best micrographs of the untilted dataset free of drift and astigmatism were used to start the SP reconstruction processing. A subset with the best 10000 particles of both the cooperative trimeric complexes formed by mAbs and fabs were screened using a value of 3 in the z-score parameter and then extracted. The centering, alignment, and classification of the particles were performed using Scipion-CL2D method grouping the particles in different reference-free classes based on their view and orientation (Figure 2.23). The analysis of the antigen-antibody geometrical relationship was performed comparing all the different classes in the same orientation of each sample (Figure 2.24). The reference-free 2D class averages of the two cooperative couple of mAbs confirm the formation of a dimeric complex with same overall rhomboidal shape with the fc portions pointing outward the rhomboid free to rotate due to their high flexibility, thus generating 2D classes that show a blurred intensity. On the contrary a very well defined intensity characterizes the fabs-antigen region of the complex (Figure 2.24A and 2.24B). The different epitopes location of the mAbs onto the antigen results in a different angle between the two complexes and a flip in the z direction on the fabs in the mAb1A3-mAb1A12 complex (Figure 2.25A and Figure 2.25B).

The reference classes of the complex formed by the fab7B10 and the fab2C1, (Figure 2.24C), clearly shows a constant intensity with no blurred area as they didn’t contain an Fc portion.

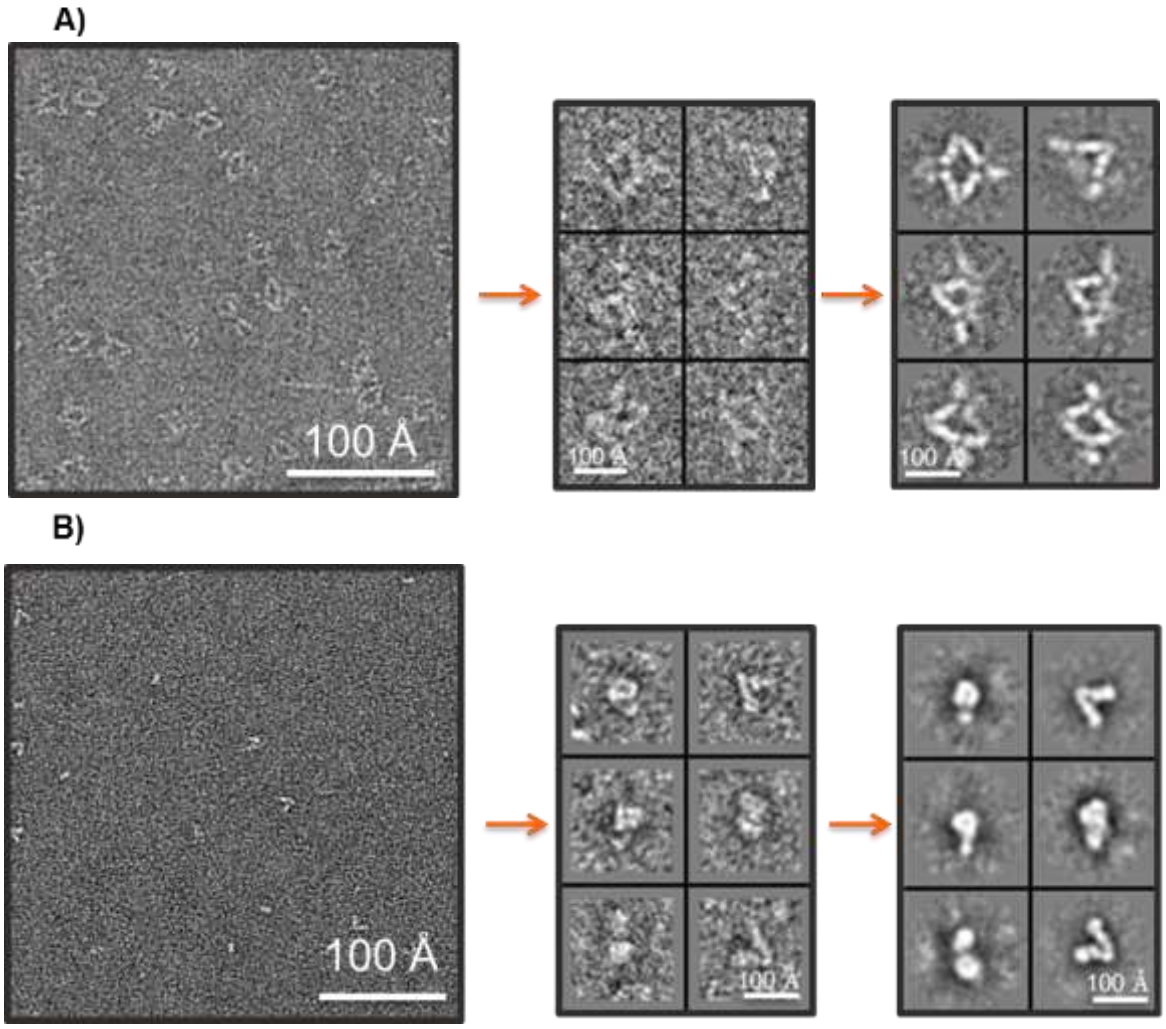

Figure 2.23: Examples of the processing of the micrographs for (A) the complex of the cooperative couple of mAbs and (B) cooperative couple of fabs: from the raw micrographs, to the extracted particles and finally reference-free classes. Scale bar is represented as white bar.

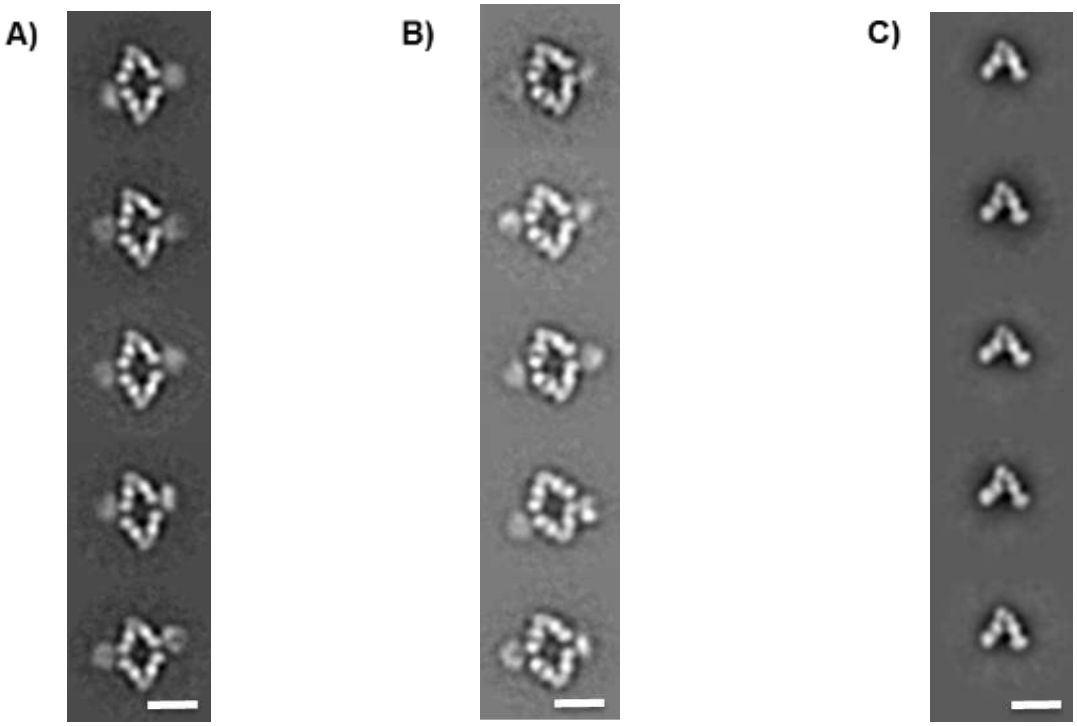

Figure 2.24: Examples of five different free reference classes in the same approximate orientation for each samples used to investigate the flexibility of each structure. (A) The complex of the cooperative trimer mAb7B10-fHbp-mAb2C1, (B) the complex of the cooperative trimer mAb1A3-fHbp-mAb1A12 and C) the cooperative trimer fab7B10-fHbp-fab2C1.The scale bar represented as white bar in the images corresponds to 10 nm.

Figure 2.25: Representative class averages of the mAbs complexes in a side view. A) The complex formed by the mAb7B10 and mAb2C1 B) The complex composed by the mAb1A3-fHbp-mAb1A12. The scale bar is represented in white and corresponds to 10 nm.

The first prerequisite to proceed with the reconstruction and the final 3D map is the presence of an adequate number of different orientations of the complex among the different classes. In the absence of several different orientations the final model may result affected by elongation or other distortions due to the missing information of that

lacking views. Since we should use all the particles for the refinement, we verified the existence of different views of the complex in order to avoid the generation of a model with a preferred orientation. All the 10000 particles of each dataset collected were tested against a number of classes (300) applying CL2D to detect the orientations. The Figure 2.26 shows the classes generated by the mAb7B10-fHbp-mAb2C1, as example. Although the preferred side orientation is predominant some lateral views are also available (Figure 2.26, red boxed).

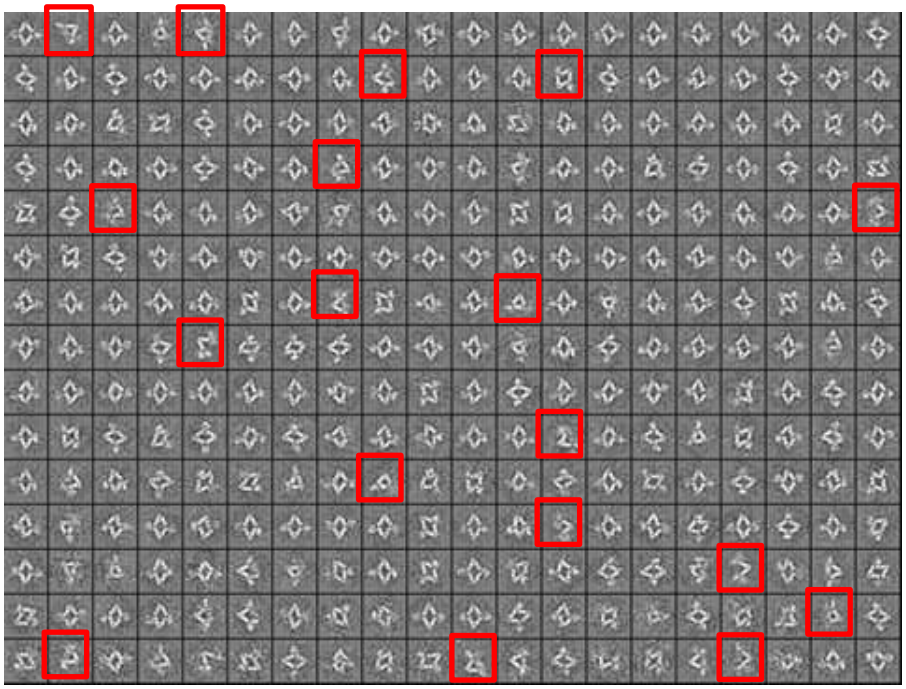

Figure 2.26: CL2D classification of the 10000 particles in 300 classes of the complex mAb7B10-mAb2C1. Most of the classes show the complex in its preferred orientation (top view) while red boxes indicate different views.

2.4.7.2 Initial model generated with RCT

To generate an initial model free of bias and to avoid any distortion produced by the preferred orientation assumed by the complex onto the grid, the collected tilt-pairs (i.e. formed by a tilted and untilted couple of micrographs) were processed using the Random Conical Tilt protocol. Briefly all the tilt-pairs of micrographs (Figure 2.27) were imported and the particles picked out with Scipion-RCT package. The angle correlation was calculated using assignment tilt-pairs protocol, and then all the pairs of particles were extracted. The class averages were generated and each class was refined with pairs of extracted particles to obtain initial models. The initial map generated by the single class reconstruction was chosen for 3D reconstruction and refinement against the untilted images.

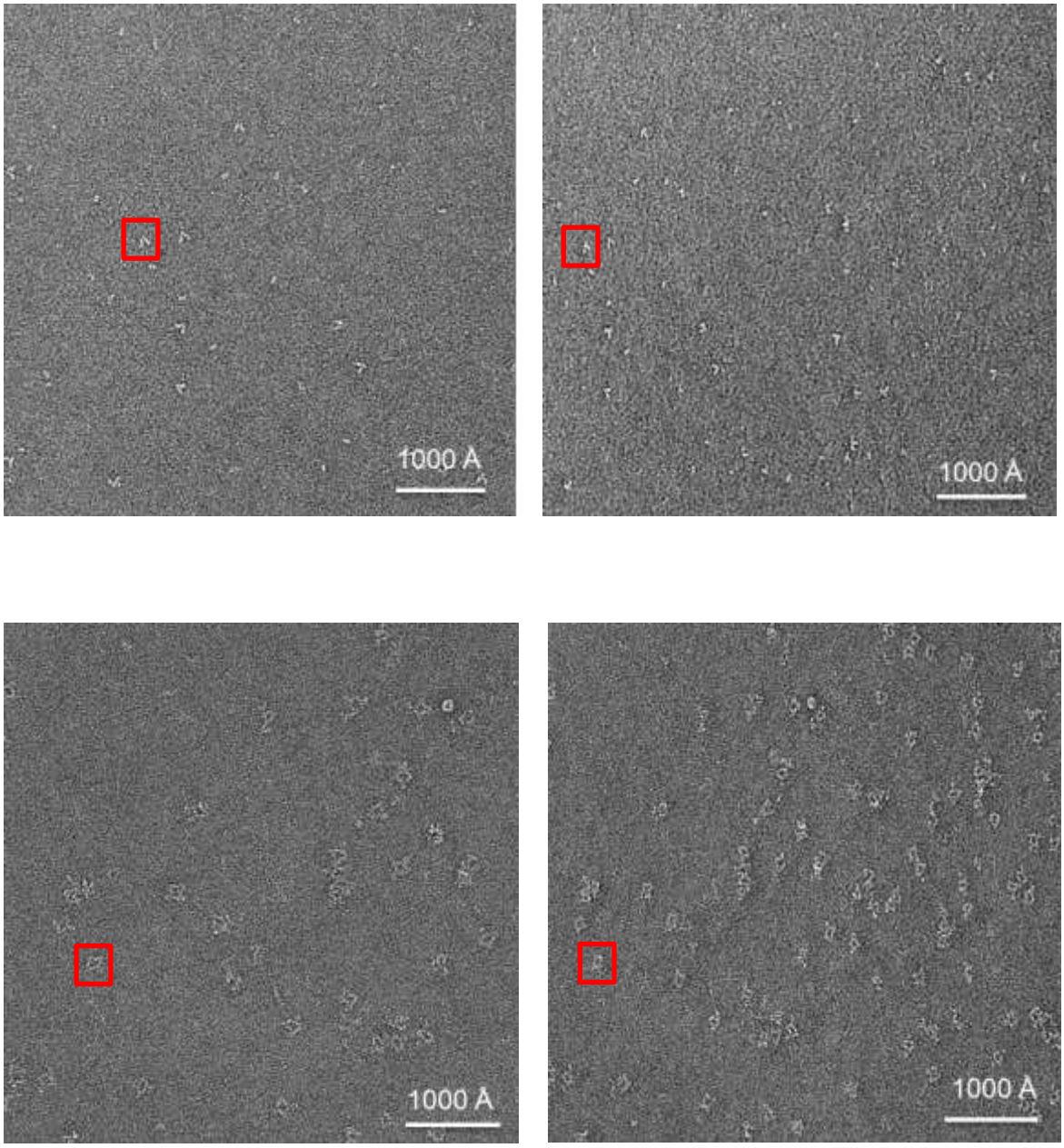
1000 Å
1000 Å
1000 Å
1000 Å

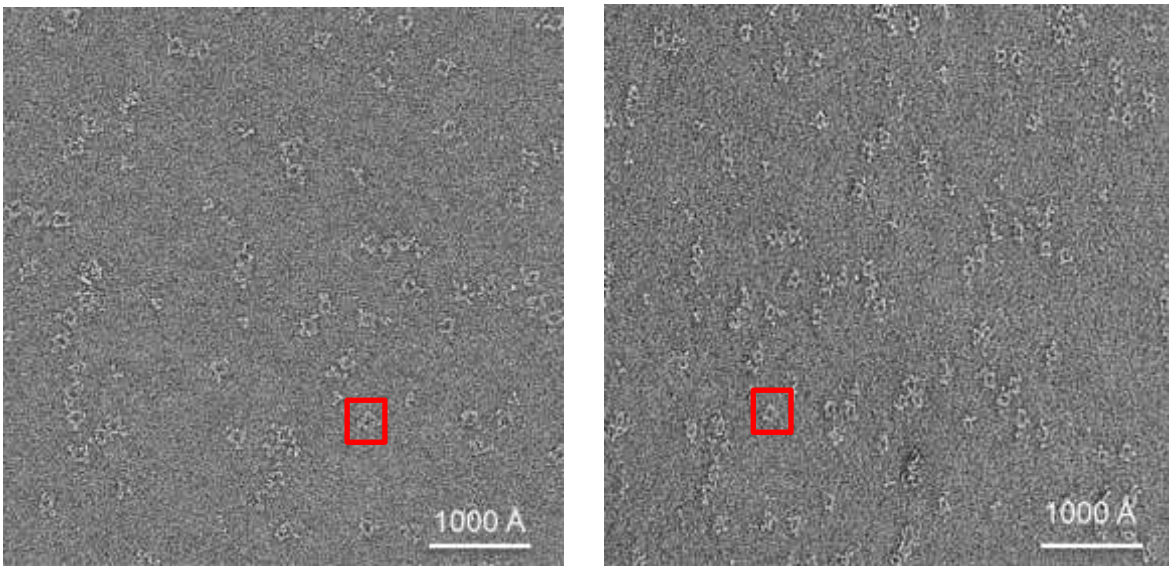

Figure 2.27: Tilt-pairs of micrographs used for the generation of the initial model with Random Conical Tilt protocol, reported here as examples. These images show the sample fab7B10-fab2C1 (top line), mAb7B10-mAb2C1 (center line) and the complex formed by the mAb1A3-mAb1A12 (bottom line). The untilted image is shown on the left; the -55° tilted image is shown on the right. The orange boxes indicate a couple of tilt-pairs: the untilted (left) and tilted (right) particles.

The best 3D structure obtained as initial model for the immune complexes formed by the mAb7B10-fHbp-mAb2C1 and mAb1A3-fHbp-mAb1A12 show a well-defined rhomboidal shape, corresponding to the fabs-antigen region of the complex, and two distinct densities on the sides, equivalent to the flexible Fc region of each mAbs (Figure 2.28A and Figure 2.28B). The connection densities between Fc portion and the rest of the mAb molecule are missing due to the thin and highly flexible hinge region of the antibody. As expected, the fab complex result in a V shape presenting only the two rigid bodies of the fabs those protrude from antigen density (Figure 2.28C).

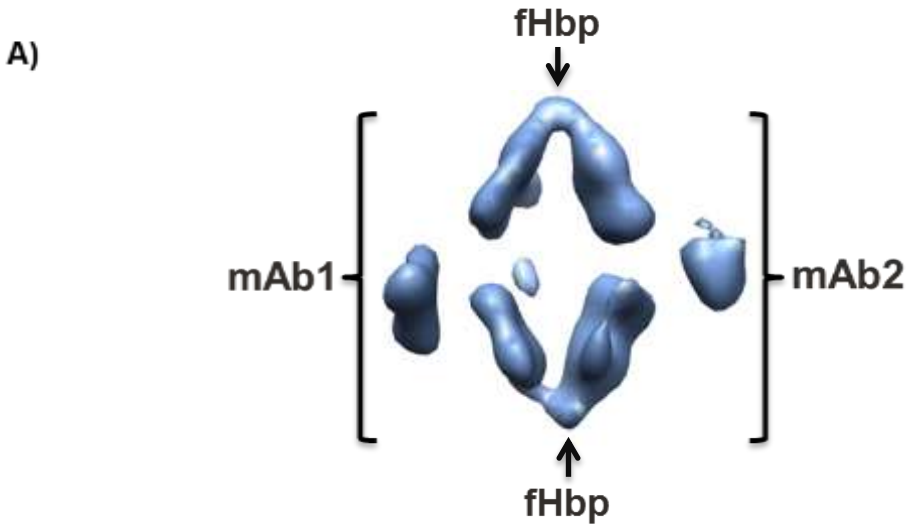

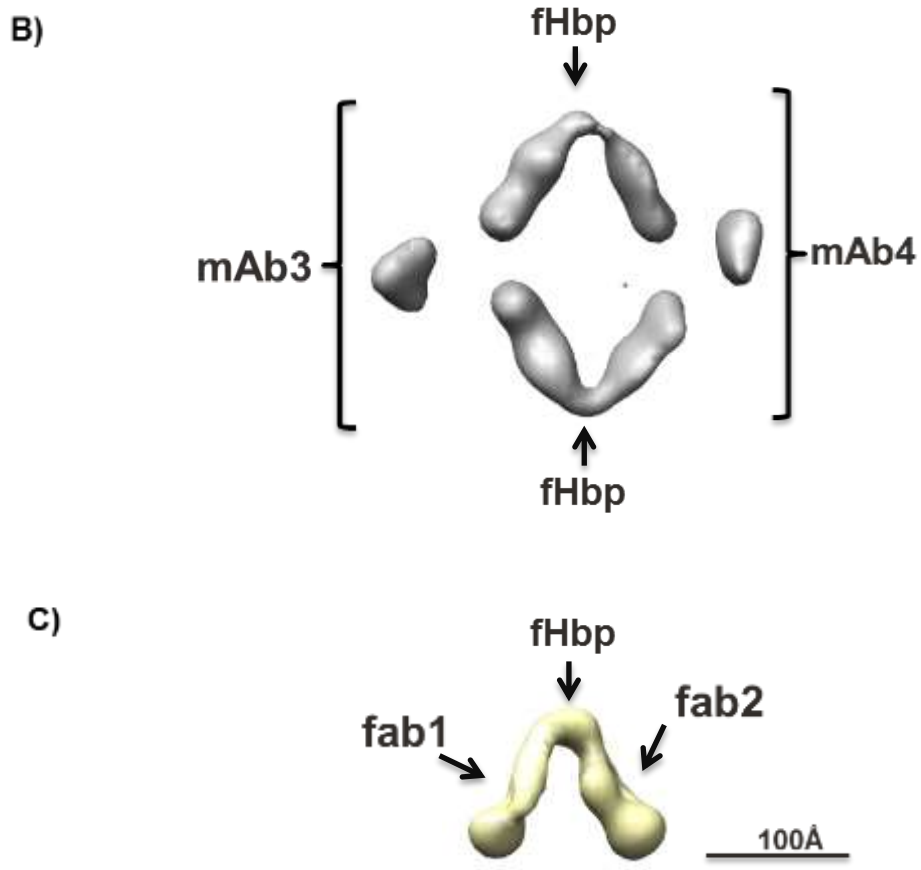

Figure 2.28: Random Conical Tilt models generated with Scipion software from the tilt-pairs micrographs collected. Each model presents the main features of the correspondent immune complex. The scale bar for all the models is reported in the right bottom part. The components of each immune complex are reported in the models. A) The complex formed by the mAb7B10-fHbp-mAb2C1 B) The complex composed by the mAb1A3-fHbp-mAb1A12 and C) the fab7B10-fHbp-fab2C1.

2.4.7.3 3D refinement and reconstruction

To investigate the influence of the mAb molecule on the structure of the immune complexes, Scipion-Xmipp projection matching was used to refine the 3D structure obtained from the previous RCT models. Each subset of 10000 particles was used to refine the initial model resulting in three maps each with a resolution of 30 Å (FSC=0.5 calculated by Scipion Xmipp projection matching approach) (Figure 2.29B, 2.30B, 2.31B). The resolution obtained was high enough to allow the determination of the geometrical relationship between the antigen and the antibodies.

A manual fitting of the available PDB X-ray coordinates in the EM maps was performed. The structure of the human Immunoglobulin subclass 1 at a resolution of 2.8 Å (PDB entry: 1IGT) and the antigen fHbp solved at a resolution of 2 Å (PDB entry: 3KVD) (Figure

2.29A, Figure 2.30A, Figure 2.31A) were used in the fitting. The crystallographic coordinates of both the antigen and the antibodies correctly fitted inside the EM volume. To test the reliability of the reconstructions the projections of the reconstructed volume (reference projection) were compared with the raw images (experimental data) (Figure 2.29B, Figure 2.30B and Figure 2.31B).

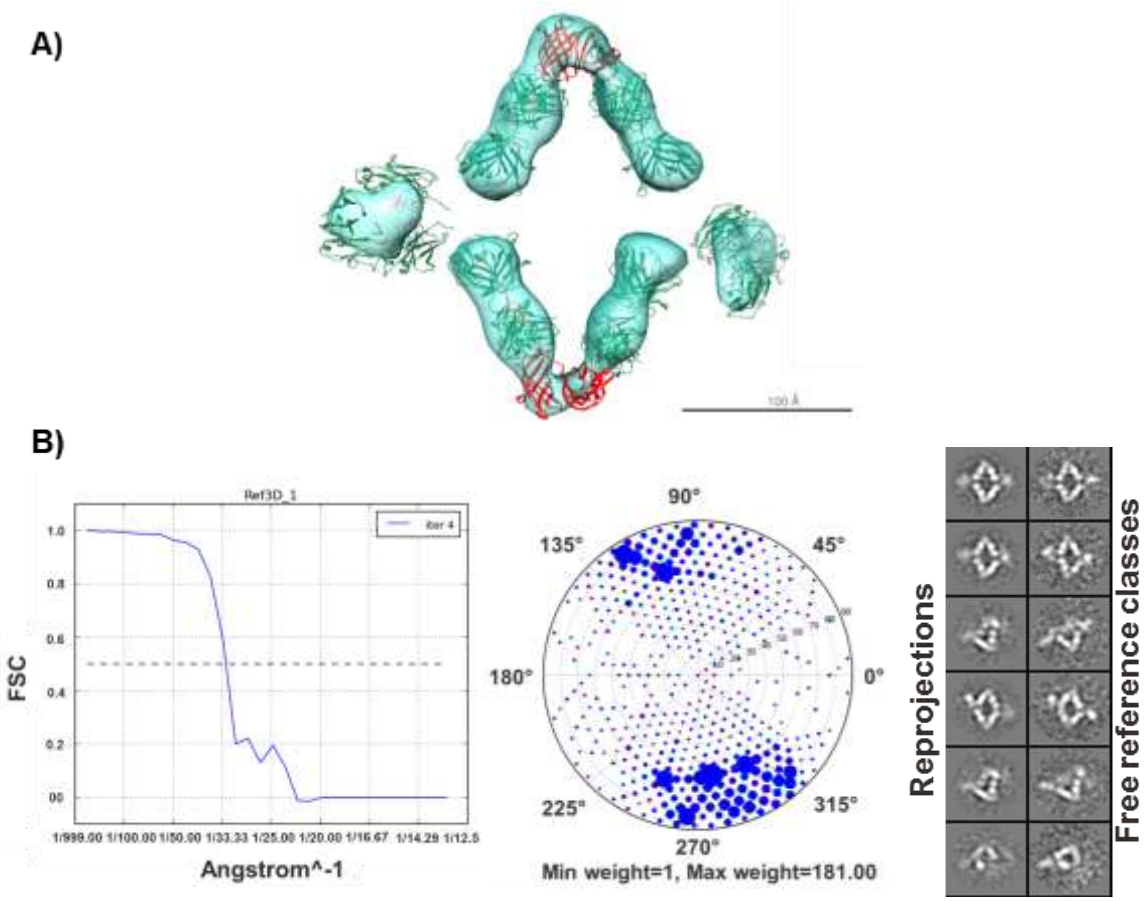

Figure 2.29: 3D reconstruction of the complex formed by the mAb7B10-mAb2C1. A) The final map of the complex at a resolution around 30 Å fitted with an immunoglobulin PDB structure (1IGT, green colored) and the structure of the fHbp (3KVD, red colored). B) FSC curve (on the left) and the angular distribution (in the center) related to the EM volume generated using the projection matching. The panel on the right shows the comparison between projections of the final volume (left) and reference-free classes (right).

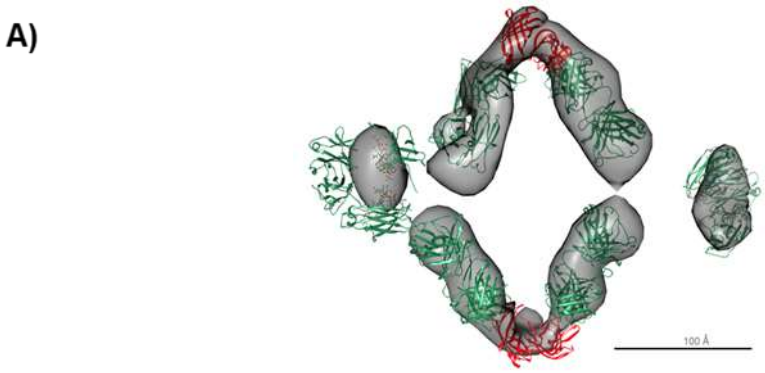

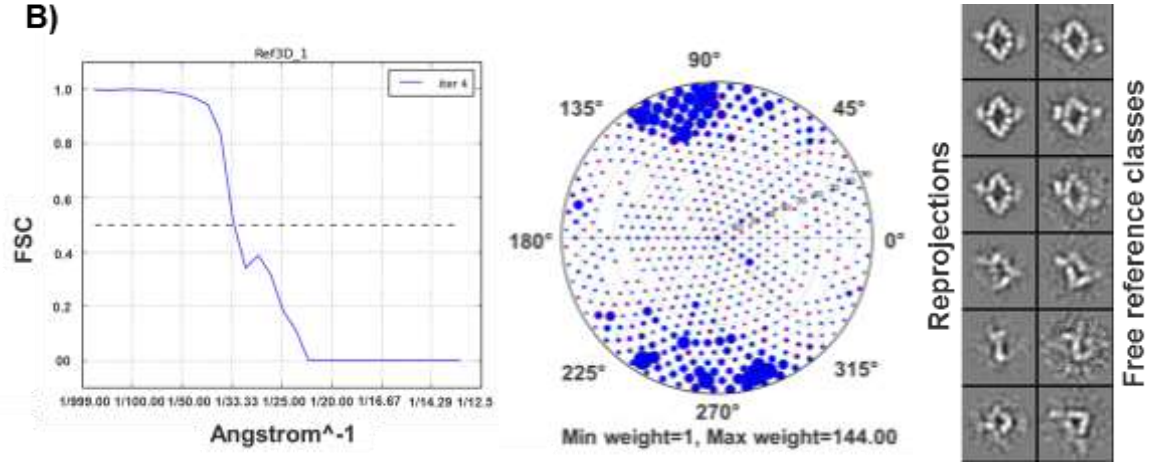

Figure 2.30: 3D reconstruction of the complex formed by the mAb1A3-mAb1A12. A) The final map of the complex at a resolution around 30 Å fitted with an immunoglobulin PDB structure (1IGT, green colored) and the structure of the fHbp (3KVD, red colored). B) FSC curve (on the left) and the angular distribution (in the center) related to the EM volume generated using the projection matching. The panel on the right shows the comparison between projections of the final volume (left) and reference-free classes (right).

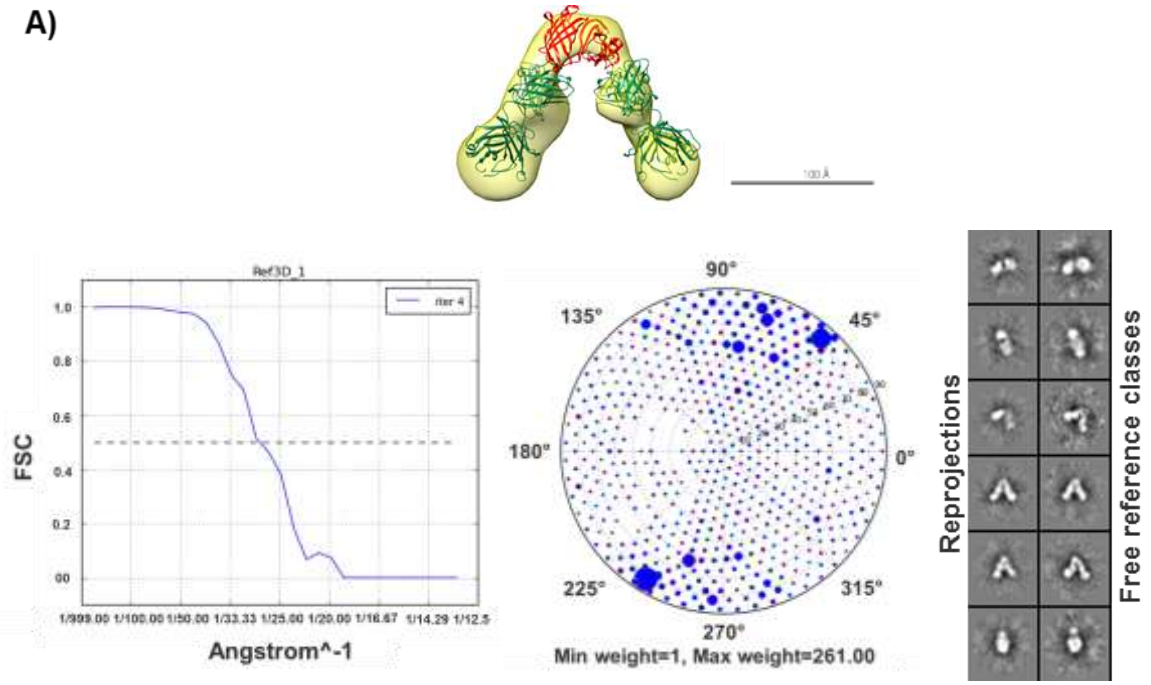

Figure 2.31: 3D reconstruction of the complex formed by the fab7B10-fab2C1. A) The final map of the complex at a resolution around 30 Å fitted with the fabs portion of the immunoglobulin PDB structure (1IGT, green colored) and the structure of the fHbp (3KVD, red colored). B) FSC curve (on the left) and the angular distribution (in the center) related to the EM volume generated using the projection matching. The panel on the right shows the comparison between projections of the final volume (left) and free reference classes (right).

The electron density map of the complex formed by the cooperative couple of fabs (Figure 2.32B) was then fitted in the 3D EM models of the mAb-mAb complex (Figure 2.32A) to assess the angular flexibility due to the binding of the antibody to the antigen (Figure 2.32C). The structures perfectly match when overlapped.

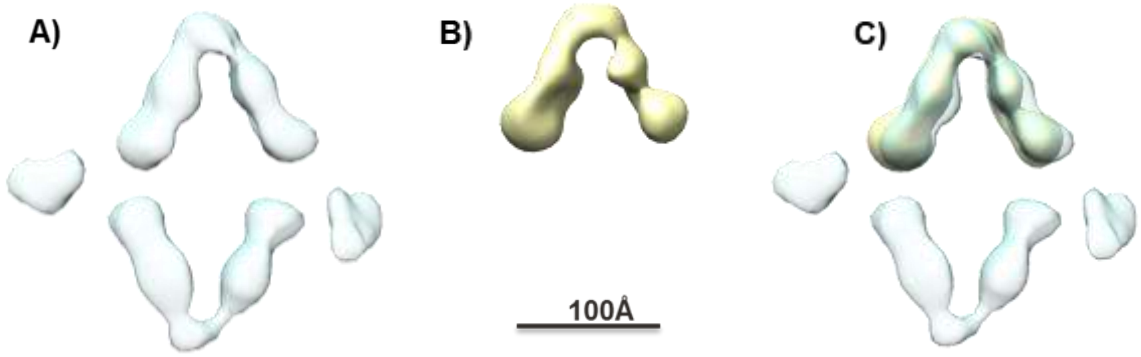

Figure 2.32: Isosurfaces of the 3D reconstructions of the couple of fabs and mAbs 7B10-2C1. A) The structure of the mAb complex. B) Fab complex C) Overlapping between the two structures. Scale bar is reported on the bottom.

To confirm the differences observed between the cooperative complexes, an overlapping of the 3D maps was performed (Figure 2.33C). The data confirm that both the immune complexes assumed the same rhomboidal shape and that a flip of one of the fab of the complex formed by mAb1A3-fHbp-mAb1A12 along the z axis occurs.

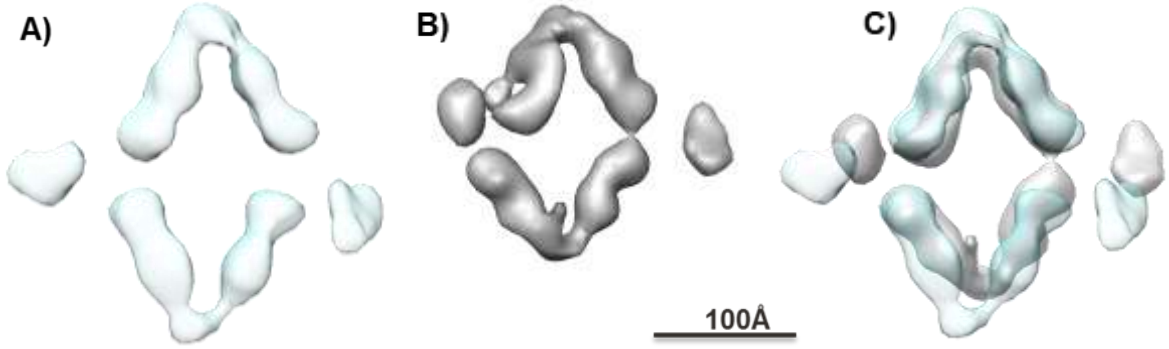

Figure 2.33: Isosurfaces of the 3D reconstructions of the couple of mAbs 7B10-2C1 and 1A3-1A12. A) The structure of the mAb7B10-fHbp-mAb2C1 complex. B) The complex formed by the mAb1A3-fHbp-mAb1A12. C) Overlapping between the two structures. Scale bar is reported on the bottom.

2.4.8 fHbp-antibodies: SPR competition assay with fH

The differences in the repertoire of serum bactericidal antibodies against fHbp found between human or primate and mouse were scribed to the complex formed between factor H and the fHbp antigen. This binding, specific for human and primate factor H, restricts the available epitopes to fHbp regions external to the fH binding site (Beernink et

al., 2015). In order to investigate the influence of the cooperative couples on the antigen-fH binding, a biophysical analysis using SPR techniques was performed. The same amine coupling method was used to bind cooperative mAbs to the CM5 chip surface with the experimental condition similar to those used for the discrimination of cooperativity. After capturing fHbp, all the complexes were tested directly for binding to human fH. The presence of an additional signal in the three profiles indicates that mAb1A3, mAb1A12 and mAb7B10 are able to form a ternary complex with the fHbp and the human fH (Figure 2.34A). A greater constant of association (Ka) of the human factor H for the mAb1A12-fHbp complex (green curve) is notably even considering the different capturing of the antigen fHbp between the mAbs. Moreover, different constants of dissociation are detected in the binding of the fH to the antigen. Particularly, a faster detaching of the fH from the complex formed between the fHbp and the mAb1A3 (red curve) and the mAb1A12 (green curve) (Figure 2.34B) is revealed compared with the one from the fHbp-mAb7B10 complex for the fH binding.

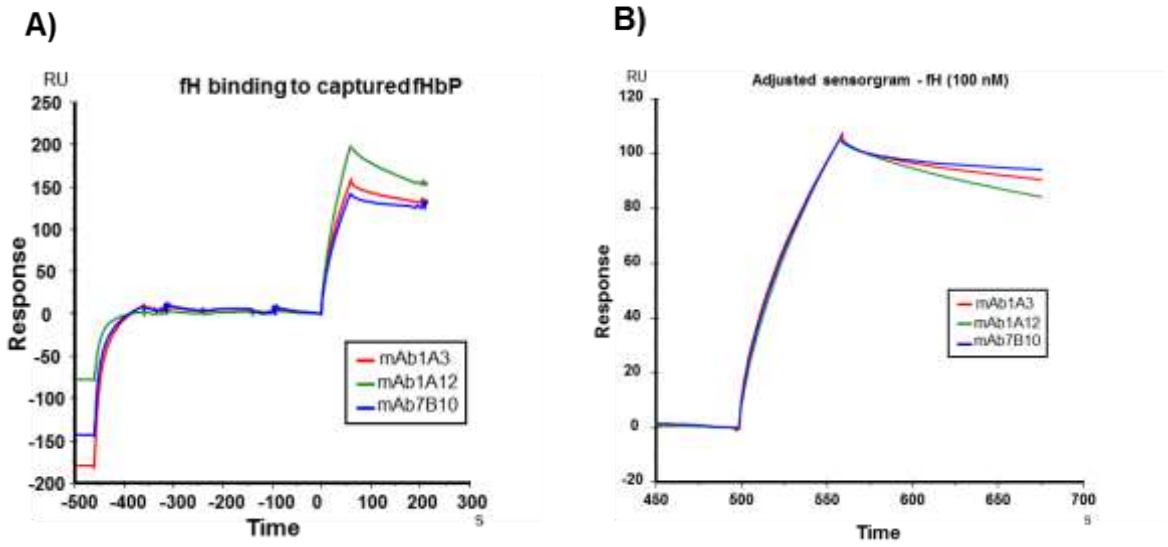

Figure 2.34: Sensorgrams profile of the SPR fH binding analysis performed using mAb1A3, mAb1A12, mAb7B10 amine coupled to the sensor surface. The color legend is reported in each figure and indicates the mAbs attached to the surface. A) The sensorgram reports the profile of the fH binding on the complex between the mAb1A3, mAb1A12 and mAb7B10 and the fHbp. The sensorgram profile is aligned at the sample baseline. B) Zoom of the binding profile of the fH to the mAb-fHbp complex normalized and aligned at the sample baseline.

The next step was to perform the fH binding experiment in the presence of the cooperative complex already formed. Thus the second mAb was injected before the fH. The sensorgrams demonstrate the formation of a quaternary complex: a third signal is

generated on the baseline of the stable cooperative complex profile (Figure 2.35). In the case of mAb1A3 and mAb7B10 coupled to the chip, the sensorgrams detect a higher affinity of fH binding in absence of the second mAb (Figure 2.35A and Figure 2.35C). The normalized sensorgrams show a slow dissociation in the signal of the fH bound to the complex formed by mAb1A12-fHbp-mAb1A3 (Figure 2.36B, green curve).

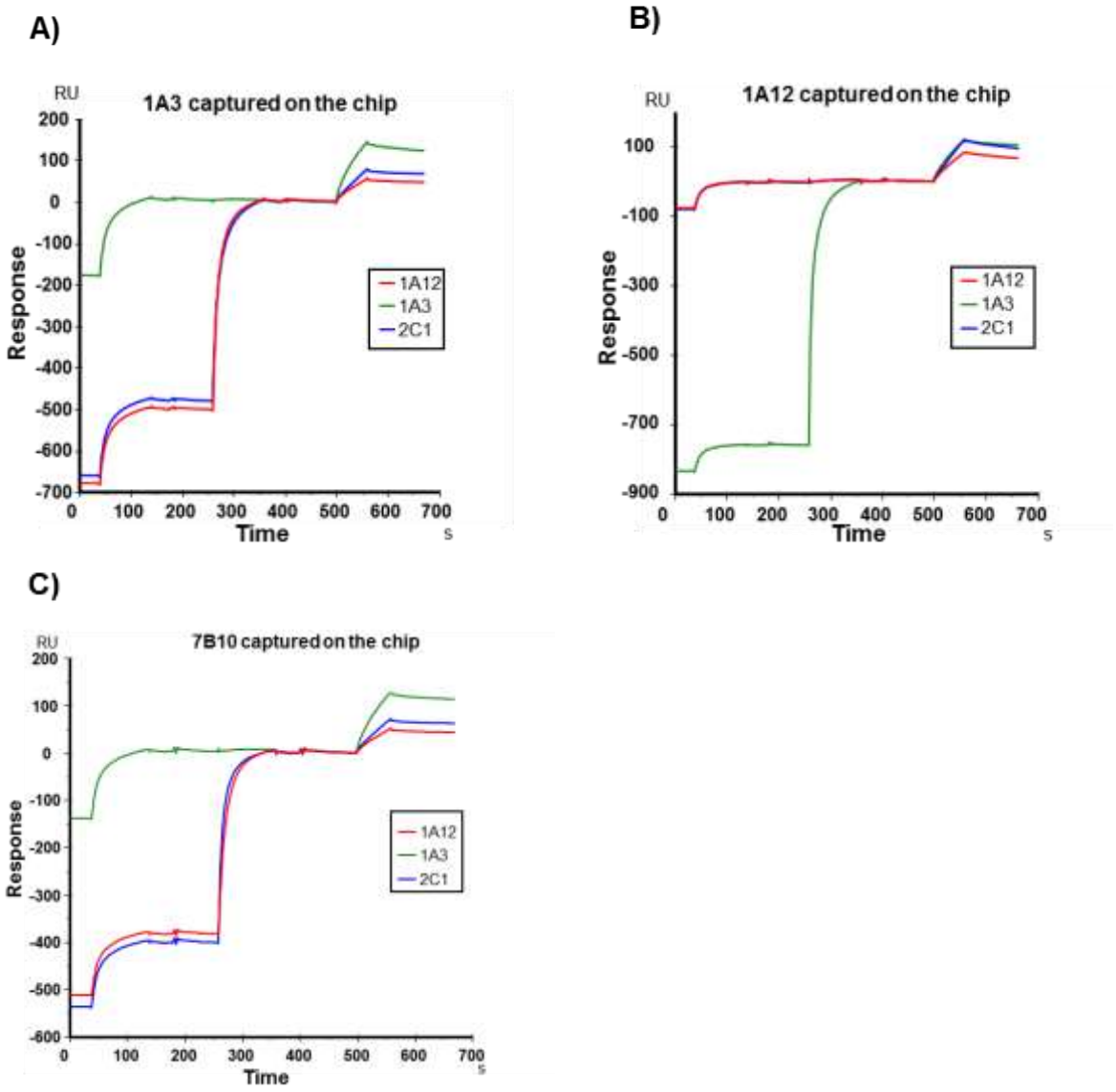

Figure 2.35: Aligned sensorgrams on the sample baseline showing the SPR fH competition assay. The profiles show the formation of a quaternary complex using mAb1A3, mAb1A12 and mAb7B10 amine coupled on the CM5 sensor-chip. A) Sensorgram profile of mAb1A3 coupled on the chip. B) Sensorgram profile of mAb 1A12 coupled on the chip. C) Sensorgram profile of mAb7B10 coupled on the chip.

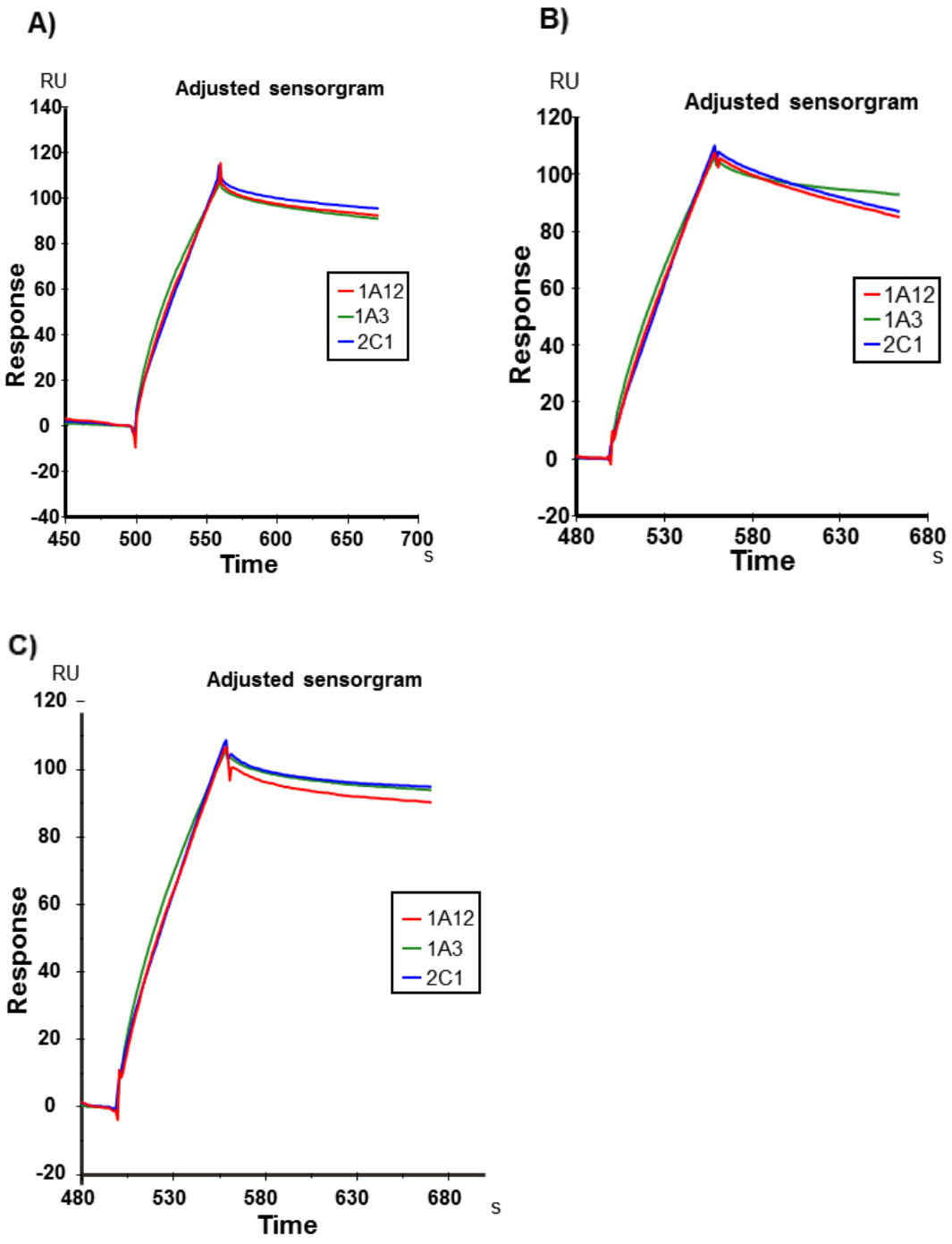

Figure 2.36: Normalized and aligned sensorgrams on the sample baseline of the SPR fH competition assay. The profiles show the different dissociation of the quaternary complex formed by the cooperative couple of mAbs, the antigen fHbp and the human fH. A) Sensorgram profile of mAb1A3 coupled on the chip. B) Sensorgram profile of mAb 1A12 coupled on the chip. C) Sensorgram profile of mAb7B10 coupled on the chip.

2.4.9 Cooperative couple of mAbs is able to recruit the C1q

The ability of the cooperative mAbs to recruit the C1q was verified by an ImmunoGold TEM (IG-TEM) to confirm the binding of the C1q to the cooperative couple of mAb7B10-

mAb2C1 bound to the fHbp express on the surface of bacteria. OMVs naturally released by the bacterium and exposing the fHbp var.1 on the surface were used as a fHbp-presenting system. The micrographs show intact OMVs decorated by with gold particles linked to the secondary antibodies anti-C1q (Figure 2.37).

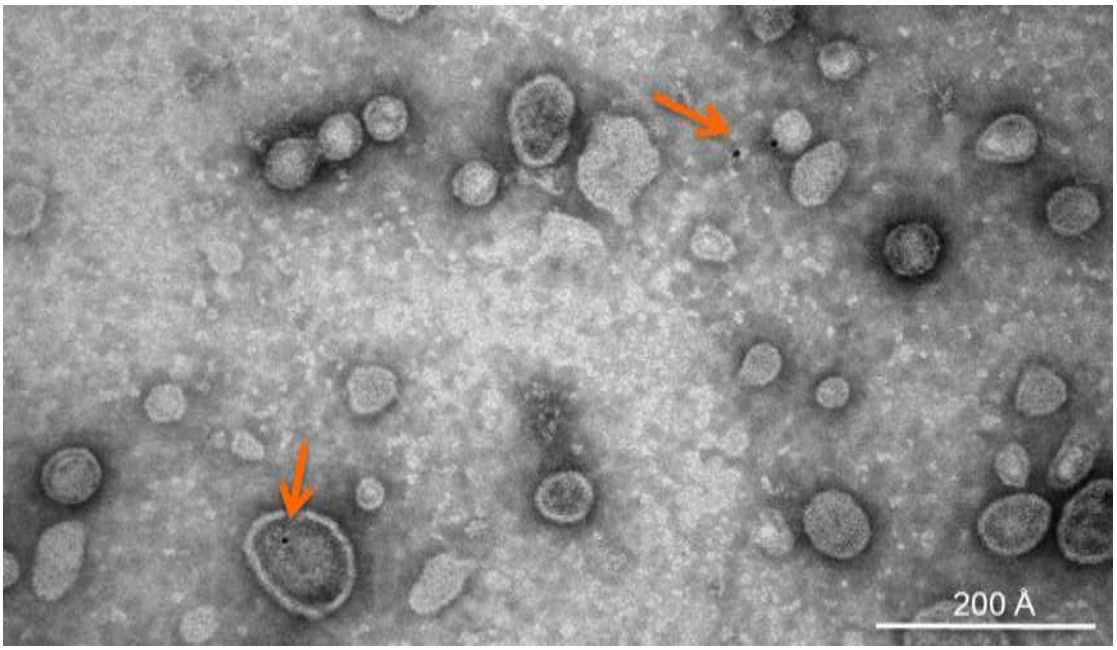

Figure 2.37: Micrograph of the immunogold assay to detect the recruitment of the C1q from the cooperative couple of mAbs on the OMV surface. Gold particles are indicated by orange arrows.

2.5 Discussion

The cooperative bactericidal activity between monoclonal antibodies is a biological mechanism that occurs when mAbs, that are individually not or low bactericidal, become bactericidal when used in combination. This biological event is still poorly understood, but several have been done during the years for a thorough understanding of antibody-based mechanisms of protection against bacterial diseases. Beernink *et al* firstly demonstrated that couples of murine mAbs anti-fHbp can elicit strongly bactericidal titers only if one of the two mAbs is able to inhibit the binding between the fH and the antigen fHbp (Beernink et al., 2008). This suggested that the bactericidal activity largely depended on the classical complement pathway as the alternative pathway would be downregulated by the bound fH (Beernink et al., 2015). Surprisingly the key role of the fH binding has been proved incorrect by the recent study on the human repertoire of mAbs elicited by the fHbp where human anti-fHbp fabs lacked fH inhibition. Moreover, a decrease in the bactericidal activity and in the C3b deposition were observed when anti-Bb mabs were used blocking the alternative pathway. Thus suggesting an important involvement of the alternative pathway (Beernink et al., 2015). Moreover an optimal relative orientation of the two mAbs bound to the antigen has been hypothesized as a necessary step for the recruitment of C1q and the consequent activation of the classical complement pathway (Faleri et al., 2014; Giuntini et al., 2012; Konar et al., 2013).

Here we used both murine cooperative couple and human cooperative and non-cooperative couples of monoclonal antibodies to deeply investigate the structural formation of the synergic complexes in order to shed light into the molecular mechanism at the basis of the cooperativity.

Since it is known that only a simultaneous and stable binding of mAbs onto the antigen allows an efficient recruitment of the C1q, we firstly analyze the stability of the complex showing interestingly, that the murine monoclonal antibodies although able to bind simultaneously the antigen they are incapable to form a stable complex with a constant and defined geometrical shape. While the human cooperative couples of monoclonal antibodies form a very stable and geometrically well-defined quaternary complex with the fHbp. The comparison of the 3D reconstruction of the murine cooperative complex with the human cooperative one strongly underlines the higher level of flexibility and instability of the first complex versus the human one. Although previously published that at least one murine mAb should inhibit the fH binding for a cooperative activity and that the human mAbs do not map in the fH binding site, we were able to prove that a simultaneous

binding of fH to the immune cooperative complex occurs with cooperative couples of mAbs. Thus, the comparison between the murine and human cooperative complexes suggests a possible different mechanism for inducing protection. An hypothesis could be that the murine monoclonal antibodies in the complex needs to hamper the fH binding in order to strongly activate the complement pathways whereas the human monoclonal antibodies couple, lacking completely the capability of fH binding, could serve as sites for deposition of C3b, thus overcoming the down regulatory activities of fH (Beernink et al., 2015). Moreover the geometrical relationship between the antigen and the human monoclonal antibodies in the complex where not influenced by the human antibody flexibility. Both the reference classes and the 3DEM maps of fab and mAb complexes showed that the angle formed between the fHbp and the antibodies is the same indicating that the reciprocal orientation of the human monoclonal antibodies is only dependent on its epitope location on the antigen. Since this finding was observed with the complex in solution where the single components of the complex could have more degrees of freedom, we expect an important decrease in flexibility when the complex is formed on bacterial surface. Although the new constrains, the immune complex should be still able to recruit the C1q protein, as showed by the immunogold assay anti-C1q performed on the outer membrane vesicles incubated with the cooperative couple of mAb7B10-mAb2C1.
Finally, the high variability of assembly for non-cooperative human monoclonal complexes proves the structural dissimilarities with the cooperative human complexes thus identifying the partial epitopes overlapping as the main cause in the absence of complex formation. A detailed epitope analysis with HDX_MS techniques confirms the last hypothesis. All the evidences based on our findings revealed that the cooperativity takes place only with mAb epitopes in different domains of the fHbp generating stable and well defined shape complexes whereas the non-cooperativity is due to overlapping epitopes resulting in the lack of stable simultaneous binding.

NadA – structural characterization of NadA var.3

Chapter 3

3.1 Introduction

Trimeric autotransporter adhesins are a widespread family of outer membrane proteins in Gram-negative bacteria (Linke et al., 2006; Lyskowski et al., 2011). As mediators of adhesion, TAAs play a crucial role in attaching bacteria to cell surfaces present in their environment thus resulting to be determinants of infection and host colonization. The TAA family includes YadA of *Yersinia enterocolitica* (Bolin et al., 1982), Hia of *Haemophilus influenza* (St Geme & Cutter, 2000), UspA1 and A2 of *Moraxella catarrhalis* (Lafontaine et al., 2000), BadA of *Bartonella henselae* (Riess et al., 2004), SadA of *Salmonella enterica* (Raghunathan et al., 2011), Eib proteins of *Escherichia coli* (Sandt & Hill, 2000) and NadA of *Neisseria meningitidis* (Linke et al., 2006) (Figure 3.1).

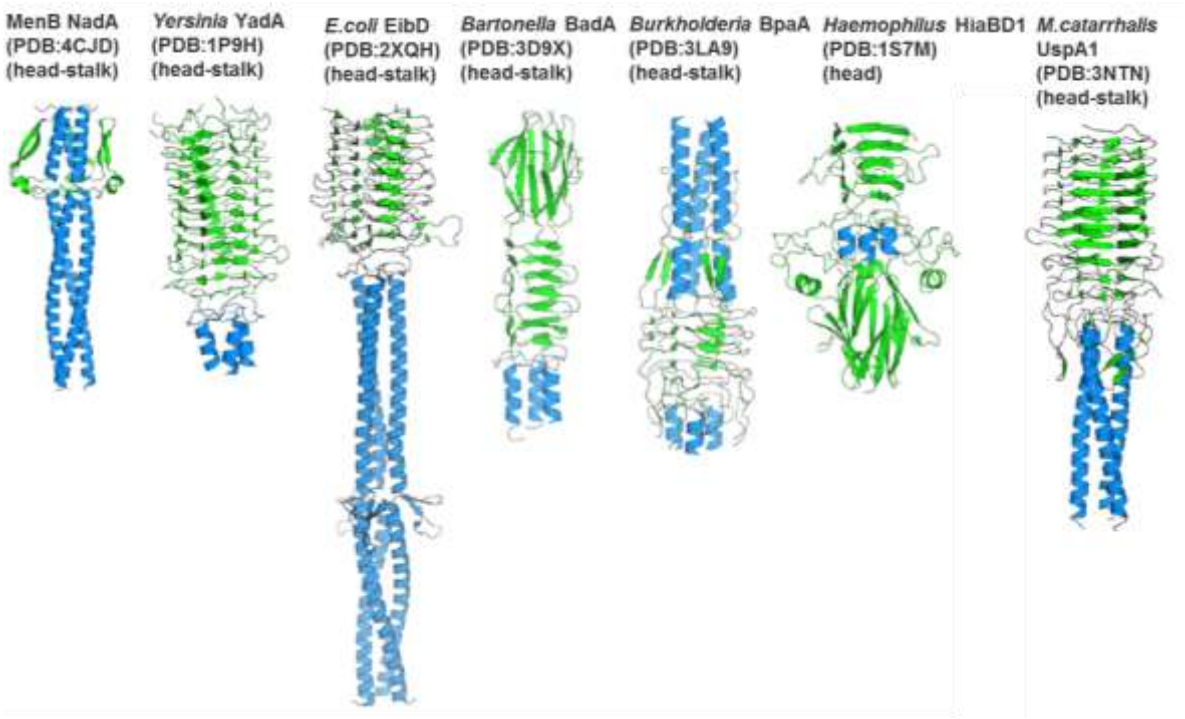

Figure 3.1: Comparison between NadA and other trimeric autotransporters adhesin. β-sheet are reported in green; α-helices are colored in blue. Figure from Malito et al., 2014.

All members of this family share common architecture consisting of variable arrays of a slender stalk, a bulkier head region, and an ending C-terminal membrane anchor (Bassler et al., 2015; Linke et al., 2006) (Figure 3.2).

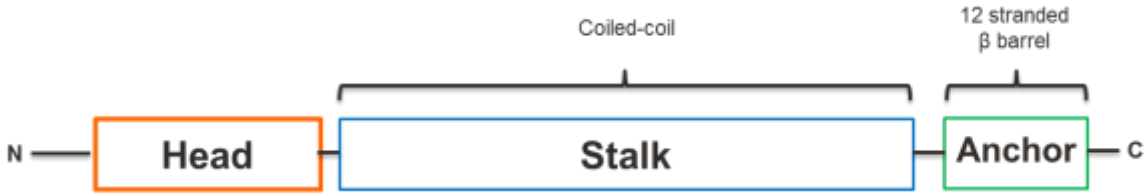

Figure 3.2: Base composition of the structure of the TAA family.

The autotransporter domain (membrane anchor domain), invariably found at the C terminus of the proteins, is the only domain present in all the TAAs (Linke et al., 2006). The barrel is thought to provide the pore through which the upstream head and stalk domain exit the periplasm (Leo et al., 2012); after the export is complete, the helices of the anchor trimerize to form a coiled-coil at the center of the barrel, obstructing the pore and stabilizing the structure (Meng et al., 2006). Indeed the stalk domains of TAAs are fibrous, highly repetitive structures that are rich in coiled-coils and extremely variable in length. Coiled-coils are bundles of α-helices that interact through hydrophobic residues arranged in a pattern of seven residues (Hartmann et al., 2009; Malito et al., 2014).

The stalk function is to project the head domains away from the bacterial cell surface (Bassler et al., 2015; Linke et al., 2006). Recently Koiwai and co-workers identified in this region the structural elements necessary to both the flexibility and toughness of TAAs which provide the resilience needed by the fibers to exert adhesive properties across a wide range of conditions. A sufficient rigidity is essential for the extension of the TAA to function as adhesion whereas the flexibility is important to reach the target surfaces (Koiwai et al., 2015). The last base domain is the head that is the most variable region commonly formed by β-strands oriented perpendicularly to the fiber axis and is mainly responsible for binding the host cellular receptor (Bassler et al., 2015; Malito et al., 2014).

Despite this basic overall common structure rearrangement the considerable diversity present between the TAA members could reflect the constant need of the pathogen to modify the virulence determinants in the face of adapting host defenses (Bassler et al., 2015; Linke et al., 2006).

The antigen Neisserial Adhesin A presents a novel structure in the N-terminal domain that, in contrast to the other TAAs, lacks a truly independent globular head domain. The crystal structure of the NadA var.5 (PDB entry: 4CJD) solved by Malito *et al*. reveals that the antigen possesses an almost exclusively coiled-coil and forms wing-like structures protruding from the stalk and packed against the N-terminal helices in the head position (Malito et al., 2014) (Figure 3.3). Interestingly the crystal structure showed clear low σ-level electron densities in the region between A137 and T199, in the most C-terminal

region of the elongated stalk. This suggests that the three helices of the stalk are less stable in this region, likely resulting in partial unwinding of the coil and therefore in some flexibility and disorder (Malito et al., 2014). The NadA family has been genetically divided in two subgroups that share overall amino acid sequence identities of 45-50%. The group I includes the three most common variants, NadA var.1, NadA var.2 and NadA var.3, the variant included in Bexsero® vaccine, that are immunologically cross-reactive. The group II comprises the three rarer variants that are NadA var.4, NadA var.5 and NadA var.6. It was demonstrated that the sequence identity inside each group is 95% and 90%, respectively (Bambini et al., 2014; Malito et al., 2014).

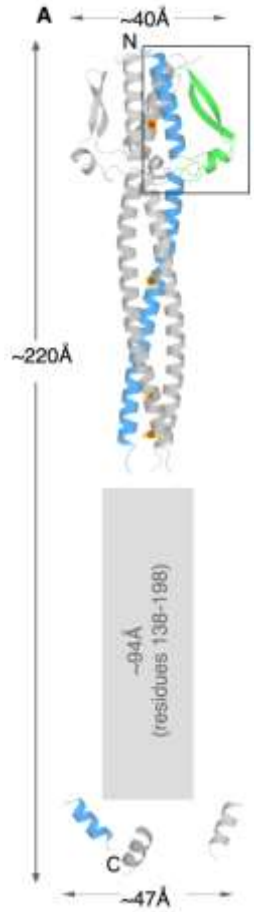

Figure 3.3: Ribbon of the crystal structure of NadA var.5 (PDB entry: 4CJD). Coiled-coil portion of the monomeric NadA var.5 is colored in blue. The wing-like insertion of the head are green colored. The other two symmetry-related molecules are shown in gray. The large rectangular gray-shaded outline shows the region of low-σ electron density. Adapted from Malito et al., 2014.

Unfortunately, the structure of the vaccine variant is not available. Extensive attempts to crystallize NadA var.3 vaccine constructs were unsuccessful due to the long, flexible stalk that hindered the crystallization attempts (Magagnoli et al., 2009; Malito et al., 2014).

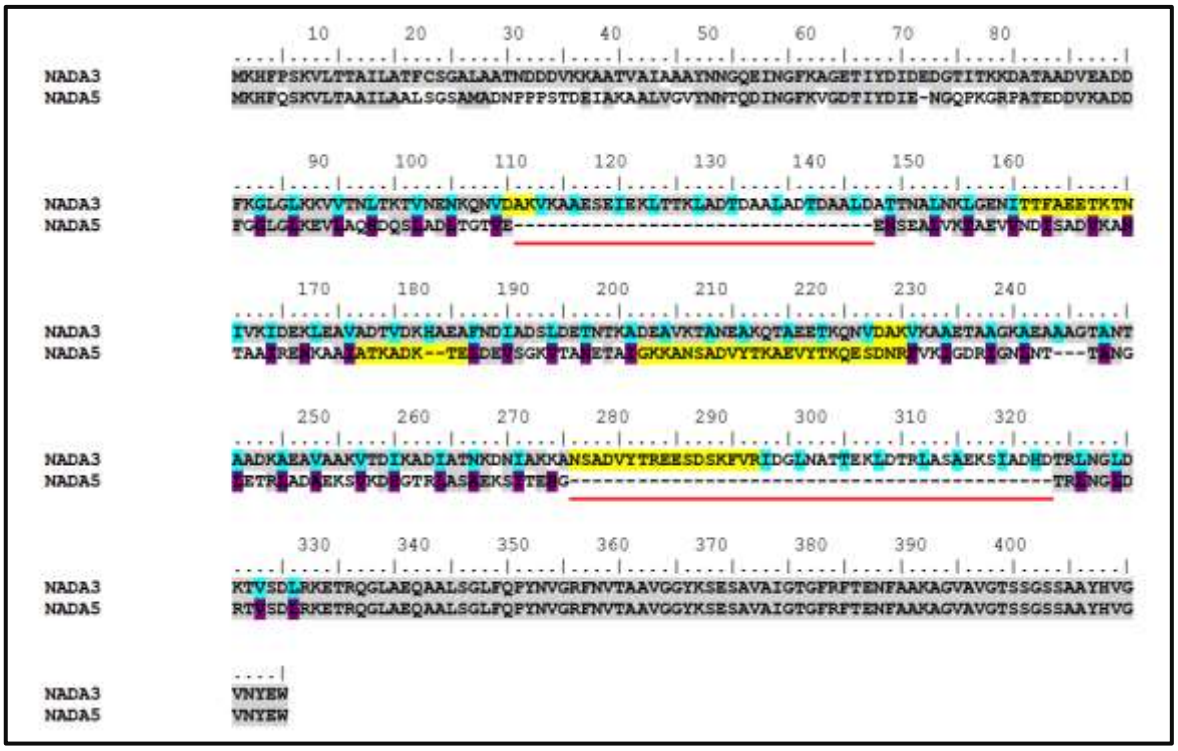

Figure 3.4: Sequence alignment between NadA var.3 and NadA var.5. Sequence identity is highlighted in grey; the heptad repeats of the coiled-coil is reported in dark purple shading and in cyan shading on the NadA var.5 and NadA var.3, respectively. The insertion of the NadA var.3 respect to the NadA var. 5 sequence are underlined in red; the yellow shading shows the predicted coiled-coil interruptions in the sequence of the NadA var.3 and of the NadA var.5. This image is adapted from Malito et al. 2014.

The sequence analysis of both NadA var.3 and NadA var.5 revealed that the stalks have a canonical left-handed trimeric coiled-coil composed by several heptad repetition (Figure 3.4, marked on the sequence of the NadA var.5 with dark purple while cyan shading is used on the sequence of NadA var.3) with the first heptad repeat starting at the N-terminus immediately after the 24 amino acids of the leader peptide. Two long insertions are detected in the NadA var.3 compared with the sequence of the NadA var.5 covering a total of 81 residues (Figure 3.4, underlined in red). Notably the heptad repeats in the NadA var.3 are interrupted by three regions with lack of coiled-coil periodicity (Figure 3.4, yellow shading).

As all the previous crystallization attempts failed, to investigate the structure of NadAV3 due to the high flexibility of the stalk an electron microscopy approach was used. Previously an immunogold electron microscopy performed on the whole life bacteria allowed to detect the relative amount and distribution of the NadAV3 molecules on the bacterial surface (Figure 3.5A). Moreover, a high resolution EM analysis performed

directly on the bacterial surface revealed the presence of the antigen spreads out from the capsule (Figure 3.5B and Figure 3.5C, white arrows).

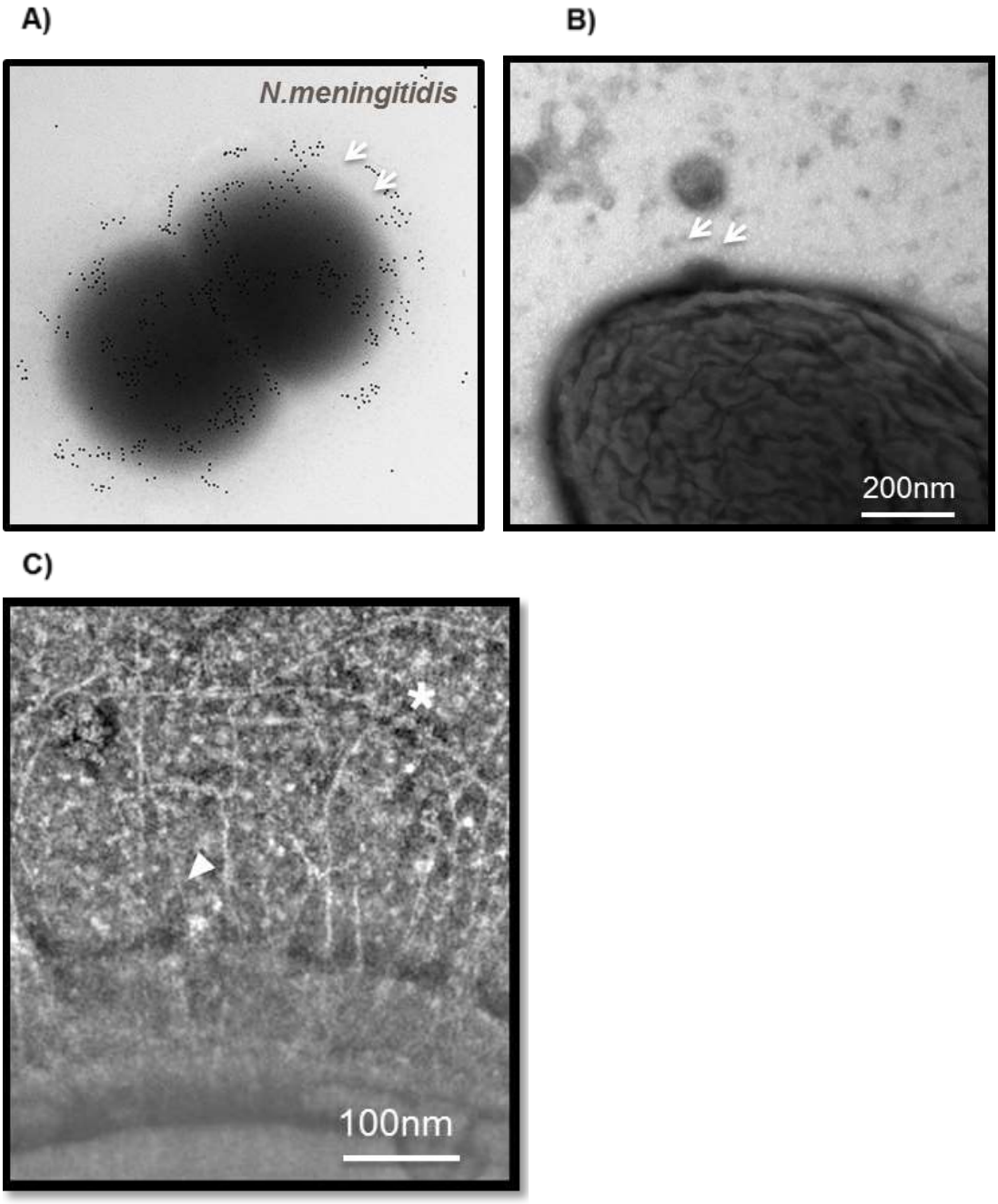

Figure 3.5: Transmission Electron Microscopy analysis of the NadA var.3 performed directly on the N.meningitidis bacterium. Scale bar is reported at the bottom of each panel. A) Immunogold assay detects the distribution of the antigen NadA var.3 on the bacteria. B) A high resolution negative staining revealed the presence of the NadA var.3 onthe bacterial surface. White arrows indicate the antigen. C) A zoom of the bacterial surface with the capsule. White arrow indicates individual stalk of NadAV3 and the asterisks indicates the position of individual head.

3.2 Aim of the work

Unveiling the structure of the NadA antigen is a key step for a complete knowledge of its role in the bacterial pathogenesis. Neisseria adhesin A is a member of the bacterial Trimeric Autotransporter Adhesins able to mediate adhesion to and entry into epithelial cells (Capecchi et al., 2005; Comanducci et al., 2002; Cotter et al., 2006; Surana et al., 2004). At least six NadA variants have been identified so far (Bambini et al., 2014). The NadA var.3 is included in the licensed vaccine against the *N.meningitidis* strain B, Bexsero®. Although extensive attempts to crystallize NadA var.3, no crystal structure was obtained up to date, probably due to the long and flexible stalk that prevented the crystal packaging (Malito et al., 2014). We decided therefore to use single particle Cryo Electron Microscopy, a very powerful technique that has emerged in the last decade as the method of choice to the study of challenging systems, to reveal the NadAV3 structure and the mechanism of action during the adhesion step.

Finally the analysis of the sequence features of NadA var.3 coupled to structural characteristics revealed by cryo-EM is expected to shed light on the role of different domains of the NadA var.3 in both the flexibility and toughness of the molecule.

3.3 Experimental procedure

3.3.1 NadA: cloning, expression and purification

The *nadA* var.3 gene fragments (from *N. meningitidis* strain 2996, UniProt Q8KH85) were cloned by PCR, using the PIPE (polymerase incomplete primer extension) technique as described by Malito et al., 2014 (Malito et al., 2014).

The cloned fragment lacked both the first 23 residues of NadA which encode a signal peptide for protein export and the C-terminal transmembrane domain. The fragment was inserted into a modified pET-21 vector (Novagen), enabling cytoplasmic expression of the NadA var.3 protein with an N-terminal 6-His tag to facilitate protein purification.

The NadA expression construct was transformed into *E. coli* BL21 (DE3) cells. Production of recombinant NadA construct was performed using the EnPresso Tablet Cultivation Set (BioSilta) growth system supplemented with 100 µg/ml ampicillin. Bacteria were grown at 30°C for a total of 40 hours and target protein production was induced by the addition of 1 mM IPTG (isopropyl β-D-thiogalactoside). Cells were harvested by centrifugation at 6400 x *g* for 30 minutes at 4°C; resuspended in 50 mM sodium phosphate pH 8.0, 300 mM NaCl, and lysed by sonication (Qsonica Q700) for 5 minutes with cycles of 30 seconds of sonication (40% amplitude) interspersed with 30 seconds on ice. Cell lysates were clarified by centrifugation at 36200 x *g* for 30 minutes, and the supernatant was filtered using a 0.22 µm membrane (Corning filter system) prior to protein purification.

The protein was purified at RT using an AKTA purifier 10 system (GE Healthcare) firstly by Ni-affinity chromatography (5mL HiTrap Ni-NTA column) and then by SEC on a HiLoad (16/60) Superdex 75 column equilibrated in 20 mM Tris–HCl, 150 mM NaCl pH8.0.

The quality of the final NadA sample was checked using 4–12% SDS–PAGE gradient gels in MES buffer and also by analytical SEC using a Superdex 200 Increase 3.2/300 column in a AKTA Mycro system (GE Healthcare) (Figure 3.6)

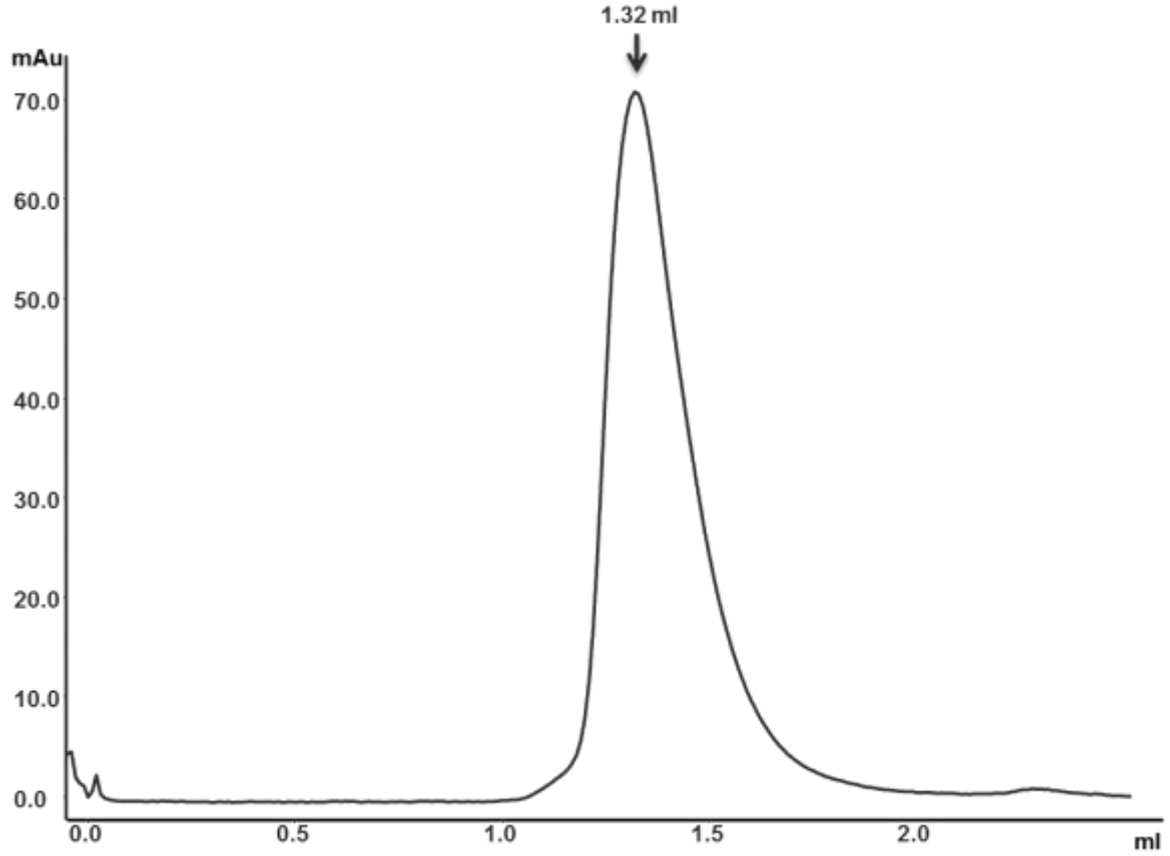

Figure 3.6: Size exclusion profile of the NadA var.3 purification

3.3.2 NadA: Negative Staining Transmission Electron Microscopy (NS TEM)

The antigen was firstly tested using negative staining electron microscopy in order to investigate the degree of flexibility of the long stalk present at the C terminus.

A fraction of the purified NadA var.3 was diluted to 0.05 mg/ml in 20 mM Tris, 150 mM NaCl, pH 8 and loaded onto a 400-square mesh grid of carbon/formvar (Agar Scientific) rendered hydrophilic with 15 mA current for 20 second by glow discharge Quorum Q150AS. The excess of the solution was blotted off using Whatman® filter Paper No.1 (SIGMA-Aldrich) and then the grid was negatively stained with 1% of Uranyl Acetate in water for 30 seconds. Excess stain was wicked off with Whatman® filter Paper No.1 (SIGMA-Aldrich). The specimen was imaged using a Tecnai G2 Spirit working at 120 kV with a side mount Olympus Morada 2Kx4K CCD camera and 105000x of magnification. The calibrated pixel size was 3.8 Å/ pixel.

3.3.3 NadA: Cryo-Electron Microscopy (Cryo-EM)

Data collection was performed with Dr.Kasim Sader, FEI (The Netherland). Purified NadAV3 concentrated 1 mg/ml were diluted 1/15 times (0.067 mg/ml) with 20 mM Tris and

150 mM NaCl, pH 7 buffer. Quantifoil R2/2 (400 mesh Cu) grid was rendered hydrophilic with 15 mA current for 90 second by glow discharge in a EmiTech K100X. 2.5 µl the the specimen was deposited onto the grid and vitrified using a Mark IV Vitrobot (FEI Company) with a blotting time of 4 second and humidity of 100% at 4°C. The plunge-frozen samples were imaged with a Titan Krios electron microscope operating at a 300 kV in focus with a Volta Phase Plate (Danev et al., 2014) with focus determined manually at a single offset position. A prototype Falcon 3 detector was used at 47,000 X nominal magnification with a pixel size of 1.75 A/pixel. A total dose of 120 e^{-}/Å was applied to each image.

3.3.4 NadAV3: image analysis and structure generation

The micrographs collected were screened to proceed with the 3D structure generation using Imagic5 software (M.Van Heel), https://www.imagescience.de/imagic.html. The particles in the images presented a clear preferred orientation with only a lateral views probably because the dimensions of the molecules is much larger than the expected ice. Around 5000 particles were automatically selected and boxed into 200 x 200 pixel frames. Within Imagic5, after rotational and translational alignment with a cylinder of the same length and thickness, all the particles were separated in different groups: i) the full length straight particles, ii) the shoert particles, and ii) the full length bend particles. Only the particles having identical length corresponding to the full length homotrimer (290Å) were selected for the reconstruction. A final subset of 2100 particles was created. Due to the difficult alignment of the particles that present a long, thin and flexible stalk, we decided to go through several cycles of rotational, translational and centering. All the pre-aligned particles were than masked with a narrow rectangular mask and used in Multivariate Statistical Analysis (MSA) to generate class averages (M. van Heel, 1984). One of the best class averages was than chosen and its Euler angles set to values α=0, β=90 and γ=0 as a single orientation of a rod-like structure is not necessary a problem as it will likely be able to rotate on its cylindrical axis freely, and therefore fill in all of Fourier space. The Euler angles are defined based on the rotation of the particle around one of the three axis (α, β, γ) of the space (Figure 3.7), Imagic5 - Brazil-School for Single Particle Cryo-EM: hands on.

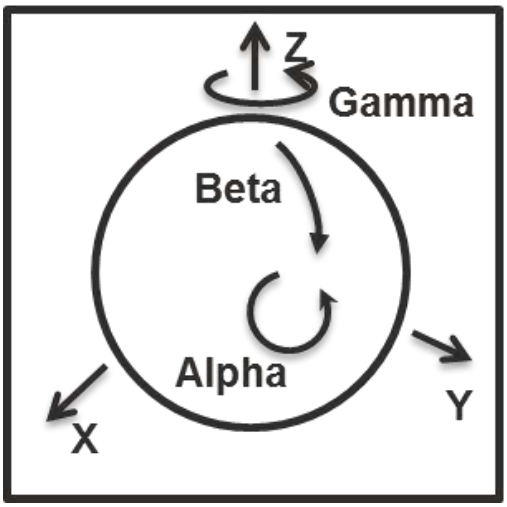

Figure 3.7: Representation of the three angles of rotation around the three axis.The image is taken from the Brazil-School for Single Particle Cryo-EM: hands on.

A 3D reconstruction was then generated starting from the single class average with the newly set Euler angles, point-group symmetry C3 was applied. The first map generated resembled to a star-like reconstruction due to the C3 symmetry applied and to the limited number of images present in the class average. In order to remove the unwanted outer parts of the density we proceeded by masking each 2D section of the 3d map separately using the same mask value used previously. From the masked map an anchor set of images has then been generated by projecting the 3D density and used in the angular-reconstitution command to find out the Euler angles. Images with incorrect Euler angles (β angle too far from 90) were removed and a new 3D reconstruction was calculated using good particles. The process was iteratively repeated until a clean and meaningful 3D map was obtained at a resolution determined as 30.3 Å (FSC=0.5).

3.4 Results

3.4.1 Negative staining EM analysis of NadA var.3

The NadA var.3 purified was firstly tested using negative staining assay in order to evaluate the quality of the sample. The sample on the grid is homogeneously dispersed and shows a thin and elongated portion with a globular part at one end, presumably corresponding to the N-terminal part (Figure 3.8). This result is in agreement with the previous description made by Malito et al. on the NadA var.3 full length protein. Most of the particles are found curved with angular deviation of 30-90° from the straight one underlining the flexibility of the protein confirming the previous published data (Malito et al., 2014).

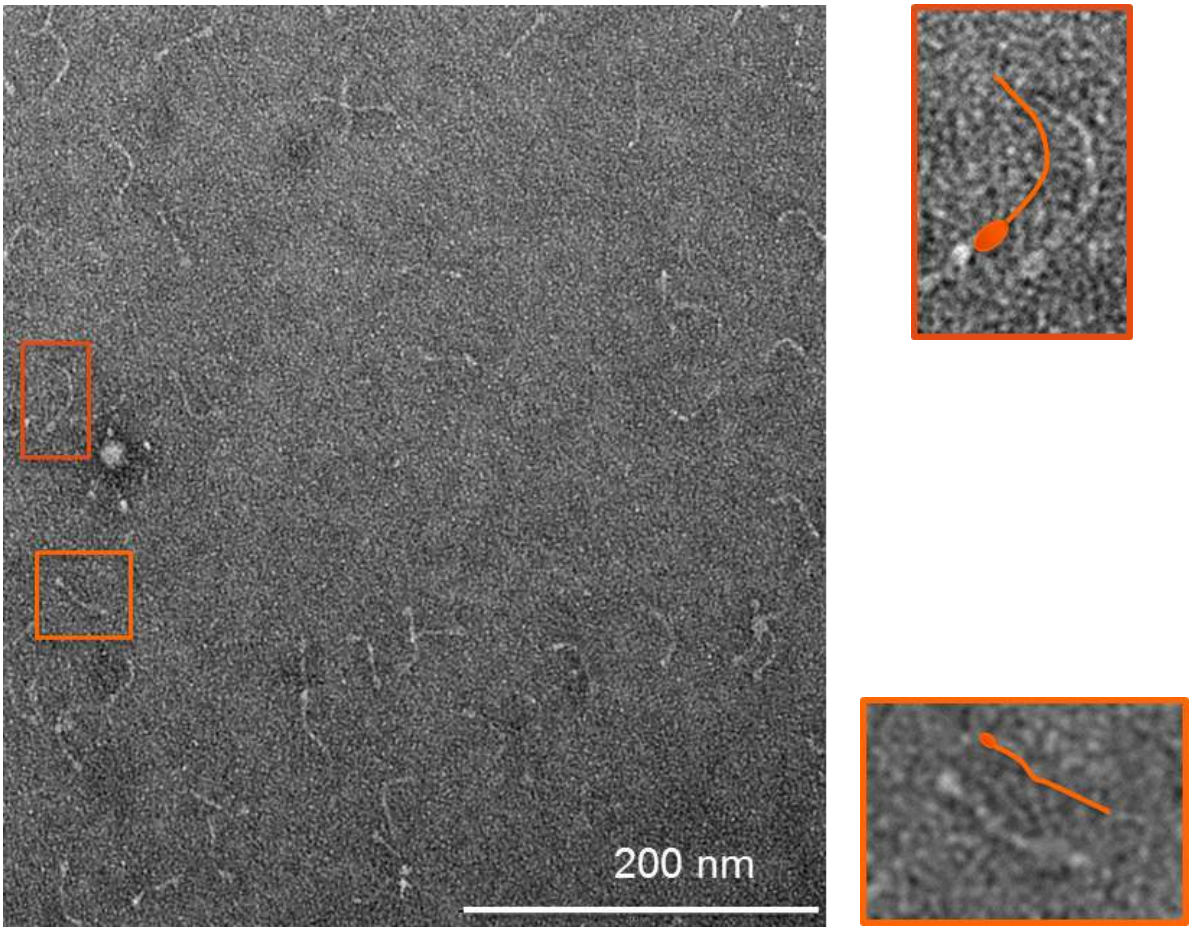

Figure 3.8: Negative staining micrographs of NadA var.3 full length (on the left). The scale bar is reported in white. Particles boxed are showed bandpass-filtered and zoomed (on the right).

3.4.2 Cryo-EM analysis of NadA var.3

To generate a good 3D map, a Cryo EM analysis was performed and the plunge freeze specimen was prepared as described in Material and Method. The images were acquired with a prototype combination of instruments in order to increase the signal-to-noise ratio. NadA var.3 sample is well dispersed in the holes of the grid and appears as a rod-like structure with an elongated part that ends with a spot of major intensity, likely the head (Figure 3.9). These data confirm the previous negative staining results regarding the structure as well as the clear preferred orientation of the particles on the side. Unfortunately the top and bottom views are very rarely and difficult to find due to the small molecular weight. The total length of the protein seems to be slightly different between the particles probably because the long stalk is flexible, as highlighted in the negative staining result, and thus curved in other directions of the plane. The stalk of the NadA var.3 results to be straighter if compared with the negative staining preparation. This difference could be due to the superficial tensions acting in the preparation of the Cryo specimens that lead less curvature in the stalk (Galkin et al., 2012).

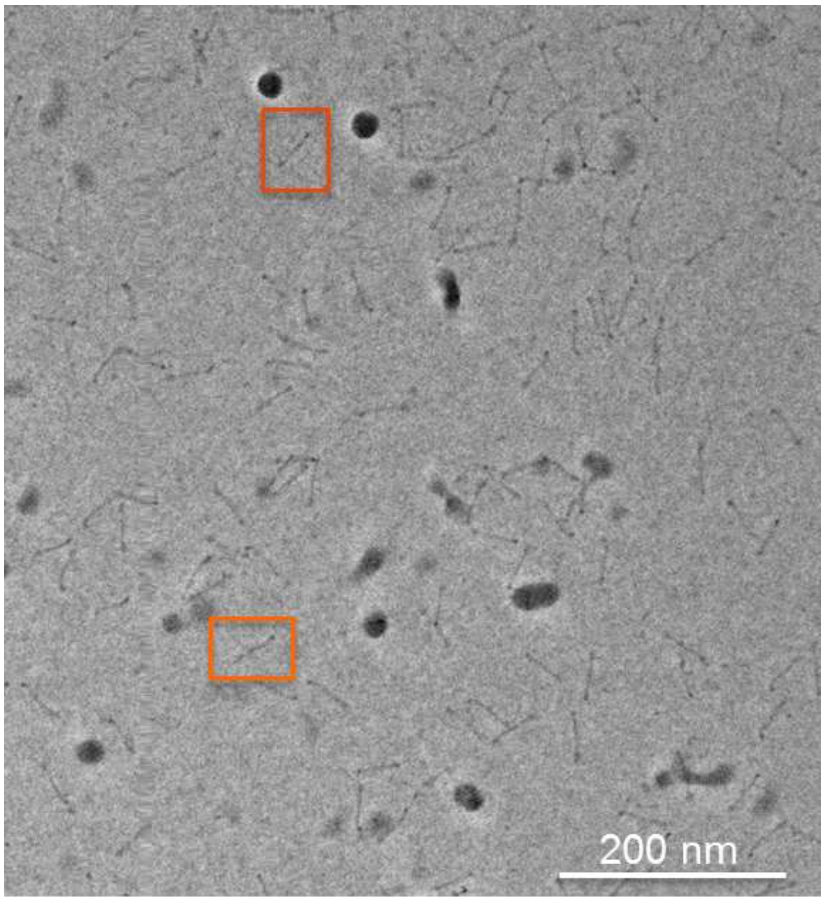

Figure 3.9: Cryo EM micrographs of NadA var.3 full length. The scale bar is reported in white. Particles boxed are showed as example.

However, the molecule assumes either a straight conformation either a smooth curved conformation (Figure 3.10). Nevertheless the majority of the particles are found as linear.

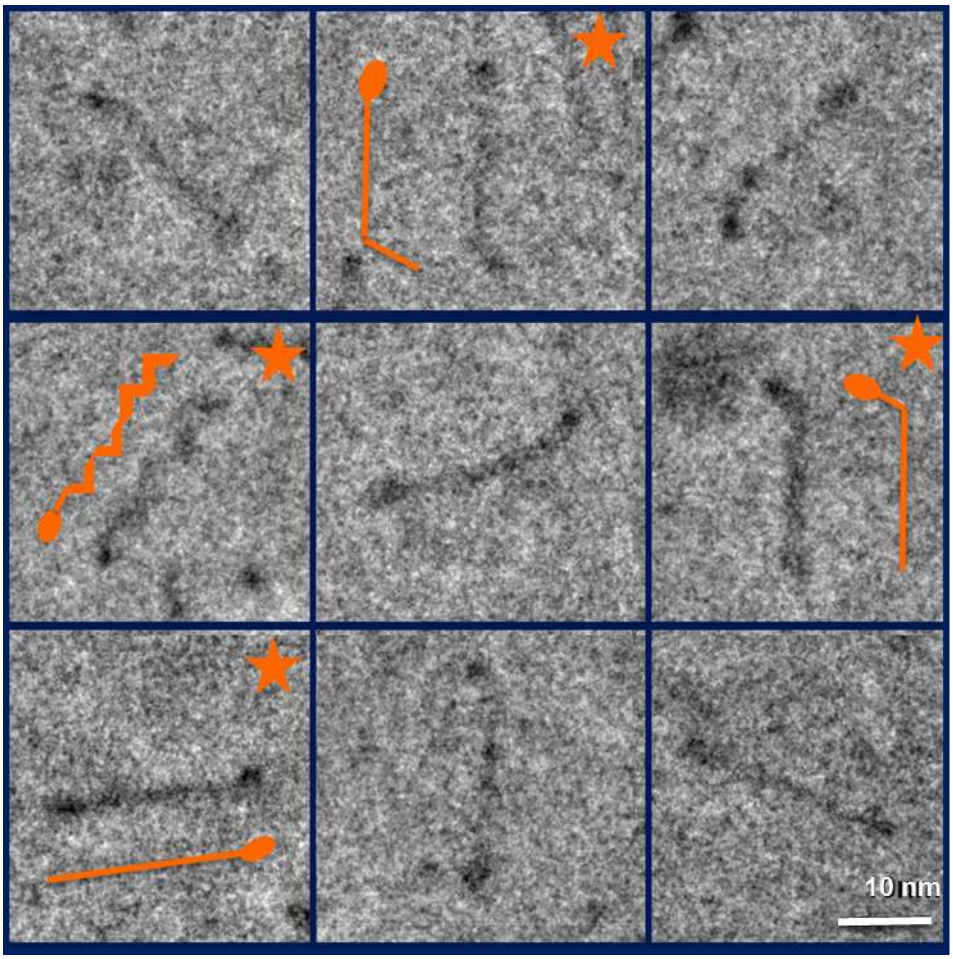

Figure 3.10: Example of NadA var.3 particles. Orange draws next to the particles indicate the shape of the stalk. Orange stars highlight the drawed molecules. The scale bar is reported in white.

3.4.3 Structure generation of NadA var.3

In order to generate the 3D structure, all the micrographs were processed using Imagic5 software. A previous screening to select the best particles suitable for the 3D map generation was performed as described in Material and Methods.

3.4.3.1 2D particle heterogeneity and measurement

All the particles were picked out from the micrographs and aligned as described in Material and Methods. Observing carefully the particles selected, it is notably that some particles have the tendency to be bent in a similar region. To investigate deeply, a measurement of the particles was carried out. The straight particles result in an overall length of around 300 Å with a stalk length of more than 260 Å. The thickness varies from 30 Å in the head region to 15 Å in the stalk region (Figure 3.11A).

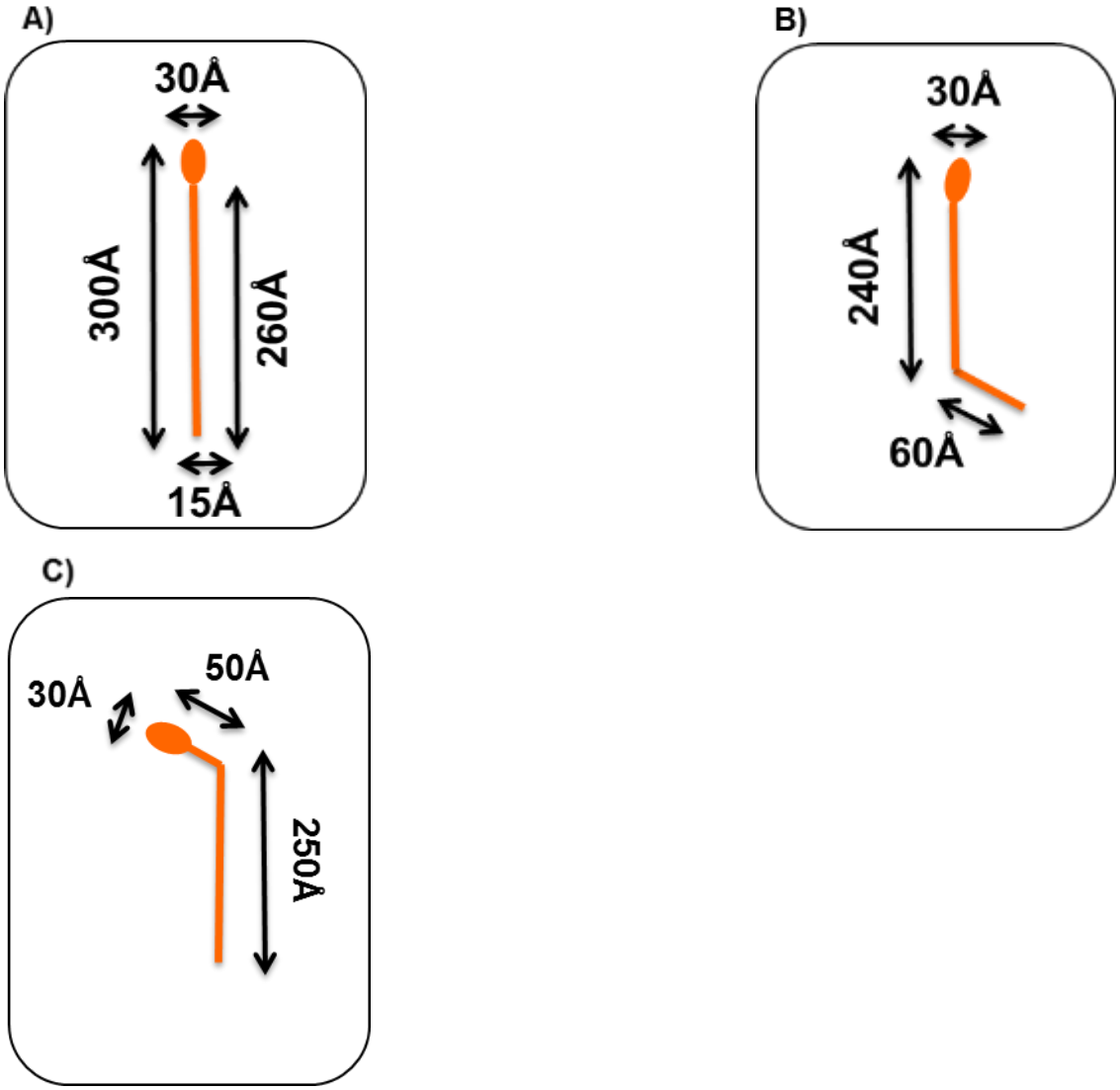

Figure 3.11: Draws reporting the structures and the measurements of the particles found out in the Cryo micrographs. A) Straight particles B) Particles bent at the C-terminal part of the stalk C) Particles bent at the N-terminal part of the stalk.

Several of the molecules observed present a tight and dramatic bent of the stalk in two specific regions of the stalk: the first one around 1/3 of the total molecule length (Figure 3.11B), the second one being present around the 1/3 from the other end (Figure 3.11C). The first type of bent results in a length of around 240 Å for the straight part and around 60 Å for the bent at the C-terminal whereas the second curve leads to around 250 Å for the straight part and around 40 Å for the N-terminal. The two bents are mutually exclusive: they are never present at the same time on the same molecule.

3.4.3.2 2D class average and 3D refinement

To gain information of the NadA var.3 homotrimer structure, a 3D map was generated. All the particles with a strictly straight conformation were selected (Figure 3.12A) as described in the Material and Methods and then aligned through several cycles of rotational, translational and centering and then masked , with a tight rectangular mask, in order to be than classified with MSA method within Imagic5 package (Figure 3.12B). One of the best class averages, with best side view, (Figure 3.12C) was chosen and its β Euler angle fixed to β=90°. This class was then used to generate a preliminary 3D model applying C3 symmetry. The 3D map was successively used to generate 2D projections, with each projection masked by a rectangular mask. All the masked projections were then used as an anchor-set of reference against the initial set of 2D class averages in the angular reconstruction process thus allowing the generation of a new set of re-oriented 2D class averages with refined β Euler angles. The best sub-set of these 2D class averages were subsequently used to generate a new 3D map. This procedure has been applied several time until a final volume (Figure 3.13A) with a resolution of 30.3 Å (FSC=0.5) (Figure 3.13B) was obtained.

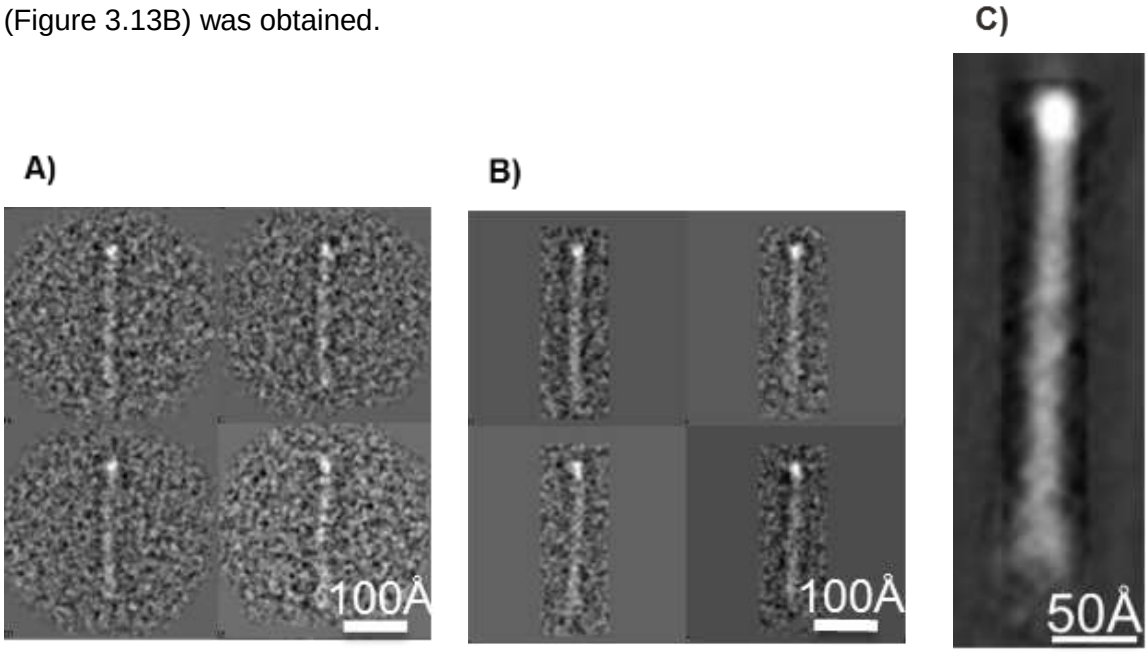

Figure 3.12: 2D processing of NadA var.3.The scale bar is reported in white at the bottom part of each panel. A) Raw particles. B) MSA classification of masked particles. C) Best class average chosen for the 3D reconstruction.

The 3D reconstruction displays a globular compact part at the N-terminus, with a diameter of 35 Å, showing a three-fold density distribution that corresponds to the head, and a long (290 Å) and thin stalk of 15 Å in diameter. The measurements on the density map confirm the calculation performed on the raw particles (Figure 3.13A).

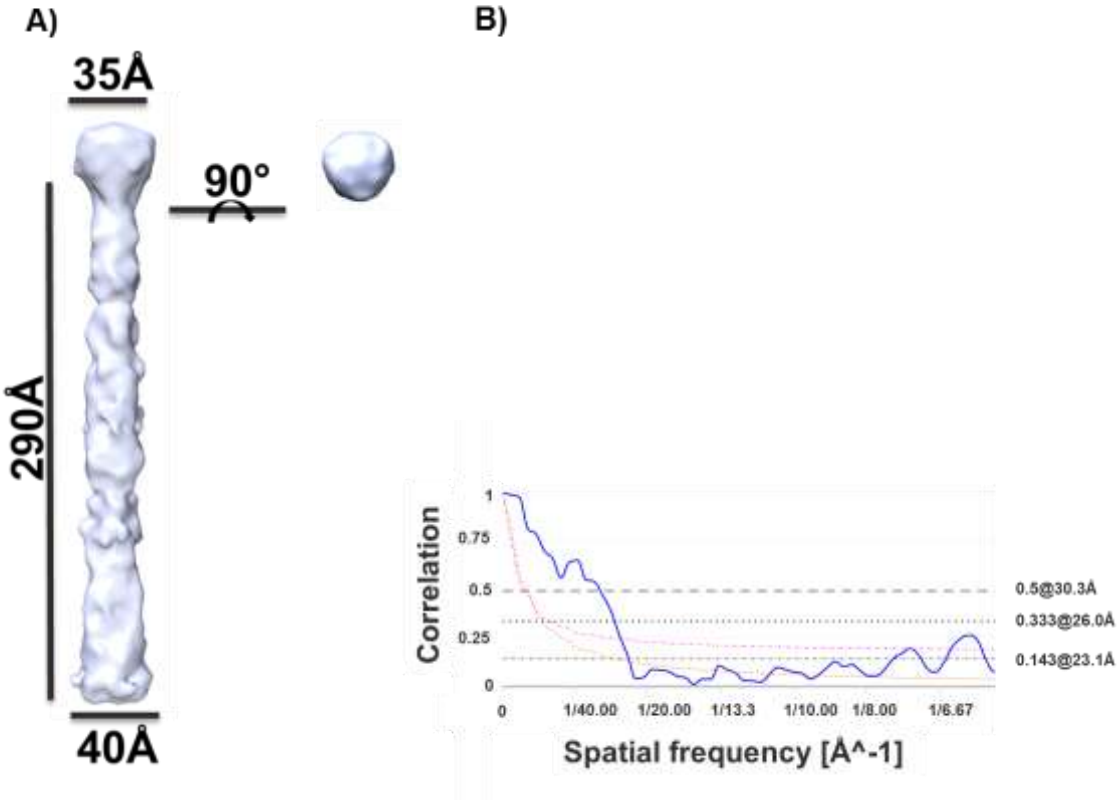

Figure 3.13: 3D reconstruction of the NadA var.3. A) The final map of the antigen with the measurementon the side of the map. B) FSC curve.

The EM structure of the NadA var.3 was manually fitted using Chimera (https://www.cgl.ucsf.edu/chimera/) with the model of the NadA var.3 generated from the NadA var. 5 crystal coordinates to investigate the similarities between the two structures. The result proves that the two structures share overall shape; both composed by a globular head followed by an elongated stalk, and are characterized by a three-fold symmetry. Moreover, the result indicates that NadA var.5 head has a larger diameter (40 Å) compared to the NadA var.3 head (35 Å) and there is no trace in the NadA var.3 EM structure of the three wings decorating the NadA var.5 head. This could be due to the low resolution of NadA var.3 EM map or due to a different way of packing of the three wings against the central coiled-coil α-helices that form the central part of the NadA var.5 head (Figure 3.14B).

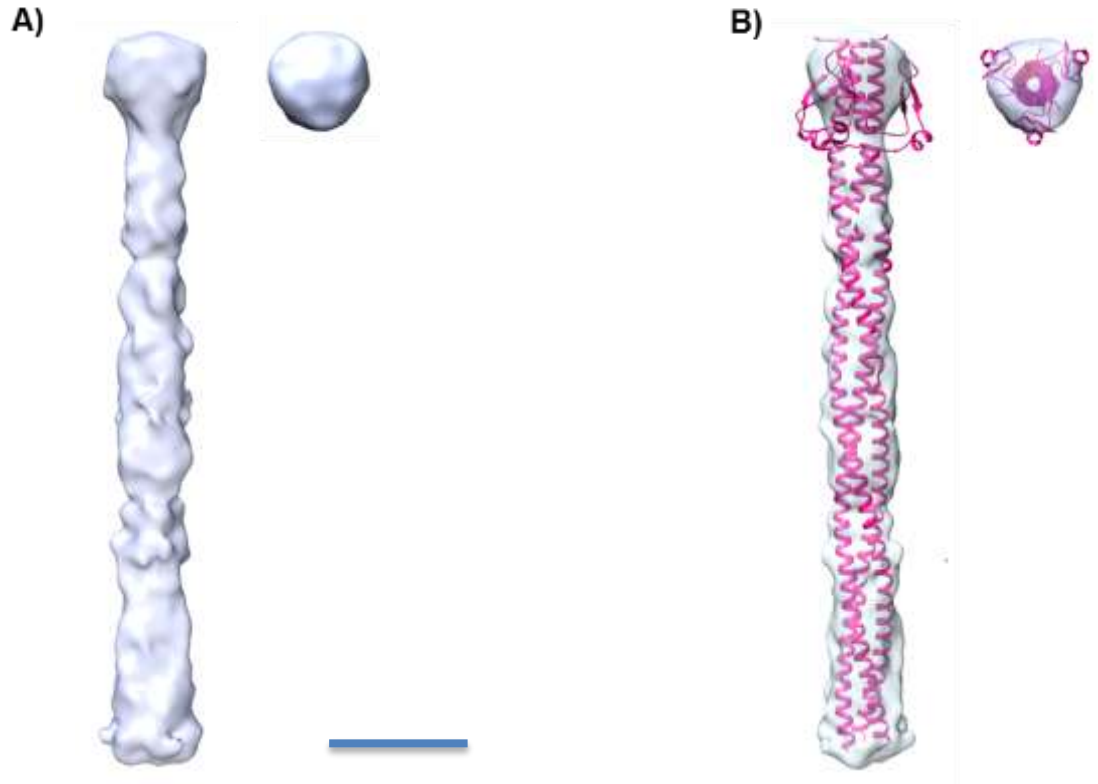

Figure 3.14: Structure of the NadA var.3. Scale bar is reported in blue and corresponds to 50 Å. A) Structure of the EM map of the NadA var.3. B) Manual fitting between the structure of the NadA var. 3 generated by EM data and the model of NadAV var.3 obtained by the crystal structure of the NadA var.5 reported in Malito et al.2014.

3.4.4 Interruptions of periodicity of NadA var.3

A remarkable feature observed in the EM structure of the NadA var.3 is the presence along the stalk, of three points where the diameter is thinner compared to the rest of the stalk. One point is closer to the N-terminus and the second closer to the C-terminus. When the NadA var.3 volume is observed at two different threshold density levels the three points of density interruption become evident (Figure 3.15A, arrows). The presence and the position of these density interruptions well correlate with the presence of the points of lack of coiled-coil periodicity observed in the NadA var.3 sequence (Figure 3.15B, boxed).

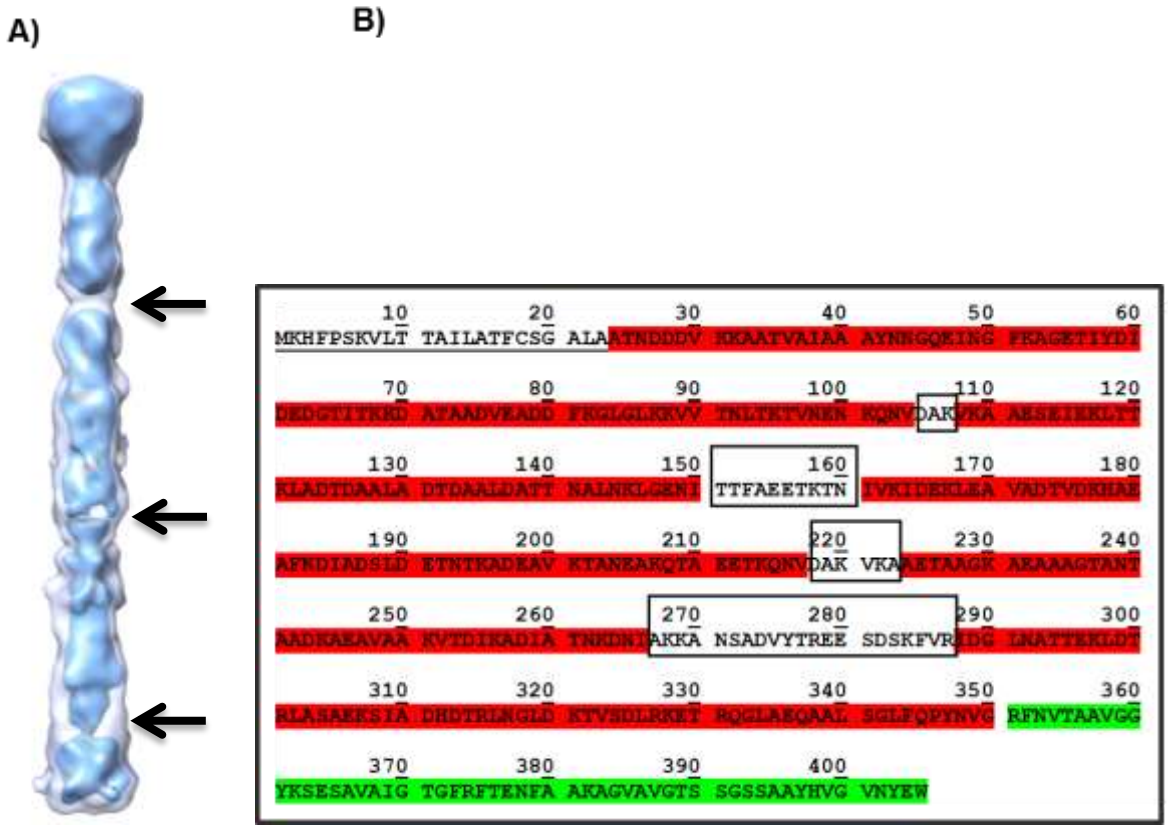

Figure 3.15: Analysis of periodicity interruptions in of the NadA var.3 stalk. A) Fitting between EM structures with different density level displayed. The two maps are reported in light blue and dark blue. Arrows indicate the points of density interruption. B) Sequence of the NadA var.3 gene fragment (UniProt Q8KH85). The leader peptide is underlined in the sequence; the passenger domain is highlight in red; the anchor domain is green colored. The boxes identify the regions with lack of periodicity.

3.5 Discussion

The NadA antigen is an outer membrane protein of *N.meningitidis* involved in bacterial adhesion and entry into epithelial cells (Capecchi et al., 2005). The antigen belongs to the TAA family sharing the common structure of an N-terminal head region, a homotrimeric coiled-coil stalk and a C-terminal membrane anchor (Bassler et al., 2015; Linke et al., 2006). Although there have been numerous attempts with crystallization trials, no crystal structure of the vaccine antigen NadA var.3 was obtained so far. Recently the crystal structure of the NadA var.5 revealed a novel structure among the other TAAs lacking a truly independent globular head domain (Malito et al., 2014).

A sequence analysis between the NadA var.3 and NadA var.5 highlighted the presence in the NadA var.3 stalk of two insertions and three regions with lack of the hepdad repeats periodicity typical of the coiled-coil (Malito et al., 2014).

In the last 20 years single particle electron microscopy has arisen as a very powerful structural biology technique thanks to the great improvement in the sample preparation, the technical tools and software. Here we applied both negative stain and Cryo-EM to structurally investigate NadA var.3 in order to deeply characterize the possible mechanism of function.

A preliminary morphological analysis using negative stain EM was performed revealing also the preferred side view of the antigen deposited onto the grid. Structurally NadA var.3 is composed by a thin and elongated rod-like organization with a globular part located at one end. The main feature of the particles is the flexibility in the stalk region leading to a deviation of 30-90° in the curved particles from the straight ones, as described by Malito *et al* (Malito et al., 2014).

The structure composition is confirmed even by the Cryo-EM data showing a long thin stalk ended with a globular head. A deeper observation was performed on the particles extracted from the micrographs before the image processing. The total length of the protein, in fact, seems to be slightly different among particles probably due to the long flexible stalk. A measurement of the antigen in different conformations demonstrates that the molecules present mutual exclusive bends in two recurrent positions of the stalk: the first one at the 1/3 at the N-terminal resulting in a total length of around 230 Å for the straight part and around 60 Å for the curved end. The second bend is detected at the 1/3 of the C-terminal causing a curve of around 40 Å and a straight portion of 250 Å.

The 3D reconstruction shows a globular compact head with a three-fold symmetry at the N-terminal head with a width of 35 Å and a total length of 290 Å. The stalk results in a larger portion of 40 Å may be due to a partial unwind of the three α-helices.

The observation of the NadA var.3 volume at two different threshold density levels reveals three evident points of interruption in the density of the stalk region which correlate with the breaks in the coiled-coil periodicity of the sequence analysis. This result suggests a possible role of the interruptions in the flexibility mechanism of the antigen. An additional extension and flexibility of the stalk assured by the lack of coiled coil periodicity can aid the head of the NadA var.3 in the adhesion function to the cells (Figure 3.16).

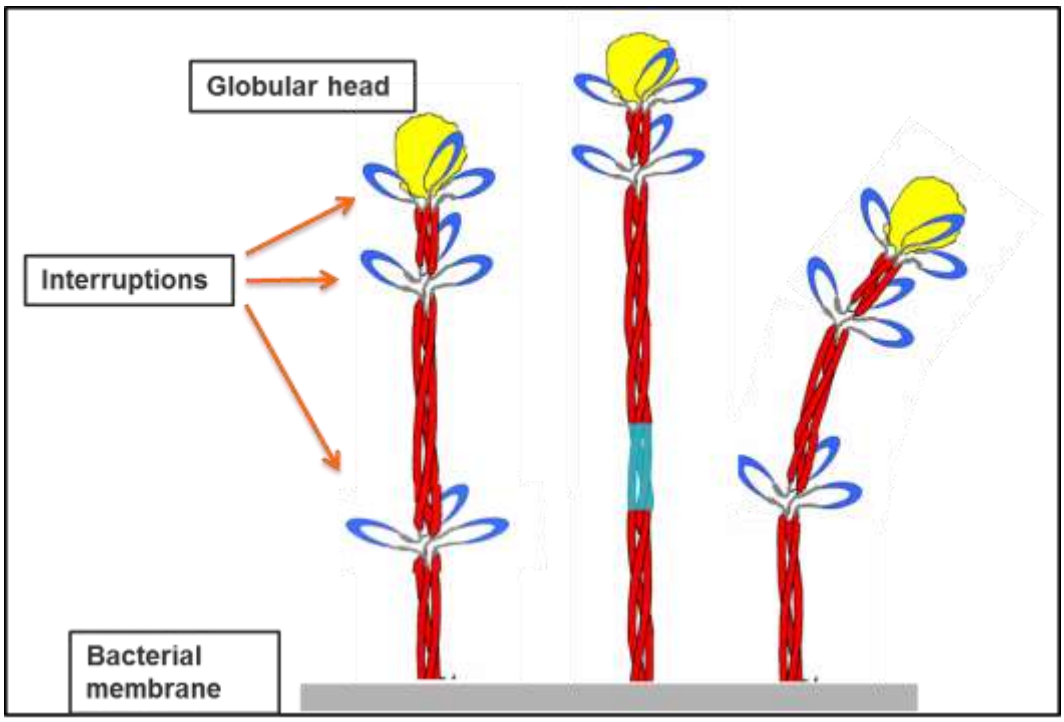

Figure 3.16: Suggested mechanism for the coiled-coil interruptions. The same molecule of NadA var.3 is showed in three different states: normal (left), addition extended (central) and increased bent (right).

References

Abdiche, Y. N., Miles, A., Eckman, J., Foletti, D., Van Blarcom, T. J., Yeung, Y. A., . . . Rajpal, A. (2014). High-throughput epitope binning assays on label-free array-based biosensors can yield exquisite epitope discrimination that facilitates the selection of monoclonal antibodies with functional activity. *PLoS One, 9*(3), e92451. doi: 10.1371/journal.pone.0092451

Allegretti, M., Mills, D. J., McMullan, G., Kuhlbrandt, W., & Vonck, J. (2014). Atomic model of the F420-reducing [NiFe] hydrogenase by electron cryo-microscopy using a direct electron detector. *Elife, 3*, e01963. doi: 10.7554/eLife.01963

Amunts, A., Brown, A., Bai, X. C., Llacer, J. L., Hussain, T., Emsley, P., . . . Ramakrishnan, V. (2014). Structure of the yeast mitochondrial large ribosomal subunit. *Science, 343*(6178), 1485-1489. doi: 10.1126/science.1249410

Aslam, M., & Perkins, S. J. (2001). Folded-back solution structure of monomeric factor H of human complement by synchrotron X-ray and neutron scattering, analytical ultracentrifugation and constrained molecular modelling. *J Mol Biol, 309*(5), 1117-1138. doi: 10.1006/jmbi.2001.4720

Bai, X. C., McMullan, G., & Scheres, S. H. (2015). How cryo-EM is revolutionizing structural biology. *Trends Biochem Sci, 40*(1), 49-57. doi: 10.1016/j.tibs.2014.10.005

Bambini, S., De Chiara, M., Muzzi, A., Mora, M., Lucidarme, J., Brehony, C., . . . Jolley, K. A. (2014). Neisseria adhesin A variation and revised nomenclature scheme. *Clin Vaccine Immunol, 21*(7), 966-971. doi: 10.1128/CVI.00825-13

Bambini, S., Muzzi, A., Olcen, P., Rappuoli, R., Pizza, M., & Comanducci, M. (2009). Distribution and genetic variability of three vaccine components in a panel of strains representative of the diversity of serogroup B meningococcus. *Vaccine, 27*(21), 2794-2803. doi: 10.1016/j.vaccine.2009.02.098

Bartesaghi, A., Merk, A., Banerjee, S., Matthies, D., Wu, X., Milne, J. L., & Subramaniam, S. (2015). 2.2 A resolution cryo-EM structure of beta-galactosidase in complex with a cell-permeant inhibitor. *Science, 348*(6239), 1147-1151. doi: 10.1126/science.aab1576

Bassler, J., Hernandez Alvarez, B., Hartmann, M. D., & Lupas, A. N. (2015). A domain dictionary of trimeric autotransporter adhesins. *Int J Med Microbiol, 305*(2), 265-275. doi: 10.1016/j.ijmm.2014.12.010

Beernink, P. T., Giuntini, S., Costa, I., Lucas, A. H., & Granoff, D. M. (2015). Functional Analysis of the Human Antibody Response to Meningococcal Factor H Binding Protein. *MBio, 6*(3), e00842. doi: 10.1128/mBio.00842-15

Beernink, P. T., LoPasso, C., Angiolillo, A., Felici, F., & Granoff, D. (2009). A region of the N-terminal domain of meningococcal factor H-binding protein that elicits bactericidal antibody across antigenic variant groups. *Mol Immunol, 46*(8-9), 1647-1653. doi: 10.1016/j.molimm.2009.02.021

Beernink, P. T., Shaughnessy, J., Braga, E. M., Liu, Q., Rice, P. A., Ram, S., & Granoff, D. M. (2011). A meningococcal factor H binding protein mutant that eliminates factor H binding enhances protective antibody responses to vaccination. *J Immunol, 186*(6), 3606-3614. doi: 10.4049/jimmunol.1003470

Beernink, P. T., Shaughnessy, J., Stefek, H., Ram, S., & Granoff, D. M. (2014). Heterogeneity in rhesus macaque complement factor H binding to meningococcal factor H binding protein (FHbp) informs selection of primates to assess immunogenicity of FHbp-based vaccines. *Clin Vaccine Immunol, 21*(11), 1505-1511. doi: 10.1128/CVI.00517-14

Beernink, P. T., Welsch, J. A., Bar-Lev, M., Koeberling, O., Comanducci, M., & Granoff, D. M. (2008). Fine antigenic specificity and cooperative bactericidal activity of monoclonal antibodies directed at the meningococcal vaccine candidate factor h-binding protein. *Infect Immun, 76*(9), 4232-4240. doi: 10.1128/IAI.00367-08

Belnap, D. M. (2015). Electron Microscopy and Image Processing: Essential Tools for Structural Analysis of Macromolecules. *Curr Protoc Protein Sci, 82*, 17 12 11-17 12 61. doi: 10.1002/0471140864.ps1702s82

Bindon, C. I., Hale, G., & Waldmann, H. (1988). Importance of antigen specificity for complement-mediated lysis by monoclonal antibodies. *Eur J Immunol, 18*(10), 1507-1514. doi: 10.1002/eji.1830181006

Bolin, I., Norlander, L., & Wolf-Watz, H. (1982). Temperature-inducible outer membrane protein of Yersinia pseudotuberculosis and Yersinia enterocolitica is associated with the virulence plasmid. *Infect Immun, 37*(2), 506-512.

Booth, D. S., Avila-Sakar, A., & Cheng, Y. (2011). Visualizing proteins and macromolecular complexes by negative stain EM: from grid preparation to image acquisition. *J Vis Exp*(58). doi: 10.3791/3227

Borrow, R., Carlone, G. M., Rosenstein, N., Blake, M., Feavers, I., Martin, D., . . . Stephens, D. (2006). Neisseria meningitidis group B correlates of protection and assay standardization--international meeting report Emory University, Atlanta, Georgia, United States, 16-17 March 2005. *Vaccine, 24*(24), 5093-5107.

Borsos, T., & Rapp, H. J. (1965). Complement fixation on cell surfaces by 19S and 7S antibodies. *Science, 150*(3695), 505-506.

Brilot, A. F., Chen, J. Z., Cheng, A., Pan, J., Harrison, S. C., Potter, C. S., . . . Grigorieff, N. (2012). Beam-induced motion of vitrified specimen on holey carbon film. *J Struct Biol, 177*(3), 630-637. doi: 10.1016/j.jsb.2012.02.003

Burton, D. R. (1986). Is IgM-like dislocation a common feature of antibody function? *Immunology Today, 7*(6), 165-167. doi: 10.1016/0167-5699(86)90166-0

Cantini, F., Veggi, D., Dragonetti, S., Savino, S., Scarselli, M., Romagnoli, G., . . . Rappuoli, R. (2009). Solution structure of the factor H-binding protein, a survival factor and protective antigen of Neisseria meningitidis. *J Biol Chem, 284*(14), 9022-9026. doi: 10.1074/jbc.C800214200

Cao, E., Liao, M., Cheng, Y., & Julius, D. (2013). TRPV1 structures in distinct conformations reveal activation mechanisms. *Nature, 504*(7478), 113-118. doi: 10.1038/nature12823

Capecchi, B., Adu-Bobie, J., Di Marcello, F., Ciucchi, L., Masignani, V., Taddei, A., . . . Arico, B. (2005). Neisseria meningitidis NadA is a new invasin which promotes bacterial adhesion to and penetration into human epithelial cells. *Mol Microbiol, 55*(3), 687-698. doi: 10.1111/j.1365-2958.2004.04423.x

Carazo, J. M., Sorzano, C. O., Oton, J., Marabini, R., & Vargas, J. (2015). Three-dimensional reconstruction methods in Single Particle Analysis from transmission electron microscopy data. *Arch Biochem Biophys, 581*, 39-48. doi: 10.1016/j.abb.2015.05.003

Caugant, D. A., & Maiden, M. C. (2009). Meningococcal carriage and disease--population biology and evolution. *Vaccine, 27 Suppl 2*, B64-70. doi: 10.1016/j.vaccine.2009.04.061

Cendron, L., Veggi, D., Girardi, E., & Zanotti, G. (2011). Structure of the uncomplexed Neisseria meningitidis factor H-binding protein fHbp (rLP2086). *Acta Crystallogr Sect F Struct Biol Cryst Commun, 67*(Pt 5), 531-535. doi: 10.1107/S1744309111006154

Cheng, Y., Grigorieff, N., Penczek, P. A., & Walz, T. (2015). A primer to single-particle cryo-electron microscopy. *Cell, 161*(3), 438-449. doi: 10.1016/j.cell.2015.03.050

Chiang, M. H., Sung, W. C., Lien, S. P., Chen, Y. Z., Lo, A. F., Huang, J. H., . . . Chong, P. (2015). Identification of novel vaccine candidates against Acinetobacter baumannii using reverse vaccinology. *Hum Vaccin Immunother, 11*(4), 1065-1073. doi: 10.1080/21645515.2015.1010910

Comanducci, M., Bambini, S., Brunelli, B., Adu-Bobie, J., Arico, B., Capecchi, B., . . . Mora, M. (2002). NadA, a novel vaccine candidate of Neisseria meningitidis. *J Exp Med, 195*(11), 1445-1454.

Comanducci, M., Bambini, S., Caugant, D. A., Mora, M., Brunelli, B., Capecchi, B., . . . Pizza, M. (2004). NadA diversity and carriage in Neisseria meningitidis. *Infect Immun, 72*(7), 4217-4223. doi: 10.1128/IAI.72.7.4217-4223.2004

Cooper, N. R. (1985). The classical complement pathway: activation and regulation of the first complement component. *Adv Immunol, 37*, 151-216.

Costantino, P., Rappuoli, R., & Berti, F. (2011). The design of semi-synthetic and synthetic glycoconjugate vaccines. *Expert Opinion on Drug Discovery, 6*(10), 1045-1066. doi: 10.1517/17460441.2011.609554

Cotter, S. E., Surana, N. K., Grass, S., & St Geme, J. W., 3rd. (2006). Trimeric autotransporters require trimerization of the passenger domain for stability and adhesive activity. *J Bacteriol, 188*(15), 5400-5407. doi: 10.1128/JB.00164-06

Cozzi, R., Scarselli, M., & Ferlenghi, I. (2013). Structural vaccinology: a three-dimensional view for vaccine development. *Curr Top Med Chem, 13*(20), 2629-2637.

Cragg, M. S., & Glennie, M. J. (2004). Antibody specificity controls in vivo effector mechanisms of anti-CD20 reagents. *Blood, 103*(7), 2738-2743. doi: 10.1182/blood-2003-06-2031

Cragg, M. S., Morgan, S. M., Chan, H. T., Morgan, B. P., Filatov, A. V., Johnson, P. W., . . . Glennie, M. J. (2003). Complement-mediated lysis by anti-CD20 mAb correlates with segregation into lipid rafts. *Blood, 101*(3), 1045-1052. doi: 10.1182/blood-2002-06-1761

Czajkowsky, D. M., & Shao, Z. (2009). The human IgM pentamer is a mushroom-shaped molecule with a flexural bias. *Proc Natl Acad Sci U S A, 106*(35), 14960-14965. doi: 10.1073/pnas.0903805106

Danev, R., Buijsse, B., Khoshouei, M., Plitzko, J. M., & Baumeister, W. (2014). Volta potential phase plate for in-focus phase contrast transmission electron microscopy. *Proc Natl Acad Sci U S A, 111*(44), 15635-15640. doi: 10.1073/pnas.1418377111

Davies, A. M., Jefferis, R., & Sutton, B. J. (2014). Crystal structure of deglycosylated human IgG4-Fc. *Mol Immunol, 62*(1), 46-53. doi: 10.1016/j.molimm.2014.05.015

Delany, I., Rappuoli, R., & De Gregorio, E. (2014). Vaccines for the 21st century. *EMBO Mol Med, 6*(6), 708-720. doi: 10.1002/emmm.201403876

Diebolder, C. A., Beurskens, F. J., de Jong, R. N., Koning, R. I., Strumane, K., Lindorfer, M. A., . . . Parren, P. W. (2014). Complement is activated by IgG hexamers assembled at the cell surface. *Science, 343*(6176), 1260-1263. doi: 10.1126/science.1248943

DiScipio, R. G. (1992). Ultrastructures and interactions of complement factors H and I. *J Immunol, 149*(8), 2592-2599.

Esposito, V., Musi, V., de Chiara, C., Veggi, D., Serruto, D., Scarselli, M., . . . Pastore, A. (2011). Structure of the C-terminal domain of Neisseria heparin binding antigen (NHBA), one of the main antigens of a novel vaccine against Neisseria meningitidis. *J Biol Chem, 286*(48), 41767-41775. doi: 10.1074/jbc.M111.289314

Fagnocchi, L., Biolchi, A., Ferlicca, F., Boccadifuoco, G., Brunelli, B., Brier, S., . . . Delany, I. (2013). Transcriptional regulation of the nadA gene in Neisseria

meningitidis impacts the prediction of coverage of a multicomponent meningococcal serogroup B vaccine. *Infect Immun, 81*(2), 560-569. doi: 10.1128/IAI.01085-12
Faleri, A., Santini, L., Brier, S., Pansegrau, W., Lo Surdo, P., Scarselli, M., . . . Masignani, V. (2014). Two cross-reactive monoclonal antibodies recognize overlapping epitopes on Neisseria meningitidis factor H binding protein but have different functional properties. *FASEB J, 28*(4), 1644-1653. doi: 10.1096/fj.13-239012
Feinstein, A., Richardson, N., & Taussig, M. I. (1986). Immunoglobulin flexibility in complement activation. *Immunology Today, 7*(6), 169-174. doi: 10.1016/0167-5699(86)90168-4
Fernandez, I. S., Bai, X. C., Murshudov, G., Scheres, S. H., & Ramakrishnan, V. (2014). Initiation of translation by cricket paralysis virus IRES requires its translocation in the ribosome. *Cell, 157*(4), 823-831. doi: 10.1016/j.cell.2014.04.015
Ferreira, V. P., Pangburn, M. K., & Cortes, C. (2010). Complement control protein factor H: the good, the bad, and the inadequate. *Mol Immunol, 47*(13), 2187-2197. doi: 10.1016/j.molimm.2010.05.007
Finne, J., Leinonen, M., & Makela, P. H. (1983). Antigenic similarities between brain components and bacteria causing meningitis. Implications for vaccine development and pathogenesis. *Lancet, 2*(8346), 355-357.
Fletcher, L. D., Bernfield, L., Barniak, V., Farley, J. E., Howell, A., Knauf, M., . . . Zlotnick, G. W. (2004). Vaccine potential of the Neisseria meningitidis 2086 lipoprotein. *Infect Immun, 72*(4), 2088-2100.
Forneris, F., Wu, J., & Gros, P. (2012). The modular serine proteases of the complement cascade. *Curr Opin Struct Biol, 22*(3), 333-341. doi: 10.1016/j.sbi.2012.04.001
Frank, J. (2006). *Three-dimensional electron microscopy of macromolecular assemblies: visualization of biological molecules in their native state*: Oxford University Press.
Frank, J. (2009). Single-particle reconstruction of biological macromolecules in electron microscopy--30 years. *Q Rev Biophys, 42*(3), 139-158. doi: 10.1017/S0033583509990059
Frank, J., Shimkin, B., & Dowse, H. (1981). Spider—A modular software system for electron image processing. *Ultramicroscopy, 6*(4), 343-357. doi: http://dx.doi.org/10.1016/S0304-3991(81)80236-7
Gaboriaud, C., Juanhuix, J., Gruez, A., Lacroix, M., Darnault, C., Pignol, D., . . . Arlaud, G. J. (2003). The crystal structure of the globular head of complement protein C1q provides a basis for its versatile recognition properties. *J Biol Chem, 278*(47), 46974-46982. doi: 10.1074/jbc.M307764200
Gaboriaud, C., Ling, W. L., Thielens, N. M., Bally, I., & Rossi, V. (2014). Deciphering the fine details of c1 assembly and activation mechanisms: "mission impossible"? *Front Immunol, 5*, 565. doi: 10.3389/fimmu.2014.00565
Gaboriaud, C., Thielens, N. M., Gregory, L. A., Rossi, V., Fontecilla-Camps, J. C., & Arlaud, G. J. (2004). Structure and activation of the C1 complex of complement: unraveling the puzzle. *Trends Immunol, 25*(7), 368-373. doi: 10.1016/j.it.2004.04.008
Galkin, V. E., Orlova, A., & Egelman, E. H. (2012). Actin filaments as tension sensors. *Curr Biol, 22*(3), R96-101. doi: 10.1016/j.cub.2011.12.010
Giuliani, M. M., Adu-Bobie, J., Comanducci, M., Arico, B., Savino, S., Santini, L., . . . Pizza, M. (2006). A universal vaccine for serogroup B meningococcus. *Proc Natl Acad Sci U S A, 103*(29), 10834-10839. doi: 10.1073/pnas.0603940103

Giuliani, M. M., Santini, L., Brunelli, B., Biolchi, A., Arico, B., Di Marcello, F., . . . Pizza, M. (2005). The region comprising amino acids 100 to 255 of Neisseria meningitidis lipoprotein GNA 1870 elicits bactericidal antibodies. *Infect Immun, 73*(2), 1151-1160. doi: 10.1128/IAI.73.2.1151-1160.2005

Giuntini, S., Reason, D. C., & Granoff, D. M. (2011). Complement-mediated bactericidal activity of anti-factor H binding protein monoclonal antibodies against the meningococcus relies upon blocking factor H binding. *Infect Immun, 79*(9), 3751-3759. doi: 10.1128/IAI.05182-11

Giuntini, S., Reason, D. C., & Granoff, D. M. (2012). Combined roles of human IgG subclass, alternative complement pathway activation, and epitope density in the bactericidal activity of antibodies to meningococcal factor h binding protein. *Infect Immun, 80*(1), 187-194. doi: 10.1128/IAI.05956-11

Glaeser, R. M., Typke, D., Tiemeijer, P. C., Pulokas, J., & Cheng, A. (2011). Precise beam-tilt alignment and collimation are required to minimize the phase error associated with coma in high-resolution cryo-EM. *J Struct Biol, 174*(1), 1-10. doi: 10.1016/j.jsb.2010.12.005

Goldschneider, I., Gotschlich, E. C., & Artenstein, M. S. (1969). Human immunity to the meningococcus. I. The role of humoral antibodies. *J Exp Med, 129*(6), 1307-1326.

Granoff, D. M., Welsch, J. A., & Ram, S. (2009). Binding of complement factor H (fH) to Neisseria meningitidis is specific for human fH and inhibits complement activation by rat and rabbit sera. *Infect Immun, 77*(2), 764-769. doi: 10.1128/IAI.01191-08

Greenspan, N. S., & Bona, C. A. (1993). Idiotypes: structure and immunogenicity. *FASEB J, 7*(5), 437-444.

Grigorieff, N. (2007). FREALIGN: high-resolution refinement of single particle structures. *J Struct Biol, 157*(1), 117-125. doi: 10.1016/j.jsb.2006.05.004

Harris, J. R., Schroder, E., Isupov, M. N., Scheffler, D., Kristensen, P., Littlechild, J. A., . . . Meissner, U. (2001). Comparison of the decameric structure of peroxiredoxin-II by transmission electron microscopy and X-ray crystallography. *Biochim Biophys Acta, 1547*(2), 221-234.

Harrison, S. C. (2004). Whither structural biology? *Nat Struct Mol Biol, 11*(1), 12-15. doi: 10.1038/nsmb0104-12

Hartmann, M. D., Ridderbusch, O., Zeth, K., Albrecht, R., Testa, O., Woolfson, D. N., . . . Alvarez, B. H. (2009). A coiled-coil motif that sequesters ions to the hydrophobic core. *Proc Natl Acad Sci U S A, 106*(40), 16950-16955. doi: 10.1073/pnas.0907256106

Henderson, R. (1995). The potential and limitations of neutrons, electrons and X-rays for atomic resolution microscopy of unstained biological molecules. *Q Rev Biophys, 28*(2), 171-193.

Hughes-Jones, N. C., Gorick, B. D., Howard, J. C., & Feinstein, A. (1985). Antibody density on rat red cells determines the rate of activation of the complement component C1. *Eur J Immunol, 15*(10), 976-980. doi: 10.1002/eji.1830151003

Idusogie, E. E., Presta, L. G., Gazzano-Santoro, H., Totpal, K., Wong, P. Y., Ultsch, M., . . . Mulkerrin, M. G. (2000). Mapping of the C1q binding site on rituxan, a chimeric antibody with a human IgG1 Fc. *J Immunol, 164*(8), 4178-4184.

Kaldor, S. W., Kalish, V. J., Davies, J. F., 2nd, Shetty, B. V., Fritz, J. E., Appelt, K., . . . Tatlock, J. H. (1997). Viracept (nelfinavir mesylate, AG1343): a potent, orally bioavailable inhibitor of HIV-1 protease. *J Med Chem, 40*(24), 3979-3985. doi: 10.1021/jm9704098

Kang, Y. S., Do, Y., Lee, H. K., Park, S. H., Cheong, C., Lynch, R. M., . . . Park, C. G. (2006). A dominant complement fixation pathway for pneumococcal

polysaccharides initiated by SIGN-R1 interacting with C1q. *Cell, 125*(1), 47-58. doi: 10.1016/j.cell.2006.01.046
Kellner, C., Derer, S., Valerius, T., & Peipp, M. (2014). Boosting ADCC and CDC activity by Fc engineering and evaluation of antibody effector functions. *Methods, 65*(1), 105-113. doi: 10.1016/j.ymeth.2013.06.036
Khatami, A., & Pollard, A. J. (2010). The epidemiology of meningococcal disease and the impact of vaccines. *Expert Rev Vaccines, 9*(3), 285-298. doi: 10.1586/ERV.10.3
Khoshouei, M., Radjainia, M., Phillips, A. J., Gerrard, J. A., Mitra, A. K., Plitzko, J. M., . . . Danev, R. (2016). Volta phase plate cryo-EM of the small protein complex Prx3. *Nat Commun, 7*, 10534. doi: 10.1038/ncomms10534
Kim, C. U., Lew, W., Williams, M. A., Liu, H., Zhang, L., Swaminathan, S., . . . Stevens, R. C. (1997). Influenza neuraminidase inhibitors possessing a novel hydrophobic interaction in the enzyme active site: design, synthesis, and structural analysis of carbocyclic sialic acid analogues with potent anti-influenza activity. *J Am Chem Soc, 119*(4), 681-690.
Kirkitadze, M. D., & Barlow, P. N. (2001). Structure and flexibility of the multiple domain proteins that regulate complement activation. *Immunol Rev, 180*, 146-161.
Kishore, U., Ghai, R., Greenhough, T. J., Shrive, A. K., Bonifati, D. M., Gadjeva, M. G., . . . Agrawal, A. (2004). Structural and functional anatomy of the globular domain of complement protein C1q. *Immunol Lett, 95*(2), 113-128. doi: 10.1016/j.imlet.2004.06.015
Koiwai, K., Hartmann, M. D., Linke, D., Lupas, A. N., & Hori, K. (2015). Structural Basis for Toughness and Flexibility in the C-terminal Passenger Domain of an Acinetobacter Trimeric Autotransporter Adhesin. *J Biol Chem*. doi: 10.1074/jbc.M115.701698
Konar, M., Granoff, D. M., & Beernink, P. T. (2013). Importance of inhibition of binding of complement factor H for serum bactericidal antibody responses to meningococcal factor H-binding protein vaccines. *J Infect Dis, 208*(4), 627-636. doi: 10.1093/infdis/jit239
Kristensen, C. G., Nakagawa, Y., Coe, F. L., & Lindheimer, M. D. (1986). Effect of atrial natriuretic factor in rat pregnancy. *Am J Physiol, 250*(4 Pt 2), R589-594.
Kuhlbrandt, W. (2014). Biochemistry. The resolution revolution. *Science, 343*(6178), 1443-1444. doi: 10.1126/science.1251652
Lafontaine, E. R., Cope, L. D., Aebi, C., Latimer, J. L., McCracken, G. H., Jr., & Hansen, E. J. (2000). The UspA1 protein and a second type of UspA2 protein mediate adherence of Moraxella catarrhalis to human epithelial cells in vitro. *J Bacteriol, 182*(5), 1364-1373.
Leca, M., Bornet, C., Montana, M., Curti, C., & Vanelle, P. (2015). Meningococcal vaccines: Current state and future outlook. *Pathol Biol (Paris), 63*(3), 144-151. doi: 10.1016/j.patbio.2015.04.003
Leo, J. C., Grin, I., & Linke, D. (2012). Type V secretion: mechanism(s) of autotransport through the bacterial outer membrane. *Philos Trans R Soc Lond B Biol Sci, 367*(1592), 1088-1101. doi: 10.1098/rstb.2011.0208
Lewis, L. A., Ngampasutadol, J., Wallace, R., Reid, J. E., Vogel, U., & Ram, S. (2010). The meningococcal vaccine candidate neisserial surface protein A (NspA) binds to factor H and enhances meningococcal resistance to complement. *PLoS Pathog, 6*(7), e1001027. doi: 10.1371/journal.ppat.1001027
Lewis, L. A., & Ram, S. (2014). Meningococcal disease and the complement system. *Virulence, 5*(1), 98-126. doi: 10.4161/viru.26515
Liao, M., Cao, E., Julius, D., & Cheng, Y. (2013). Structure of the TRPV1 ion channel determined by electron cryo-microscopy. *Nature, 504*(7478), 107-112. doi: 10.1038/nature12822

Liljeroos, L., Malito, E., Ferlenghi, I., & Bottomley, M. J. (2015). Structural and Computational Biology in the Design of Immunogenic Vaccine Antigens. *J Immunol Res, 2015*, 156241. doi: 10.1155/2015/156241

Linke, D., Riess, T., Autenrieth, I. B., Lupas, A., & Kempf, V. A. (2006). Trimeric autotransporter adhesins: variable structure, common function. *Trends Microbiol, 14*(6), 264-270. doi: 10.1016/j.tim.2006.04.005

Liszewski, M. K., Farries, T. C., Lublin, D. M., Rooney, I. A., & Atkinson, J. P. (1996). Control of the complement system. *Adv Immunol, 61*, 201-283.

Lu, P., Bai, X. C., Ma, D., Xie, T., Yan, C., Sun, L., . . . Shi, Y. (2014). Three-dimensional structure of human gamma-secretase. *Nature, 512*(7513), 166-170. doi: 10.1038/nature13567

Lucidarme, J., Tan, L., Exley, R. M., Findlow, J., Borrow, R., & Tang, C. M. (2011). Characterization of Neisseria meningitidis isolates that do not express the virulence factor and vaccine antigen factor H binding protein. *Clin Vaccine Immunol, 18*(6), 1002-1014. doi: 10.1128/CVI.00055-11

Ludtke, S. J., & Serysheva, II. (2013). Single-particle cryo-EM of calcium release channels: structural validation. *Curr Opin Struct Biol, 23*(5), 755-762. doi: 10.1016/j.sbi.2013.06.003

Lyskowski, A., Leo, J. C., & Goldman, A. (2011). Structure and biology of trimeric autotransporter adhesins. *Adv Exp Med Biol, 715*, 143-158. doi: 10.1007/978-94-007-0940-9_9

Madico, G., Welsch, J. A., Lewis, L. A., McNaughton, A., Perlman, D. H., Costello, C. E., . . . Ram, S. (2006). The meningococcal vaccine candidate GNA1870 binds the complement regulatory protein factor H and enhances serum resistance. *J Immunol, 177*(1), 501-510.

Magagnoli, C., Bardotti, A., De Conciliis, G., Galasso, R., Tomei, M., Campa, C., . . . Helling, F. (2009). Structural organization of NadADelta(351-405), a recombinant MenB vaccine component, by its physico-chemical characterization at drug substance level. *Vaccine, 27*(15), 2156-2170. doi: 10.1016/j.vaccine.2009.01.099

Maione, D., Margarit, I., Rinaudo, C. D., Masignani, V., Mora, M., Scarselli, M., . . . Grandi, G. (2005). Identification of a universal Group B streptococcus vaccine by multiple genome screen. *Science, 309*(5731), 148-150. doi: 10.1126/science.1109869

Malito, E., Biancucci, M., Faleri, A., Ferlenghi, I., Scarselli, M., Maruggi, G., . . . Bottomley, M. J. (2014). Structure of the meningococcal vaccine antigen NadA and epitope mapping of a bactericidal antibody. *Proc Natl Acad Sci U S A, 111*(48), 17128-17133. doi: 10.1073/pnas.1419686111

Malito, E., Faleri, A., Lo Surdo, P., Veggi, D., Maruggi, G., Grassi, E., . . . Masignani, V. (2013). Defining a protective epitope on factor H binding protein, a key meningococcal virulence factor and vaccine antigen. *Proc Natl Acad Sci U S A, 110*(9), 3304-3309. doi: 10.1073/pnas.1222845110

Marabini, R., Macias, J. R., Vargas, J., Quintana, A., Sorzano, C. O., & Carazo, J. M. (2013). On the development of three new tools for organizing and sharing information in three-dimensional electron microscopy. *Acta Crystallogr D Biol Crystallogr, 69*(Pt 5), 695-700. doi: 10.1107/S0907444913007038

Marabini, R., Masegosa, I. M., San Martin, M. C., Marco, S., Fernandez, J. J., de la Fraga, L. G., . . . Carazo, J. M. (1996). Xmipp: An Image Processing Package for Electron Microscopy. *J Struct Biol, 116*(1), 237-240.

Mascioni, A., Bentley, B. E., Camarda, R., Dilts, D. A., Fink, P., Gusarova, V., . . . Tsao, D. H. (2009). Structural Basis for the Immunogenic Properties of the Meningococcal Vaccine Candidate LP2086. *J Biol Chem, 284*(13), 8738-8746. doi: 10.1074/jbc.M808831200

Mascioni, A., Moy, F. J., McNeil, L. K., Murphy, E., Bentley, B. E., Camarda, R., . . . Tsao, D. H. (2010). NMR dynamics and antibody recognition of the meningococcal lipidated outer membrane protein LP2086 in micellar solution. *Biochim Biophys Acta, 1798*(2), 87-93. doi: 10.1016/j.bbamem.2009.09.021

Masignani, V., Comanducci, M., Giuliani, M. M., Bambini, S., Adu-Bobie, J., Arico, B., . . . Pizza, M. (2003). Vaccination against Neisseria meningitidis using three variants of the lipoprotein GNA1870. *J Exp Med, 197*(6), 789-799. doi: 10.1084/jem.20021911

McMullan, G., Faruqi, A. R., Henderson, R., Guerrini, N., Turchetta, R., Jacobs, A., & van Hoften, G. (2009). Experimental observation of the improvement in MTF from backthinning a CMOS direct electron detector. *Ultramicroscopy, 109*(9), 1144-1147. doi: 10.1016/j.ultramic.2009.05.005

Meng, G., Surana, N. K., St Geme, J. W., 3rd, & Waksman, G. (2006). Structure of the outer membrane translocator domain of the Haemophilus influenzae Hia trimeric autotransporter. *EMBO J, 25*(11), 2297-2304. doi: 10.1038/sj.emboj.7601132

Montigiani, S., Falugi, F., Scarselli, M., Finco, O., Petracca, R., Galli, G., . . . Grandi, G. (2002). Genomic approach for analysis of surface proteins in Chlamydia pneumoniae. *Infect Immun, 70*(1), 368-379.

Moore, G. L., Chen, H., Karki, S., & Lazar, G. A. (2010). Engineered Fc variant antibodies with enhanced ability to recruit complement and mediate effector functions. *MAbs, 2*(2), 181-189.

Muller-Eberhard, H. J. (1988). Molecular organization and function of the complement system. *Annu Rev Biochem, 57*, 321-347. doi: 10.1146/annurev.bi.57.070188.001541

Naz, A., Awan, F. M., Obaid, A., Muhammad, S. A., Paracha, R. Z., Ahmad, J., & Ali, A. (2015). Identification of putative vaccine candidates against Helicobacter pylori exploiting exoproteome and secretome: a reverse vaccinology based approach. *Infect Genet Evol, 32*, 280-291. doi: 10.1016/j.meegid.2015.03.027

Nogales, E. (2016). The development of cryo-EM into a mainstream structural biology technique. *Nature Methods, 13*(1), 24-27. doi: 10.1038/nmeth.3694

Nogales, E., & Scheres, S. H. (2015). Cryo-EM: A Unique Tool for the Visualization of Macromolecular Complexity. *Mol Cell, 58*(4), 677-689. doi: 10.1016/j.molcel.2015.02.019

Nonaka, M. (2014). Evolution of the complement system. *Subcell Biochem, 80*, 31-43. doi: 10.1007/978-94-017-8881-6_3

Ohi, M., Li, Y., Cheng, Y., & Walz, T. (2004). Negative Staining and Image Classification - Powerful Tools in Modern Electron Microscopy. *Biol Proced Online, 6*, 23-34. doi: 10.1251/bpo70

Oriente, F., Scarlato, V., & Delany, I. (2010). Expression of factor H binding protein of meningococcus responds to oxygen limitation through a dedicated FNR-regulated promoter. *J Bacteriol, 192*(3), 691-701. doi: 10.1128/JB.01308-09

Parce, J. W., Kelley, D., & Heinzelmann, K. (1983). Measurement of antibody-dependent binding, proteolysis, and turnover of C1s on liposomal antigens localizes the fluidity-dependent step in C1 activation. *Biochim Biophys Acta, 736*(1), 92-98.

Pawluczkowycz, A. W., Beurskens, F. J., Beum, P. V., Lindorfer, M. A., van de Winkel, J. G., Parren, P. W., & Taylor, R. P. (2009). Binding of submaximal C1q promotes complement-dependent cytotoxicity (CDC) of B cells opsonized with anti-CD20 mAbs ofatumumab (OFA) or rituximab (RTX): considerably higher levels of CDC are induced by OFA than by RTX. *J Immunol, 183*(1), 749-758. doi: 10.4049/jimmunol.0900632

Pellequer, J. L., & Van Regenmortel, M. H. (1993). Affinity of monoclonal antibodies to large multivalent antigens: influence of steric hindrance on antibody affinity constants calculated from Scatchard plots. *Mol Immunol, 30*(10), 955-958.
Perkins, S. J., Nealis, A. S., & Sim, R. B. (1991). Oligomeric domain structure of human complement factor H by X-ray and neutron solution scattering. *Biochemistry, 30*(11), 2847-2857.
Pizza, M., & Rappuoli, R. (2015). Neisseria meningitidis: pathogenesis and immunity. *Curr Opin Microbiol, 23*, 68-72. doi: 10.1016/j.mib.2014.11.006
Pizza, M., Scarlato, V., Masignani, V., Giuliani, M. M., Arico, B., Comanducci, M., . . . Rappuoli, R. (2000). Identification of vaccine candidates against serogroup B meningococcus by whole-genome sequencing. *Science, 287*(5459), 1816-1820.
Raghunathan, D., Wells, T. J., Morris, F. C., Shaw, R. K., Bobat, S., Peters, S. E., . . . Henderson, I. R. (2011). SadA, a trimeric autotransporter from Salmonella enterica serovar Typhimurium, can promote biofilm formation and provides limited protection against infection. *Infect Immun, 79*(11), 4342-4352. doi: 10.1128/IAI.05592-11
Rappuoli, R. (2001). Reverse vaccinology, a genome-based approach to vaccine development. *Vaccine, 19*(17-19), 2688-2691.
Riess, T., Andersson, S. G., Lupas, A., Schaller, M., Schafer, A., Kyme, P., . . . Kempf, V. A. (2004). Bartonella adhesin a mediates a proangiogenic host cell response. *J Exp Med, 200*(10), 1267-1278. doi: 10.1084/jem.20040500
Ripoche, J., Day, A. J., Harris, T. J., & Sim, R. B. (1988). The complete amino acid sequence of human complement factor H. *Biochem J, 249*(2), 593-602.
Rosenstein, N. E., Perkins, B. A., Stephens, D. S., Popovic, T., & Hughes, J. M. (2001). Meningococcal disease. *N Engl J Med, 344*(18), 1378-1388. doi: 10.1056/NEJM200105033441807
Rosse, W. F., Rapp, H. J., & Borsos, T. (1967). Structural characteristics of hemolytic antibodies as determined by the effects of ionizing radiation. *J Immunol, 98*(6), 1190-1195.
Rouphael, N. G., & Stephens, D. S. (2012). Neisseria meningitidis: biology, microbiology, and epidemiology. *Methods Mol Biol, 799*, 1-20. doi: 10.1007/978-1-61779-346-2_1
Roux, K. H. (1999). Immunoglobulin structure and function as revealed by electron microscopy. *Int Arch Allergy Immunol, 120*(2), 85-99. doi: 24226
Roux, K. H., & Greenspan, N. S. (1994). Monitoring the formation of soluble immune complexes composed of idiotype and anti-idiotype antibodies by electron microscopy. *Mol Immunol, 31*(8), 599-606.
Roux, K. H., & Tankersley, D. L. (1990). A view of the human idiotypic repertoire. Electron microscopic and immunologic analyses of spontaneous idiotype-anti-idiotype dimers in pooled human IgG. *J Immunol, 144*(4), 1387-1395.
Ruskin, R. S., Yu, Z., & Grigorieff, N. (2013). Quantitative characterization of electron detectors for transmission electron microscopy. *J Struct Biol, 184*(3), 385-393. doi: 10.1016/j.jsb.2013.10.016
Sandt, C. H., & Hill, C. W. (2000). Four different genes responsible for nonimmune immunoglobulin-binding activities within a single strain of Escherichia coli. *Infect Immun, 68*(4), 2205-2214. doi: Doi 10.1128/Iai.68.4.2205-2214.2000
Scarselli, M., Arico, B., Brunelli, B., Savino, S., Di Marcello, F., Palumbo, E., . . . Rappuoli, R. (2011). Rational design of a meningococcal antigen inducing broad protective immunity. *Sci Transl Med, 3*(91), 91ra62. doi: 10.1126/scitranslmed.3002234
Scarselli, M., Cantini, F., Santini, L., Veggi, D., Dragonetti, S., Donati, C., . . . Rappuoli, R. (2009). Epitope mapping of a bactericidal monoclonal antibody against the

factor H binding protein of Neisseria meningitidis. *J Mol Biol, 386*(1), 97-108. doi: 10.1016/j.jmb.2008.12.005
Schneider, M. C., Prosser, B. E., Caesar, J. J., Kugelberg, E., Li, S., Zhang, Q., . . . Lea, S. M. (2009). Neisseria meningitidis recruits factor H using protein mimicry of host carbohydrates. *Nature, 458*(7240), 890-893. doi: 10.1038/nature07769
Scott, D. E., Coyne, A. G., Hudson, S. A., & Abell, C. (2012). Fragment-based approaches in drug discovery and chemical biology. *Biochemistry, 51*(25), 4990-5003. doi: 10.1021/bi3005126
Seib, K. L., Scarselli, M., Comanducci, M., Toneatto, D., & Masignani, V. (2015). Neisseria meningitidis factor H-binding protein fHbp: a key virulence factor and vaccine antigen. *Expert Rev Vaccines, 14*(6), 841-859. doi: 10.1586/14760584.2015.1016915
Serruto, D., Bottomley, M. J., Ram, S., Giuliani, M. M., & Rappuoli, R. (2012). The new multicomponent vaccine against meningococcal serogroup B, 4CMenB: immunological, functional and structural characterization of the antigens. *Vaccine, 30 Suppl 2*, B87-97. doi: 10.1016/j.vaccine.2012.01.033
Serruto, D., Spadafina, T., Ciucchi, L., Lewis, L. A., Ram, S., Tontini, M., . . . Arico, B. (2010). Neisseria meningitidis GNA2132, a heparin-binding protein that induces protective immunity in humans. *Proc Natl Acad Sci U S A, 107*(8), 3770-3775. doi: 10.1073/pnas.0915162107
Shigematsu, H., & Sigworth, F. J. (2013). Noise models and cryo-EM drift correction with a direct-electron camera. *Ultramicroscopy, 131*, 61-69. doi: 10.1016/j.ultramic.2013.04.001
Shoenfeld, Y., Kennedy, R. C., & Ferrone, S. (1997). *Idiotypes in medicine : autoimmunity, infection, and cancer*. Amsterdam ; New York: Elsevier.
Sim, R. B., & Perkins, S. J. (1990). Molecular modelling of C3 and its ligands. *Curr Top Microbiol Immunol, 153*, 209-222.
Sorzano, C. O., Bilbao-Castro, J. R., Shkolnisky, Y., Alcorlo, M., Melero, R., Caffarena-Fernandez, G., . . . Carazo, J. M. (2010). A clustering approach to multireference alignment of single-particle projections in electron microscopy. *J Struct Biol, 171*(2), 197-206. doi: 10.1016/j.jsb.2010.03.011
St Geme, J. W., 3rd, & Cutter, D. (2000). The Haemophilus influenzae Hia adhesin is an autotransporter protein that remains uncleaved at the C terminus and fully cell associated. *J Bacteriol, 182*(21), 6005-6013.
Stephens, D. S., Greenwood, B., & Brandtzaeg, P. (2007). Epidemic meningitis, meningococcaemia, and Neisseria meningitidis. *Lancet, 369*(9580), 2196-2210. doi: 10.1016/S0140-6736(07)61016-2
Steven, A. C., & Navia, M. A. (1980). Fidelity of structure representation in electron micrographs of negatively stained protein molecules. *Proc Natl Acad Sci U S A, 77*(8), 4721-4725.
Stoops, J. K., Baker, T. S., Schroeter, J. P., Kolodziej, S. J., Niu, X. D., & Reed, L. J. (1992). Three-dimensional structure of the truncated core of the Saccharomyces cerevisiae pyruvate dehydrogenase complex determined from negative stain and cryoelectron microscopy images. *J Biol Chem, 267*(34), 24769-24775.
Surana, N. K., Cutter, D., Barenkamp, S. J., & St Geme, J. W., 3rd. (2004). The Haemophilus influenzae Hia autotransporter contains an unusually short trimeric translocator domain. *J Biol Chem, 279*(15), 14679-14685. doi: 10.1074/jbc.M311496200
Szalai, A. J., Agrawal, A., Greenhough, T. J., & Volanakis, J. E. (1999). C-reactive protein: structural biology and host defense function. *Clin Chem Lab Med, 37*(3), 265-270. doi: 10.1515/CCLM.1999.046

Talukdar, S., Zutshi, S., Prashanth, K. S., Saikia, K. K., & Kumar, P. (2014). Identification of potential vaccine candidates against Streptococcus pneumoniae by reverse vaccinology approach. *Appl Biochem Biotechnol, 172*(6), 3026-3041. doi: 10.1007/s12010-014-0749-x

Tang, G., Peng, L., Baldwin, P. R., Mann, D. S., Jiang, W., Rees, I., & Ludtke, S. J. (2007). EMAN2: an extensible image processing suite for electron microscopy. *J Struct Biol, 157*(1), 38-46. doi: 10.1016/j.jsb.2006.05.009

Taylor, K. A., & Glaeser, R. M. (1974). Electron diffraction of frozen, hydrated protein crystals. *Science, 186*(4168), 1036-1037.

Teeling, J. L., Mackus, W. J., Wiegman, L. J., van den Brakel, J. H., Beers, S. A., French, R. R., . . . van de Winkel, J. G. (2006). The biological activity of human CD20 monoclonal antibodies is linked to unique epitopes on CD20. *J Immunol, 177*(1), 362-371.

Tettelin, H., Saunders, N. J., Heidelberg, J., Jeffries, A. C., Nelson, K. E., Eisen, J. A., . . . Venter, J. C. (2000). Complete genome sequence of Neisseria meningitidis serogroup B strain MC58. *Science, 287*(5459), 1809-1815.

Thielens, N. M., Tacnet-Delorme, P., & Arlaud, G. J. (2002). Interaction of C1q and mannan-binding lectin with viruses. *Immunobiology, 205*(4-5), 563-574. doi: 10.1078/0171-2985-00155

Valpuesta, J. M., & Carrascosa, J. L. (2015). Electron microscopy: the coming of age of a structural biology technique. *Arch Biochem Biophys, 581*, 1-2. doi: 10.1016/j.abb.2015.06.018

van Heel, M. (1984). Multivariate statistical classification of noisy images (randomly oriented biological macromolecules). *Ultramicroscopy, 13*(1-2), 165-183.

van Heel, M., & Keegstra, W. (1981). IMAGIC: A fast, flexible and friendly image analysis software system. *Ultramicroscopy, 7*(2), 113-129. doi: http://dx.doi.org/10.1016/0304-3991(81)90001-2

Vargas, J., Abrishami, V., Marabini, R., de la Rosa-Trevin, J. M., Zaldivar, A., Carazo, J. M., & Sorzano, C. O. (2013). Particle quality assessment and sorting for automatic and semiautomatic particle-picking techniques. *J Struct Biol, 183*(3), 342-353. doi: 10.1016/j.jsb.2013.07.015

Veesler, D., Campbell, M. G., Cheng, A., Fu, C. Y., Murez, Z., Johnson, J. E., . . . Carragher, B. (2013). Maximizing the potential of electron cryomicroscopy data collected using direct detectors. *J Struct Biol, 184*(2), 193-202. doi: 10.1016/j.jsb.2013.09.003

Voorhees, R. M., Fernandez, I. S., Scheres, S. H., & Hegde, R. S. (2014). Structure of the mammalian ribosome-Sec61 complex to 3.4 A resolution. *Cell, 157*(7), 1632-1643. doi: 10.1016/j.cell.2014.05.024

Vu, D. M., Pajon, R., Reason, D. C., & Granoff, D. M. (2012). A broadly cross-reactive monoclonal antibody against an epitope on the n-terminus of meningococcal fHbp. *Sci Rep, 2*, 341. doi: 10.1038/srep00341

Walport, M. J. (2001a). Complement. First of two parts. *N Engl J Med, 344*(14), 1058-1066. doi: 10.1056/NEJM200104053441406

Walport, M. J. (2001b). Complement. Second of two parts. *N Engl J Med, 344*(15), 1140-1144. doi: 10.1056/NEJM200104123441506

Wang, L., & Sigworth, F. J. (2006). Cryo-EM and single particles. *Physiology (Bethesda), 21*, 13-18. doi: 10.1152/physiol.00045.2005

Wizemann, T. M., Heinrichs, J. H., Adamou, J. E., Erwin, A. L., Kunsch, C., Choi, G. H., . . . Koenig, S. (2001). Use of a whole genome approach to identify vaccine molecules affording protection against Streptococcus pneumoniae infection. *Infect Immun, 69*(3), 1593-1598. doi: 10.1128/IAI.69.3.1593-1598.2001

Wong, W., Bai, X. C., Brown, A., Fernandez, I. S., Hanssen, E., Condron, M., . . . Scheres, S. H. (2014). Cryo-EM structure of the Plasmodium falciparum 80S

ribosome bound to the anti-protozoan drug emetine. *Elife, 3*. doi: 10.7554/eLife.03080
Xia, M. Q., Hale, G., & Waldmann, H. (1993). Efficient complement-mediated lysis of cells containing the CAMPATH-1 (CDw52) antigen. *Mol Immunol, 30*(12), 1089-1096.
Xiang, Z., & He, Y. (2013). Genome-wide prediction of vaccine targets for human herpes simplex viruses using Vaxign reverse vaccinology. *BMC Bioinformatics, 14 Suppl 4*, S2. doi: 10.1186/1471-2105-14-S4-S2
Zhang, X., Zhang, L., Tong, H., Peng, B., Rames, M. J., Zhang, S., & Ren, G. (2015). 3D Structural Fluctuation of IgG1 Antibody Revealed by Individual Particle Electron Tomography. *Sci Rep, 5*, 9803. doi: 10.1038/srep09803
Zhang, X., & Zhou, Z. H. (2011). Limiting factors in atomic resolution cryo electron microscopy: no simple tricks. *J Struct Biol, 175*(3), 253-263. doi: 10.1016/j.jsb.2011.05.004
Zipfel, P. F. (2009). Complement and immune defense: from innate immunity to human diseases. *Immunol Lett, 126*(1-2), 1-7. doi: 10.1016/j.imlet.2009.07.005

List of abbreviations

aa: amino acid

AP: Alternative Pathway

CCP: Complement Control Protein

CP: Classical Pathway

CPS: Capsular PolySaccharide

Cryo-ET: Cryo-Electron Tomography

CTF: Contrast Transfer Function

DD: Direct Detector

DQE: Detective Quantum Efficiency

EM: Electron Microscopy

ELU: Elution

fab: fragment antigen binding

fH: factor H

fHbp: factor H binding protein

FSC: Fourier Shell Correlation

FT: Flow Through

HC: Heavy Chain

HPLC: High Pressure Liquid Chromatography

IG-TEM: ImmunoGold Transmission Electron Microscopy

IMD: Invasive Meningococcal Disease

LC: Liquid Chromatography

mAb: monoclonal Antibody

MAC: Membrane Attack Complex

MenB: Meningococcal serogroup B

NHBA: Neisserial Heparin Binding Protein

MSA: Multivariate Statistical Analysis

NadA: Neisserial Adhesin A

NMR: Nuclear Magnetic Resonance

NR: Non-reducing

NS: Negative Staining

OCA: Oligomeric Coiled-coil Adhesin

RCT: Random Conical Tilt

RT: Room Temperature (18-26°C)

RV: Reverse Vaccinology

SBA: Serum Bactericidal Activity

SNR: Signal-to-Noise Ratio

SP: Single Particle

SPR: Surface Plasmon Resonance

SV: Structural Vaccinology

TAA: Trimeric Autotransporter Adhesin

TEM: Transmission Electron Microscopy

UPLC: Ultra Performance Liquid Chromatography

VPP: Volta Phase Plate